New Variational Models for Graphene-based Nanomaterials

Jabr Ateeg Allah J Aljedani

September, 2022

Thesis submitted for the degree of

Doctor of Philosophy

in

Applied Mathematics

at The University of Adelaide

Faculty of Sciences, Engineering and Technology

School of Mathematical Sciences

THE UNIVERSITY
of ADELAIDE

Contents

Abstract **xv**

Thesis Declaration **xvii**

Acknowledgements **xix**

Dedication **xxi**

1 Introduction **1**

1.1 Background 1

1.2 Graphene properties and applications 2

1.3 Graphene synthesis methods 5

1.4 Graphene configurations 7

1.5 Modelling graphene configurations 9

1.5.1 Small-deformation approach 10

1.5.2 Finite-deformation approach 12

1.5.3 Variational approach 14

1.5.4 Quasi-analytical approach 16

1.5.5 Other approaches 18

1.6 Thesis structure 20

1.7 Nomenclature 23

2 Mathematical methodology **25**

2.1 Theoretical approach 25

2.1.1 Line curvature representations 25

2.1.2 Variational calculus 28

2.1.3 Elliptic integrals 44

2.1.4 Cardano's method 47

2.2 Modelling approach 49

2.2.1 Lennard-Jones potential 49

2.2.2 Dominant energies 53

2.3 Nomenclature 56

3 Single–layer graphene ripples **59**

3.1 Introduction 59

3.2 Model formulation 61

3.3 The transitional case 65

3.3.1 Analytical solutions 65

3.3.2 Numerical results 70

3.4 The substrate constrained case 72

3.4.1 Analytical solutions 72

3.4.2 Numerical results 74

3.5 The graphene constrained case 76

3.5.1 Analytical solutions 76

3.5.2 Numerical results 78

3.6 Results 79

3.7 Conclusion 85

3.8 Nomenclature 87

4 Multi-layer graphene folds on a substrate 89

4.1 Introduction . . . 89

4.2 Model formulation . . . 91

4.3 Variational calculus . . . 96

4.3.1 The one-term approximation . . . 98

4.3.2 The two-term approximation . . . 99

4.3.3 The three-term approximation . . . 100

4.4 Parametric solution . . . 102

4.4.1 The one-term approximation . . . 102

4.4.2 The two-term and three-term approximations . . . 104

4.5 Substrate parameters . . . 105

4.6 Results . . . 108

4.7 Conclusion . . . 111

4.8 Nomenclature . . . 114

5 The effective bending rigidity of multi-layer graphene 115

5.1 Introduction . . . 115

5.2 Model formulation . . . 117

5.3 Multi-layer solution . . . 121

5.4 Single-layer solution . . . 124

5.5 Results . . . 125

5.6 Conclusion . . . 130

5.7 Nomenclature . . . 132

6 Collapsed graphene wrinkles 135

6.1 Introduction . . . 135

6.2 Model formulation . . . 137

6.3 Variational calculus . . . 140

6.3.1 Extremal for E_2 . . . 140
6.3.2 Extremal for E_3 . . . 142
6.3.3 Extremal for E_4 . . . 147
6.4 Substrate parameters . . . 150
6.5 Results . . . 152
6.6 Conclusion . . . 158
6.7 Nomenclature . . . 162

7 Conclusion **165**
7.1 Single-layer graphene ripples . . . 166
7.2 Multi-layer graphene folds . . . 168
7.3 Collapsed graphene wrinkles . . . 169
7.4 Future research . . . 170

A Analytical derivation of (4.3) **175**

Bibliography **177**

List of the author's publications and presentations **189**

List of Tables

1.1 The bending rigidity γ of single-layer graphene sheet. 5

2.1 Elliptic integrals representations used in different symbolic computational programs. 47

3.1 Empirical values for $\delta_{\rm gs}$ and $\epsilon_{\rm gs}$, with the prescribed ripple height $h_{\rm rip}$ for each case of a rippled graphene sheet on a substrate. 65

3.2 The x–component of the critical point and the ripple half arc length $L_{\rm rip}$ for various bending rigidities γ, in the transitional case. 72

3.3 The x–component of the critical point and the ripple half arc length $L_{\rm rip}$ for various bending rigidities γ, in the substrate constrained case. 75

3.4 The x–component of the critical point and the ripple half arc length $L_{\rm rip}$ for various bending rigidities γ, in the graphene constrained case. 79

4.1 Numerical values for $\delta_{\rm gg}$, $\delta_{\rm gs}$, and ϵ obtained using LJ potential. 108

5.1 Numerical values for $\delta_{\rm gg}$, and ϵ obtained using the LJ potential. 121

5.2 Numerical values for A_{min} and γ_{eff} for different numbers of layers N. 127
5.3 The relationship between the bending rigidity of multi-layer graphene and the number of layers N. 130

6.1 Numerical values for the parameters of graphene–graphene interactions and graphene–substrate interactions (based on our calculations unless referenced). 153
6.2 Numerical values for the heights of collapsed wrinkles (Å), and the critical height of self-adhered wrinkles h_{crit} (Å) with the corresponding L_{crit} (Å) and E_{crit} (eV/Å) where the bending rigidity $\gamma = 1.2 \pm 0.4$ eV. 160
6.3 Summary for some values for the critical height h_{crit} and the critical length L_{crit} of self-adhered wrinkles that have been reported in the literature. 160

List of Figures

1.1 The structure of a graphene sheet. 3

1.2 Graphene-based nanomaterials [1]. 4

1.3 Schematic showing the top–down and bottom–up approaches of graphene synthesis. 6

1.4 Observed configurations in CVD-produced graphene: (a) ripples, (b) arch-shaped wrinkles, (c) self-adhered wrinkles, and (d) collapsed wrinkles. 8

1.5 Schematic showing the geometry of folded single-layer graphene. 10

1.6 Comparisons in the predicted folding profiles between: (a) small- and finite-deformation models against MD simulations, and (b) different folding directions. Republished with the permission of IOP Publishing Ltd, from Ref. [2]; permission conveyed through Copyright Clearance Center Inc. 14

1.7 Folding conformations obtained from the variational approach (coloured solid lines, each for a different value of γ) are compared to experimental results (red dotted lines). Reproduced from Ref. [3] with permission from the Royal Society of Chemistry. 16

1.8 The geometry of a self-adhered wrinkle. Reprinted from Ref. [4], with the permission of AIP Publishing. 17

1.9 Folding conformations of perfect and imperfect graphene. Reprinted from Ref. [5], with permission from Elsevier. 19

2.1 Representation of a curve parametrised by s. 28

2.2 Representation of a variational problem with fixed boundary conditions. 30

2.3 Representation of a variational problem with natural boundary conditions on y. 36

2.4 Representation of a variational problem with natural boundary conditions on both x and y. 38

2.5 The LJ potential illustrating the energy well-depth ξ, and the vdW diameter σ. 51

2.6 The interaction of: (a) two planes at a distance φ, and (b) plane with volume of a height $h_{\mathcal{V}}$ at a distance $\tilde{\varphi}$. 52

3.1 Schematic showing the geometry of a rippled graphene sheet. . 62

3.2 Schematic showing the geometries of: (a) the transitional case, (b) the substrate constrained case, and (c) the graphene constrained case. 64

3.3 Rippled graphene sheet located on: (a) Cu(111) substrate and (b) Ni(111) substrate for various values of γ, in the transitional case. The substrate surface is set to be at the horizontal axis. 71

3.4 Rippled graphene sheet located on: (a) Cu(111) substrate and (b) Ni(111) substrate for various values of γ, in the substrate constrained case. The substrate surface is set to be at the horizontal axis. 75

3.5 Rippled graphene sheet located on: (a) Cu(111) substrate and (b) Ni(111) substrate for various values of γ, in the graphene constrained case. The substrate surface is set to be at the horizontal axis. 78

3.6 Various conformations for the right-half of a graphene ripple using the substrate constrained case ($\mu = 0$), the transitional case ($\mu = 0.25, 0.50, 0.75$), and the graphene constrained case ($\mu = 1$). 81

3.7 The relationship between varying the substrate length of: (a) Cu(111) substrate, (b) Ni(111) substrate and the total energy per unit length. 81

3.8 The relationship between reducing the substrate length of: (a) Cu(111) substrate, (b) Ni(111) substrate and the ripple amplitude. 82

3.9 The relationship between reducing the substrate length of: (a) Cu(111) substrate, (b) Ni(111) substrate and the total energy per unit length. 83

3.10 MD simulation models and results of graphene wrinkles reprinted (or adapted) from Ref. [6] licensed under a Creative Commons Attribution 4.0 International License. (a)-(b) The MD simulation model, performed by Wang et al. [6], is presented here in order to adopt the appropriate case among those developed in this model for comparison purposes. (c) The profiles of graphene ripples or wrinkles obtained by the present model (cyan lines) superimposed upon the results of MD simulation. 85

4.1 Schematic showing the geometry of folded 3–layer graphene sheets supported on a substrate. 92

4.2 The LJ potential showing the interaction energy between N graphene layers $\epsilon_{Ng}(\varphi)$. 107

4.3 The predicted folding profiles of 2–layer graphene sheets located on a SiO_2 substrate using: (a) the one-term approximation, (b) the two-term approximation, and (c) the three-term approximation. 110

4.4 Hump heights obtained from the present model using $\gamma = 1.0\,\text{eV}$ superimposed upon the experimental results, reprinted from [7] with the permission of AIP Publishing, for comparison purposes. 111

4.5 The predicted folding profiles of: (a) 3–layer (the two-term approximation), (b) 4–layer (the two-term approximation), (c) 5–layer (the two-term approximation), and (d) 6–layer (the three-term approximation), graphene sheets located on a SiO_2 substrate. 112

5.1 Schematic showing the geometry of folded unsupported 3–layer graphene stack. 118

5.2 Representation of the steps taken to determine γ_{eff} of 2–layer graphene. (a) A series of curves (cyan), generated by the single-layer solution with a range of values for γ, are compared to the mid-line of the predicted folding profile of 2–layer graphene obtained from the multi-layer solution (black). (b) The area between the mid-line and these curves is plotted as a function of γ. (c) The predicted folding profile of 2–layer graphene with a comparison between the mid-line and the curve given by the single-layer solution with $\gamma = \gamma_{\text{eff}}$, where the area A_{min} is shaded in yellow. 128

5.3 The predicted folding profile of: (a) 3–layer (b) 4–layer (c) 5–layer (d) 6–layer, (e) 7–layer, graphene obtained from the multi-layer solution (black) with a comparison between the mid-line and the curve (cyan) given by the single-layer solution with $\gamma = \gamma_{\text{eff}}$, where the area between these curves is shaded in yellow. 129

5.4 (a) The relationship between $\log(\gamma_{\text{eff}})$ and $\log(N)$. The blue dots correspond to the values presented in Table 5.2 which confirm the approximate relationship given in (5.6), represented by the red line. (b) The values of the effective bending rigidity obtained by the present model (blue dots) are compared to earlier results (represented by red), retrieved from Ref. [7]. . 130

6.1 Schematic showing the geometry of: (a) self-adhered graphene wrinkle, (b) collapsed graphene wrinkle, supported on a substrate. 138

6.2 Schematic illustrating the structures of two potential conformations of collapsed wrinkles: (a) Conformation A and (b) Conformation B, with a zero and a non-zero distance following the folded bilayer, respectively. 154

6.3 Energy gradients as a function of the total arc length L_{tot} of collapsed wrinkles supported by: (a) Cu(111) substrate, and (b) Ni(111) substrate. The coloured lines denote the energy gradients for Conformation A and the black line denotes the energy gradient for B, where the intersection point gives the length L_{B} for each value of γ. 155

6.4 The behaviour of the total energy E_{tot} as a function of the total arc length L_{tot} for different wrinkle configurations with bending rigidity $\gamma = 1.2\,\text{eV}$ supported by Cu(111) substrate. The marked point denotes the critical length L_{crit} where the self-adhered wrinkle folds and follows Conformation B. 157

6.5 The behaviour of the total energy E_{tot} as a function of the total arc length L_{tot} for self-adhered wrinkles (solid lines) and Conformation B of collapsed wrinkles (dashed lines) supported by: (a) Cu(111) substrate, and (b) Ni(111) substrate. The marked points denote the critical lengths L_{crit} where self-adhered wrinkles fold and follow Conformation B. 158

6.6 The conformation of collapsed wrinkles supported on: (a) Cu(111), and (b) Ni(111) substrate for different bending rigidities with $L_{\text{tot}} = L_{\text{crit}}$. 159

6.7 The conformation of collapsed wrinkles supported on Cu(111) and Ni(111) substrate with fixed arc length $L_{\text{tot}} = 180\,\text{Å}$ and bending rigidity $\gamma = 1.2\,\text{eV}$. 161

7.1 Graphene configurations investigated in this thesis: (a) single-layer ripples, (b) supported multi-layer folds, (c) unsupported multi-layer folds, and (d) collapsed wrinkles. 167

7.2 (a) Frequently and (b) occasionally observed graphene conformations. Taken from Ref. [8] under a Creative Commons Attribution 4.0 International License. 173

Abstract

The rapidly increasing use of graphene-based nanomaterials in nanotechnology has led to considerable research interest in many disciplines, including applied mathematics, solid-state physics, and material engineering. One of the main contributions of applied mathematics in this regard is the application of mathematical models that improve our understanding of the formation and geometry of these intricate nanomaterials. In this thesis, we develop a collection of mathematical models that together provide detailed and convincing explanations for several graphene nanostructures. The calculus of variations is employed to construct and analyse these models, and the Lennard-Jones potential is used to model the van der Waals interaction energy. While the modelling process involves a number of physical parameters, nondimensionalisation is employed to reduce the number of these parameters and produce simplified problems with the minimum number of arbitrary material constants. The first model is developed to investigate the behaviour of a rippled graphene sheet located on a substrate. By considering the length of the substrate, three distinct cases for this configuration are identified. The transitional case assumes that both the graphene sheet length and substrate length are constrained. The substrate constrained case assumes that only the substrate has a constrained length. Finally, the graphene constrained case assumes that only the length of the graphene sheet is constrained. These cases

are employed to demonstrate a continuous relationship between the total energy per unit length and the substrate length. The substrate constrained case is also used to examine the ripple formation in a flat graphene sheet laying on a shrinking substrate. The next model pertains to the conformation of multi-layer graphene folds. The conformation is analysed under three progressively more accurate approximations for the total line curvature, and a comparison to experimental measurements is made. With some modifications, this model is then extended to predict the effective bending rigidity of multi-layer graphene. The analysis predicts that for less than seven layers the bending rigidity of multi-layer graphene approximately follows a quadratic relationship with the number of layers. The final model is specialised for the collapsed graphene wrinkle, the most intricate and complicated structure considered in this thesis. Using this model, we account for two potential conformations for collapsed wrinkles. The stability of these conformations along with a self-adhered wrinkle is analysed through an energy comparison of the wrinkle both before and after collapse. We report numerical values for both the length when each conformation becomes stable, and the critical height of self-adhered wrinkles. In summary, the major contribution of this work is the use of applied mathematics to develop idealised variational models for a number of graphitic nanomaterial configurations. The models developed here enhance our knowledge of the geometry of these structures and may be utilised for modelling more complicated structures constructed from graphene and other two-dimensional materials. In particular, the novel formulae developed in this work, such as those derived for modelling the surface–volume interaction energy and the total squared curvature, broaden the scope of applied mathematical modelling in nanoscience.

Thesis Declaration

I certify that this work contains no material which has been accepted for the award of any other degree or diploma in my name, in any university or other tertiary institution and, to the best of my knowledge and belief, contains no material previously published or written by another person, except where due reference has been made in the text. In addition, I certify that no part of this work will, in the future, be used in a submission in my name, for any other degree or diploma in any university or other tertiary institution without the prior approval of the University of Adelaide and where applicable, any partner institution responsible for the joint-award of this degree.

I acknowledge that copyright of published works contained within this thesis resides with the copyright holder(s) of those works.

I also give permission for the digital version of my thesis to be made available on the web, via the University's digital research repository, the Library Search and also through web search engines, unless permission has been granted by the University to restrict access for a period of time.

Signed: Jabr Aljedani Date: 13/09/2022

Acknowledgements

This work would not have been completed without the enormous support of a multitude of individuals and funding bodies. First and foremost, I would like to express my deepest gratitude and appreciation to my Principal Supervisor, Dr Barry Cox. Without his tireless assistance, great patience, invaluable guidance, and efficient supervision, this thesis would not have been possible. His jokes and improvisational sense of humour made our supervision meetings enjoyable and also helped me to overcome my negative energies, especially during the first year of my candidature. Even after his retirement in February 2020, continuing his supervision to the end of my candidature, which definitely will never be forgotten, has empowered me to make the best work I possibly can. My gratitude is also extended to my Co-Supervisor, Dr Michael Chen, for his insightful ideas, useful comments, and continued encouragement. He was always willing to help whenever I asked for assistance, particularly with anything related to technology.

I must thank King Abdulaziz University for the award of a fully funded scholarship which enabled me to undertake my research at the University of Adelaide. My acknowledgements are also extended to the School of Mathematical Sciences at the University of Adelaide for providing a good study environment, and also funding my conference registrations and travel. I wish once more to express my appreciation to those who helped in editing this the-

sis, Dr Emma McEwin (the editor) and the Faculty of Sciences, Engineering and Technology (the funding source).

Time to acknowledge my small family here in Australia: my lovely wife, Bdoor; my brave son, Wesam; and my beautiful daughter, Joann. I would not have been able to afford to undertake this endeavour without their constant love, support, and tolerance. My acknowledgements would not be complete without thanking my beloved family in Saudi Arabia, my mother, my father, my brothers, my sisters, my nephews, and my nieces for their unlimited support, prayers, and faith. My warmest thanks are due to my mother who daily advised and encouraged me to overcome any difficulties I faced throughout my experience studying abroad.

Special thanks go to my friends, here in Australia and there in Saudi Arabia, who have been unfailing sources of encouragement, advice, and reassurance. I also welcome this opportunity to thank Manssor Alshehri, M. B. Almatrafi, and Hammad Alotaibi, who guided me to an ideal supervisor, Dr Barry Cox. Last but not least, I should acknowledge Dr Paul Eloe from the University of Dayton in United States, for the valuable assistance in completing my admission application at the University of Adelaide.

Dedication

After seven years of being physically away from my mother, my father, my brothers, my sisters, my nephews, and my nieces; I dedicate this thesis to all of these people.

Chapter 1

Introduction

1.1 Background

Applied mathematics provides powerful tools that may be used to describe and explain real-world problems in many fields such as medicine, engineering, and science. Applied mathematical modelling generally comprises four main stages. The first stage involves determining the scientific problem and all related factors. The next stage is to construct the model by describing the scientific problem with a mathematical formulation. Thereafter, the mathematical analysis is applied to find the solution of the mathematical formulation using appropriate mathematical techniques. The final stage entails validating the proposed model. One possible technique to validate solutions is the comparison with other published experiments or measurable environmental phenomena. In recent decades, applied mathematical modelling also plays a significant role in the research active field of nanotechnology.

Nanotechnology is a field that comprises the intersection of several disciplines, such as physics, chemistry, material science, engineering, and mathematics, to investigate and explain phenomena of nano-scaled materials.

Nano-scaled materials, commonly termed "nanomaterials", have structures in the order of nanometres in scale, where one nanometre is one billionth (10^{-9}) of a meter. Mathematical modelling is an important component of studying nanomaterials and may be applied to advance knowledge in many ways. Mathematical modelling of nanomaterials may be employed to explain experimental results, improve the efficiency of experimental design, predict new behaviours, and discover hidden properties. In this thesis, we develop mathematical models for various configurations of graphene, one of the leading nanomaterials.

1.2 Graphene properties and applications

With reference to Fig. 1.1, graphene may be defined as a two-dimensional (2D) sheet of carbon atoms which are bonded to each other in a locally planar hexagonal array. This 2D structure endows graphene with superior electronic [9], mechanical [10], and thermal properties [11, 12]. These properties mean that graphene is one of the most promising materials for constructing nanoelectromechanical systems [13, 14]. Graphene is also hypothesised to be a biocompatible material since its bending stiffness is comparable with that of the lipid bilayers of biological cells [15]. In the field of biomedicine, graphene has many potential applications, including drug transport systems, sensors, tissue engineering, and biological agents [16]. The many applications of graphene also include, but are not limited to, water treatment [17], gas separation [18], nitrogen reduction reaction [19], and metal-ion batteries [20]. Furthermore, other graphitic nanostructures, such as fullerenes and carbon nanotubes, attract widespread interest due to their unique properties, which make them fundamental components in nanoelectronic devices such as field

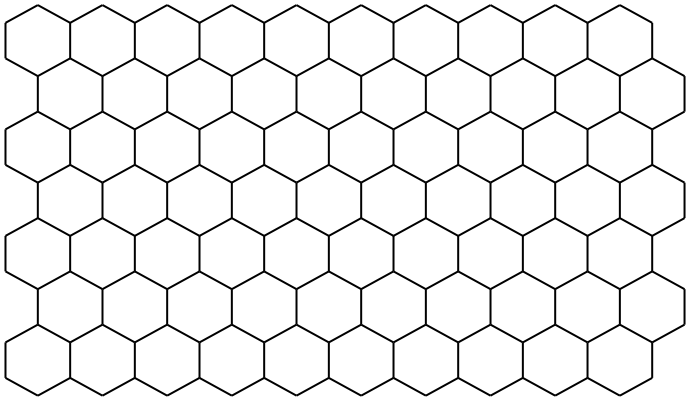

Figure 1.1: The structure of a graphene sheet.

effect transistors [21] and capacitors [22].

Graphene may be considered an important building material for other carbon nanostructures since many carbon allotropes are structurally based on the planar graphene sheet [1]. With regard to Fig. 1.2, a fullerene can be considered to be a graphene sheet wrapped up into a ball [23], and a single-walled carbon nanotube is essentially a graphene sheet rolled up as a tube [24]. While multi-layer graphene is composed of stacked single-layer sheets of graphene, multi-walled carbon nanotubes then may be considered to be rolled up multi-layer graphene sheets. Additionally, novel carbon nanostructures have been designed by reconfiguring graphene in ways that result in these new structures having desirous properties [20]. For example, popgraphene is a reconfigured graphene that is a beneficial anode material in lithium-ion batteries with fast charge and discharge rates [25]. The bending rigidity of graphene is shown to directly impact its properties [26], and consequently, it is a key factor in the construction of novel carbon nanostructures and

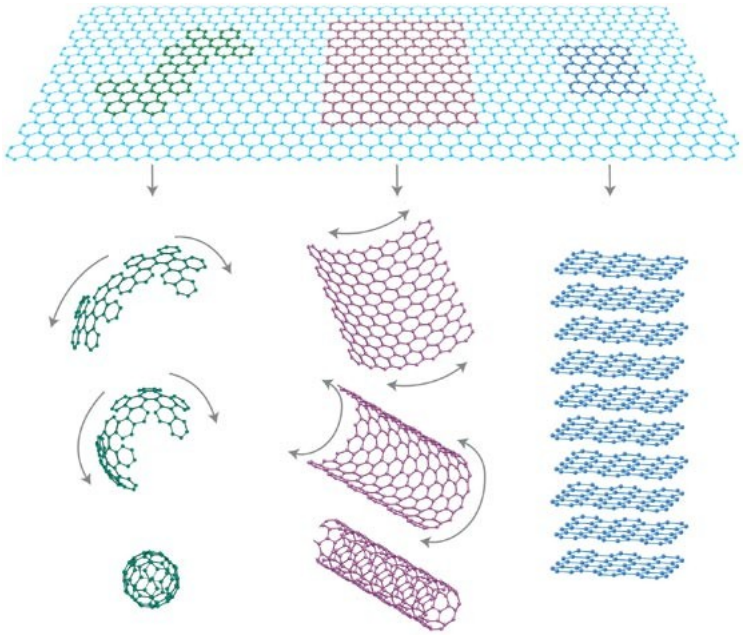

Figure 1.2: Graphene-based nanomaterials [1].

investigating their properties.

The bending rigidity of single-layer graphene has been theoretically analysed in depth. Density functional theory calculations are employed to evaluate the bending rigidity of a single-layer graphene to be 1.44 eV [15]. Other theoretical approaches, including empirical potential methods [27, 28] and *ab initio* calculations [29, 30], are also employed to estimate the bending rigidity of single-layer graphene. These theoretical studies suggest that the bending rigidity of single-layer graphene lies in the range from 0.83 eV to 1.61 eV, and these estimates are analysed in detail by Wei et al. [15]. The experimental study undertaken by Nicklow et al. [31], reports that the bending rigidity of single-layer graphene is 1.2 eV. This experimental measurement fits the theoretically reported range very well. Table 1.1 presents some values for the bending rigidity γ of single-layer graphene sheet that have been reported in

the literature. However, while the bending rigidity of single-layer graphene is relatively well characterised, further investigation is needed to investigate the bending rigidity of multi-layer graphene since there is still considerable uncertainty with regards to this property.

1.3 Graphene synthesis methods

Various methods are used to synthesise graphene, which can be classified into two broad approaches as illustrated by Fig. 1.3. The first approach relies on breaking down graphene precursors into few layers of graphene, this is known as the top–down approach. Graphite (a stack of graphene layers) is one such graphene precursor, and several methods exfoliate graphite into graphene by chemical, mechanical or thermal manipulations. For instance, the intercalation of chemical species between graphite layers is used to weaken the interlayer van der Waals (vdW) interactions and increase the distance between layers [35]. The second approach is known as bottom–up and relies on building a block of carbon molecules to produce graphene. The meth-

Table 1.1: The bending rigidity γ of single-layer graphene sheet.

Reference	γ (eV)	method
[27]	0.83	empirical potential
[32]	1.02	empirical potential
[33]	1.17	empirical potential
[31]	1.20	experiments
[15]	1.44	density functional theory
[34]	1.61	density functional tight-binding model

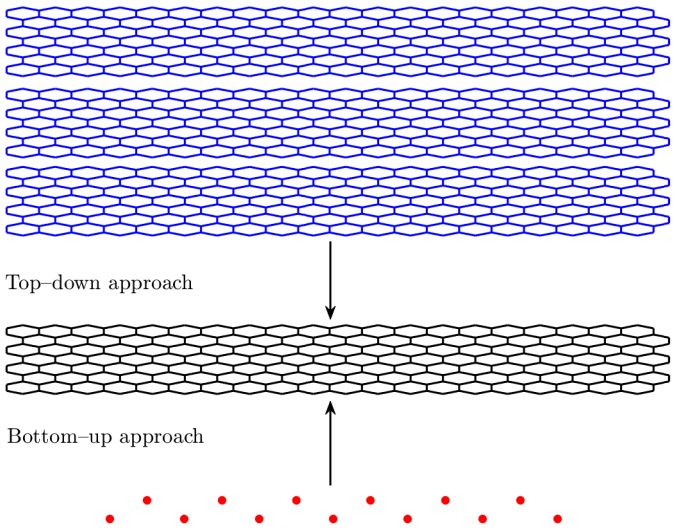

Figure 1.3: Schematic showing the top–down and bottom–up approaches of graphene synthesis.

ods that follow the bottom–up approach include chemical vapour deposition (CVD), which can be used to produce graphene with controllable thickness and quality.

The CVD bottom–up approach is a commonly used method to synthesise graphene with a large surface area and high quality. In this method, graphene is grown on a substrate in a carbon-rich environment based on depositing gaseous reactants onto the substrate. The CVD process takes several steps, which are detailed in [36]. One step involves cooling the reactant in a neutral environment. Although some progress has been made to control the growth of graphene during the cooling step, some topological deformations in the graphene structure have been observed [37, 38]. These deformations may form as a result of the natural roughness of the substrate [39], and differential thermal expansion of the substrate and the graphene [40]. Representative plots for the observed deformations are given in Fig. 1.4.

The deformations of CVD-produced graphene may be categorised as ripples and wrinkles based on their aspect ratio, physical dimensions, and topology [41]. The low aspect ratio deformations with a maximum height of 1 nm are termed by ripples [42]. After the ripple reaches its maximum height, the edges of the ripple are found to approach each other forming an arch-shaped wrinkle. Then, due to the vdW interactions, the two edges self-adhere at the equilibrium distance of a graphene bilayer forming a high aspect ratio deformation which we term in this work a self-adhered wrinkle [38]. The self-adhered wrinkle remains standing until the critical height is reached, at which point it folds towards the surface and forms a structure that we term the collapsed wrinkle [38]. The presence of such deformations alters the properties of the graphene, such as electrical mobility [38], thermal conductivity [43, 44], and strain sensitivity [45].

1.4 Graphene configurations

Non-planar structures of graphene possess many unique and useful properties, compared to planar graphene. This widens the range of applications that could exploit these properties. Experimental studies find that the electronic properties of graphene can be altered by the range and height of the ripple [46, 47]. Gui et al. [48] use first-principles calculations to predict the electronic properties of a rippled graphene sheet where a band gap opening is observed in the rippled graphene. They evaluate a direct band gap of 0.93 eV which indicates rippled graphene may be a highly tunable semiconductor. Furthermore, wrinkled graphene is shown to be a beneficial material in the fabrication of graphene nanoribbons and flexible electronic sensors [49, 45].

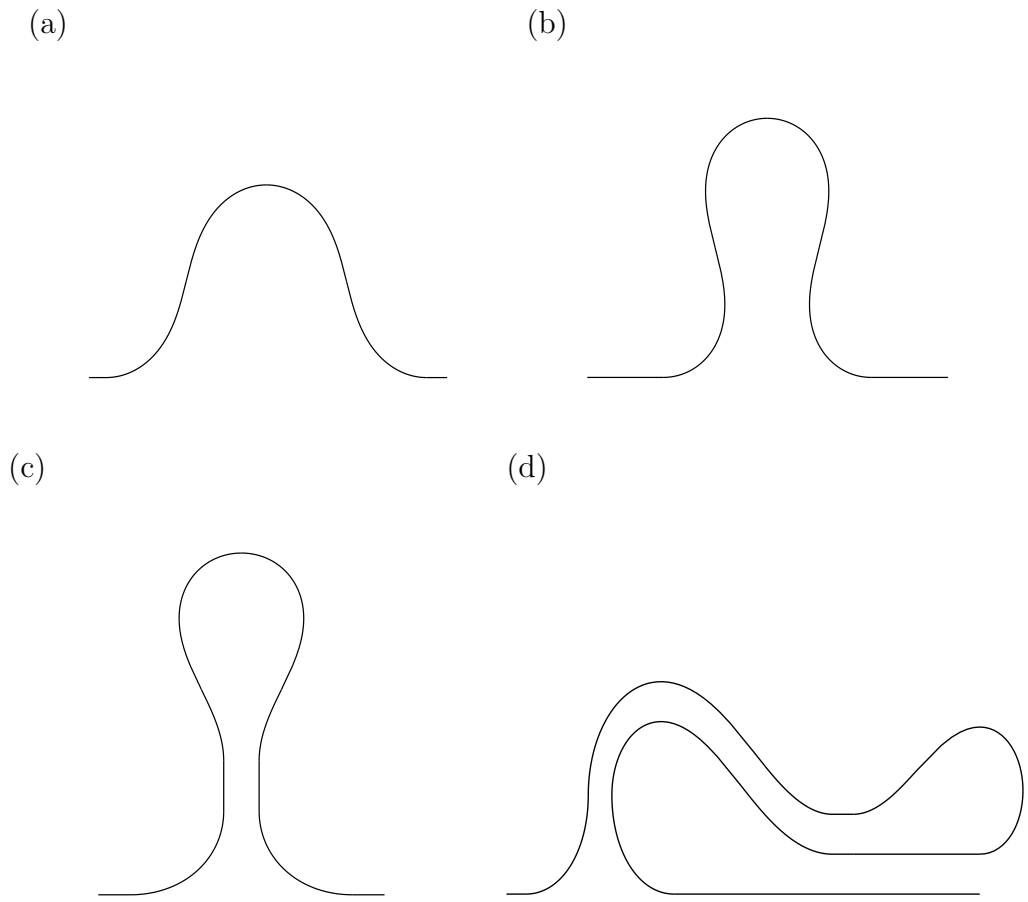

Figure 1.4: Observed configurations in CVD-produced graphene:
(a) ripples, (b) arch-shaped wrinkles, (c) self-adhered wrinkles, and (d) collapsed wrinkles.

Another important type of graphene configuration is the closed-edge graphene structure, or simply the folded graphene. Some techniques, such as applying a mechanical force, have been used to fold 2D materials into specific structures in order to achieve desirable properties. Although graphene is known in one sense as the strongest known material [10], it may also be folded and unfolded repeatedly via the tip of an atomic force microscope [50, 51]. Graphene folding is involved in the process of constructing graphene origami,

a programmable nanoscale building block [52, 53, 54, 55].

Understanding the formation of these and related structures and controlling their morphologies plays a significant role in tuning the properties of graphene-based structures. Such structures of graphene are likely to be important components with potential applications in many areas of nanotechnology. Many theoretical studies have proposed mathematical models for non-planar structures of graphene. In the next section, we trace the history of modelling graphitic nanostructures.

1.5 Modelling graphene configurations

The behaviour of graphene configurations is principally governed by two energies, the bending elastic energy and the vdW energy. Based on these energy components, several mathematical models have been proposed for graphene configurations. In many cases, the mathematical model is presented with a comparison to molecular dynamics (MD) simulations or experiments to validate the proposed model. One configuration that has received significant attention is that of folded graphene; however, similar models are also applicable to other configurations such as ripples and wrinkles. The main approaches that have been used to model folded graphene include small-deformation, finite-deformation, and variational models.

In order to clearly introduce each approach, it is necessary to provide some data for folded graphene. As shown in Fig. 1.5, most studies assume a translational symmetry in the fold direction and a reflective symmetry about the x–axis, which simplify the modelling. Experimental and theoretical studies show that the conformation of folded graphene is determined by the bending energy and the vdW interaction strength in the flat region. If the

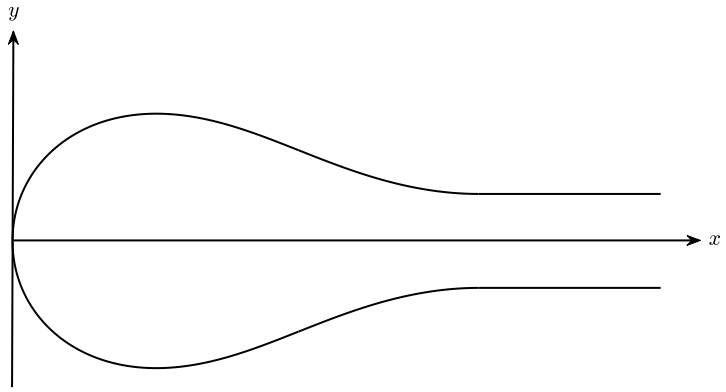

Figure 1.5: Schematic showing the geometry of folded single-layer graphene.

vdW energy in the flat region exceeds the bending energy in the curved region then the fold would be energetically stable, and if not then the configuration is unstable. Therefore, the stability of the fold depends on (among other factors) the length of the graphene sheet. Next, a brief overview of each approach is presented along with the assumptions that have been made in each case.

1.5.1 Small-deformation approach

Cranford et al. [56] study the folding behaviour of single- and multi-layers graphene by developing a small-deformation model along with an atomistic simulation. They employ molecular dynamics to obtain values for a set of parameters including the equilibrium distance between two graphene sheets $2\delta_{\mathrm{gg}}$, and the vdW interaction energy ϵ_{gg}. The Tersoff potential is used to account for carbon–carbon interactions, with the Lennard-Jones (LJ) potential

used for the interactions between graphene sheets.

With the help of the reflective symmetry, the total length of the folded graphene is $L_{\text{tot}} = 2\,(L_{\text{bend}} + L_{\text{flat}})$, where L_{bend} and L_{flat} represent the arc length of the bended and flat regions, respectively. They assume that the folding configuration is due to a balance between the elastic bending energy E_{e}, and the vdW energy E_{v}. The total energy of the system is then the sum of these energies, namely $E_{\text{tot}} = E_{\text{e}} + E_{\text{v}}$.

These authors assume that graphene can be approximated as a beam composed of an elastic isotropic material with the presence of local small deformations. If $y(x)$ represents the deflection of the beam at the point x, then the deformed beam angle or the slope is

$$\theta = \frac{\mathrm{d}y}{\mathrm{d}x}.$$

With the presumption of the small slope θ, the square of the slope is assumed to be equal to zero which yields

$$\left(\frac{\mathrm{d}y}{\mathrm{d}x}\right)^2 = 0.$$

As a consequence, they define the elastic bending energy as

$$E_{\text{e}} = 2\gamma \int_{L_{\text{bend}}} y''^2 \,\mathrm{d}x\,,$$

where primes denote derivatives with respect to x, and γ denotes the bending rigidity of the graphene sheet. The bending rigidity γ is calculated based on energy minimisation of the system using conjugate gradient methods. The vdW energy is calculated to be

$$E_{\text{v}} = \epsilon_{\text{gg}}\, 2L_{\text{flat}}.$$

The Euler–Bernoulli beam theory is then applied to derive the total energy of the system as

$$E_{\text{tot}} = \frac{2\gamma\pi^2}{L_{\text{bend}}} + 2L_{\text{bend}} - \gamma L_{\text{tot}}.$$

The energy is therefore minimised to find the critical bended length $2L_{\text{bend}}$ as

$$L_{\text{bend}} = \pi\sqrt{\frac{\gamma}{\epsilon_{\text{gg}}}}.$$

Along with the small-deformation model, they also employ an atomistic simulation in the analysis by developing a coarse-grained model where pseudo-atoms are used to represent groups of atoms. Although the coarse-grained model confirms the relationship between the bending rigidity γ and the bended length L_{bend} obtained from the small-deformation model, the predicted folding profiles are not presented in this study.

1.5.2 Finite-deformation approach

Meng et al. [2] study the self-folding of single-layer graphene using finite-deformation beam theory and molecular MD simulations. Due to the reflective symmetry, only the top-half is analysed. Similar to the small-deformation model, the total length is $L_{\text{tot}} = 2\,(L_{\text{bend}} + L_{\text{flat}})$, and the total energy is $E_{\text{tot}} = E_{\text{e}} + E_{\text{v}}$. These authors argue that the small-deformation model cannot accurately predict the shape of the folded graphene. The elastic energy is modelled by the small-deformation model as a beam with the presumption of small slopes. The finite-deformation model, however, accounts for large slopes.

Graphene is modelled with a finite-deformation approach as a beam with bending rigidity γ. They give the equilibrium equations of the beam by

$$\frac{\mathrm{d}M}{\mathrm{d}s} + V = 0, \quad \frac{\mathrm{d}V}{\mathrm{d}s} + N\frac{\mathrm{d}\theta}{\mathrm{d}s} = 0, \quad \frac{\mathrm{d}N}{\mathrm{d}s} - V\frac{\mathrm{d}\theta}{\mathrm{d}s} = 0, \tag{1.1}$$

where M is the bending moment, V is the shear force and N is the normal force within the beam. Using the Euler–Bernoulli beam theory, the bending moment is written as $M = \gamma\kappa$, where $\kappa = \mathrm{d}\theta/\mathrm{d}s$ is the curvature. Using the

expression for M, the shear force V is eliminated from (1.1) and the number of equations is reduced to the pair of equations

$$\frac{\mathrm{d}N}{\mathrm{d}s} + \gamma \frac{\mathrm{d}}{\mathrm{d}s}\left(\frac{\mathrm{d}\theta}{\mathrm{d}s}\right)\frac{\mathrm{d}\theta}{\mathrm{d}s} = 0, \tag{1.2}$$

$$N\frac{\mathrm{d}\theta}{\mathrm{d}s} - \gamma \frac{\mathrm{d}^2}{\mathrm{d}s^2}\left(\frac{\mathrm{d}\theta}{\mathrm{d}s}\right) = 0. \tag{1.3}$$

An expression for the normal force N is then derived by integrating (1.2) with respect to s which gives

$$N = -\frac{\gamma}{2}\left(\frac{\mathrm{d}\theta}{\mathrm{d}s}\right)^2 + N_0,$$

where N_0 is a constant of integration. Then the expression for N is substituted into (1.3) to yield an equation that only depends on $\kappa = \mathrm{d}\theta/\mathrm{d}s$. The bending energy can then be calculated using the expression for κ.

A comparison between the predicted folding profiles obtained from the small-deformation model, finite-deformation model and MD simulations is made by Meng et al. [2] in Fig. 1.6(a). The finite-deformation model and MD simulations simulations are in good agreement when predicting the folding profile, while the small-deformation model predicts a folding profile with a sharp discontinuous point. This is a consequence of the different approximate expressions of the slope used in each model. The finite-deformation model uses the approximate expression of the slope as $\sin\theta = \mathrm{d}y/\mathrm{d}s$, while the small-deformation model uses $\theta = \mathrm{d}y/\mathrm{d}x$ instead. As shown in Fig. 1.6(b), they examined the shape under different folding directions ranging from a direction with chiral angle 0° (armchair) to a direction with chiral angle 30° (zigzag). Their analysis also reveals that the folding direction does not strongly impact the profile of the fold. Finite-deformation beam theory, combined with MD simulations, is also used to study the self-folding of multi-layer graphene [57].

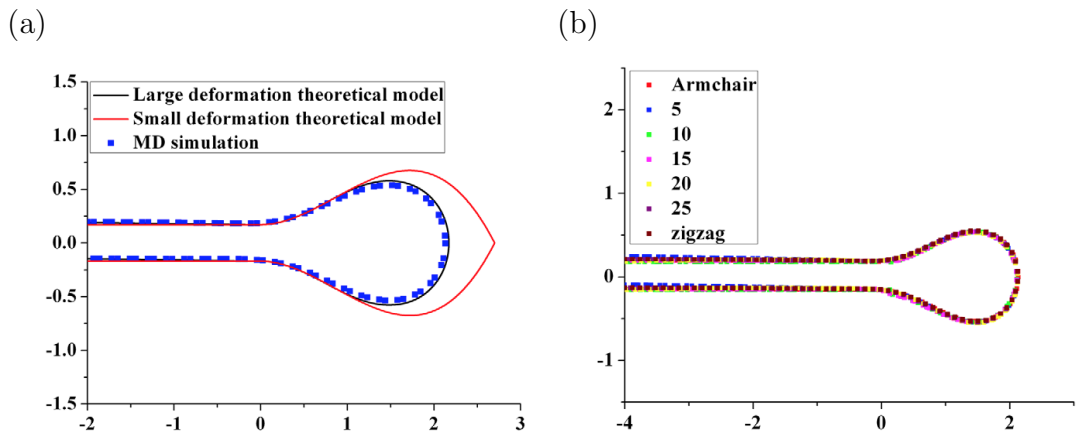

Figure 1.6: Comparisons in the predicted folding profiles between: (a) small- and finite-deformation models against MD simulations, and (b) different folding directions. Republished with the permission of IOP Publishing Ltd, from Ref. [2]; permission conveyed through Copyright Clearance Center Inc.

1.5.3 Variational approach

The folding behaviour of a single-layer graphene sheet is also investigated by Cox et al. [3] utilising the calculus of variations. They only analyse the top-half curve denoted by C. The curve C is further divided into three parts according to the sign of the curvature. The bended region is composed of C_1 and C_2 which correspond to the parts with negative and positive curvature, respectively. The flat region with zero curvature is designated C_3. The total energy of the system $E_{\text{tot}} = E_{\text{e}} + E_{\text{v}}$, is derived from variational considerations as a functional of the conformation profile $y(x)$ and its derivatives. They assume that the conformation is determined by minimising the elastic energy and maximising the vdW interaction energy.

The elastic energy is considered to be proportional to the square of the

curvature, and modelled as

$$E_{\mathrm{e}} = \gamma \int_C \kappa^2 \, \mathrm{d}s \,,$$

where κ represents the line curvature and is given by

$$\kappa = \frac{y''}{(1 + y'^2)^{3/2}}.$$

Thus, E_{e} vanishes at the parallel regions ($y' = 0$) where the vdW is considered to be the dominant energy. The vdW energy is modelled as

$$E_{\mathrm{v}} = -\epsilon_{\mathrm{gg}} \int_C u(x) \, \mathrm{d}s \,,$$

where $u(x)$ is a Heaviside unit step function. By imposing an isoperimetric constraint on the total arc length, the total energy E_{tot} is reduced to account for the elastic curve with an unknown endpoint. Variational calculus is then employed to derive and solve the Euler–Lagrange equation and derive an explicit expression for the curvature κ which involves the term y'. The substitution $y' = \tan\theta$ is then used to derive parametric solutions for the folding conformation.

The analytical solution involving elliptic integrals is presented as a function of γ. Then different values for the bending rigidity γ are adopted from the range 0.8–1.6 eV. The predicted folding conformations show good agreement with experimental images taken by high-resolution transmission electron microscopy [58], as shown in Fig. 1.7. This approach is then extended to model the intercalation of a single-walled carbon nanotube situated in a fold of graphene sheet [59]. The variational model is largely equivalent to the approach used by Lu and Chou [60], to investigate the geometrical characteristics of self-folded carbon nanotubes.

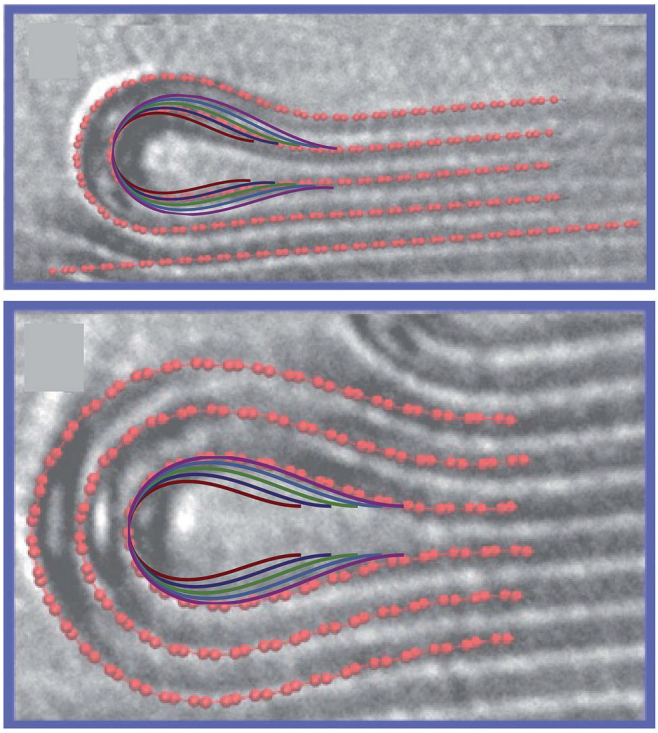

Figure 1.7: Folding conformations obtained from the variational approach (coloured solid lines, each for a different value of γ) are compared to experimental results (red dotted lines). Reproduced from Ref. [3] with permission from the Royal Society of Chemistry.

1.5.4 Quasi-analytical approach

The quasi-analytical approach has been applied to graphene self-adhered and collapsed wrinkles. A 90 degree anticlockwise rotation of the top-half of the self-adhered wrinkle shown in Fig. 1.4(c) produces an equivalent shape to that given by Fig. 1.5. Therefore, this approach can still be compared to the above-mentioned approaches. The quasi-analytical approach is first employed by Zhu et al. [38] where the bended region of the self-adhered wrinkle is approximated by two pairs of circular arcs. Each half is composed of a concave arc followed by a convex arc.

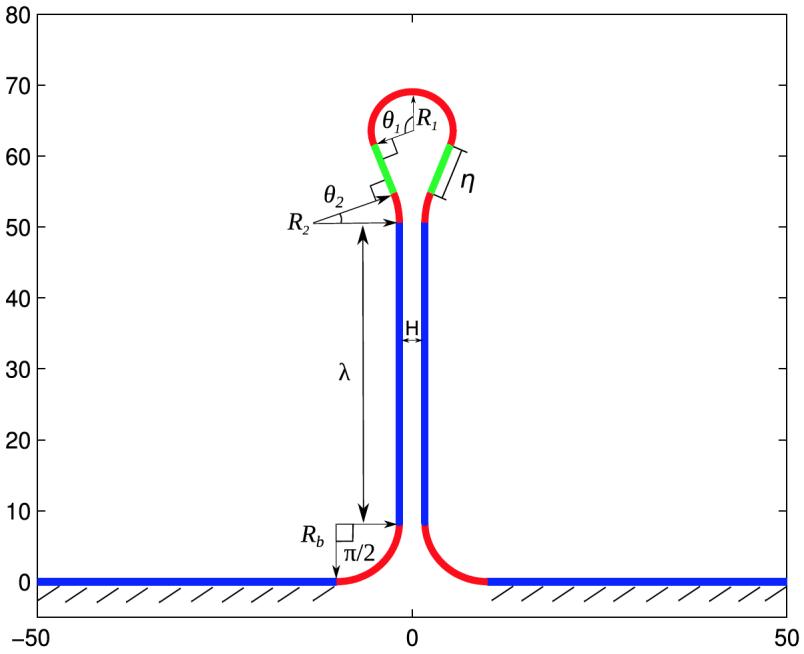

Figure 1.8: The geometry of a self-adhered wrinkle. Reprinted from Ref. [4], with the permission of AIP Publishing.

The approach has been subsequently extended by Zhang et al. [4] with two different modifications for deriving the length and the energy of the folded wrinkles. Transition lines are introduced between any concave and convex arcs, and the effects of the metallic substrate are ignored. We now give some details on modelling the self-adhered wrinkle using the quasi-analytical approach. The geometry of the self-adhered wrinkle considered by Zhang et al. [4] is shown in Fig. 1.8. The top-curved regions are approximated by the arcs of radii R_1 and R_2 with angles θ_1 and θ_2. Furthermore, a linear transition η is incorporated to accommodate the transition between the two adjacent arcs. The length of the vertical lines is denoted by λ, while the bottom-curved regions are approximated by arcs of a radius R_b with an angle $\pi/2$.

In their study, each arc is assumed to be circular with a fixed radius along the arc. Since the curvature is the inverse of the radius, the total energy of the wrinkle E_{tot} is then estimated by

$$E_{\text{tot}} = \frac{\gamma}{2}\left(\frac{\pi}{R_{\text{b}}} + \frac{2\theta_1}{R_1} + \frac{2\theta_2}{R_2}\right) - \epsilon_{\text{gg}}\lambda,$$

where the first term represents the elastic energy E_{e} and the second term represents the vdW energy. They also calculate the excess length L_{tot}, which is the length the wrinkle without the fixed length interacting with the substrate. The excess length is given by

$$L_{\text{tot}} = 2\left(\frac{\pi}{2}R_{\text{b}} + \theta_1 R_1 + \theta_2 R_2 + \eta + \lambda\right).$$

They adopt a fixed value for the excess length L_{tot}, and then minimise the total energy E_{tot} with respect to the parameters R_{b}, R_1, θ_1, R_2, θ_2, η, and λ. Besides the self-adhered and collapsed wrinkles, they also study the behaviour of multiple-folded collapsed wrinkles.

1.5.5 Other approaches

The approaches mentioned above consider perfect graphene with uniform thickness distribution. However, the geometry variation with additive–layer segments, or material impurity with residual contaminants, may lead to imperfect graphene. The main difference in the modelling is to account for the elastic energy of the impure region for the imperfect graphene, but this elastic energy vanishes in the perfect graphene. Li et al. [61] employ small- and finite-deformation beam theory with geometry assumptions to investigate the non-uniform effect on the global-buckling behaviour and local-folding phenomenon. An extension was further developed by Li et al. [5] utilising a finite-deformation varying–section beam model to model non-uniform self-folding

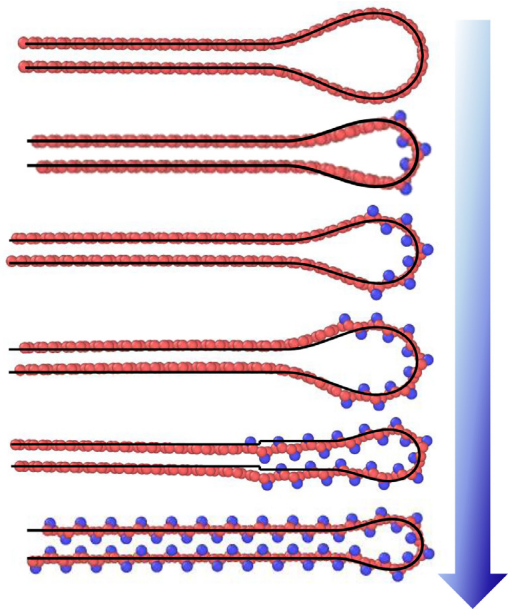

Figure 1.9: Folding conformations of perfect and imperfect graphene. Reprinted from Ref. [5], with permission from Elsevier.

of impure graphene. While perfect graphene yields a unique folded configuration, there might be different geometries for folded imperfect graphene, depending on the length of the impure region. As shown in Fig. 1.9, the folding conformation of a perfect sheet of graphene is given at the top, then several folding conformations are given for imperfect graphene, varying the length of the impure region. It is clear that the increase of the imperfection region flatten the folding conformation of graphene, leading to an approximate flat stack of graphene.

Besides mathematical modelling, experimental studies have also investigated the morphologies of graphene. Chen et al. [7], apply atomic force microscopy to study the folding behaviour of supported multi-layer graphene. They report experimental measurements of the hump height, that is the height from the point where the folding edge becomes flat to the maximum

height obtained. Based on these measurements, they calculate the bending rigidity of multi-layer graphene using continuum mechanics theories. Another experiment for graphene wrinkles is reported by Wang et al. [6], where unexpected profiles of graphene wrinkles on copper (Cu) substrate are observed. The widths of those wrinkles are in the range of tens of nanometres, whereas the heights are in the range of a few nanometres. As they reported, the presence of interlayer molecules between the graphene and the copper substrate is the main mechanism that enlarges both width and height of graphene wrinkles.

In this work, we aim to develop a cogent collection of mathematical models to enable detailed explanations for different graphene structures. While most of the approaches mentioned earlier are compared to simulations, the variational approach is especially promising due to the agreement with experiments rather than simulations. The models developed in this work are based on the variational approach, and detailed information about the calculus of variations are provided in the next chapter.

1.6 Thesis structure

This thesis entitled "New Variational Models for Graphene-based Nanomaterials" comprises seven chapters as follows:

- The first chapter outlines the importance of graphene, its properties, and applications. Graphene synthesis methods are also discussed to explain the formation of non-planar structures of graphene. This chapter is wrapped up by giving some historic approaches of modelling graphene configurations detailed in Section 1.5.

- The second chapter presents the mathematical methodology used in

this work. The theoretical approach is described first in Section 2.1, which includes the use of calculus of variations and other mathematical techniques. The modelling approach is then described in Section 2.2, including the use of LJ potential to model the vdW interaction energy and the modelling approach for the dominant energies.

- The third chapter develops the first variational model to study the behaviour of a rippled graphene sheet. Three different configurations of a rippled graphene sheet located on a flat substrate are examined. We derive a general formulation for these configurations which leads to the discovery of a smooth transition between them. The model unifies all three cases in Section 3.6 to demonstrate a continuous relationship between the total energy per unit length and the substrate length. Finally, a comparison is made with earlier published results from molecular dynamics simulations and the model shows excellent agreement in so far as predicting the profiles of graphene ripples.

- The fourth chapter proposes a novel mathematical model for a fold of supported multi-layer graphene sheets. Taylor series approximations are used to derive a general expression for the total squared curvature. Then, we investigate the effects of three degenerate approximations on the folding conformation of multi-layer graphene. In Section 4.6, the results from the model are compared to experimental measurements of multi-layer graphene folds from the literature. The model shows improved agreement with the experimental measurements as we include more terms in the Taylor series approximations of the total squared curvature.

- In the fifth chapter, we exploit the model developed in the fourth chap-

ter to model a fold of unsupported multi-layer graphene sheets. A simplified solution for the fold of unsupported multi-layer graphene sheets is also proposed. These solutions are then used to predict the effective bending rigidity of multi-layer graphene. For less than seven layers, the model shows an approximate quadratic relationship between the effective bending rigidity and the number of layers, and this relationship is confirmed by a log-log plot in Section 5.5. This prediction supports some theoretical and experimental studies reported in the literature.

- The sixth chapter presents a variational model to investigate the behaviour of collapsed graphene wrinkles. Two potential conformations of collapsed wrinkle are taken into account and the required length for each conformation to be favoured is determined. We also predict the critical height of self-adhered wrinkles by comparing the energy cost of self-adhered wrinkles to that of collapsed wrinkles. In Section 6.5, numerical data is presented for the heights, lengths, and energies of these wrinkles at the stable conformation. These results are consistent with the experimental and theoretical studies in the literature.

- The seventh chapter contains a summary, concluding remarks, and possible future works. Following this are an appendix and bibliography.

Each chapter is followed by a nomenclature section listing the symbols used in that chapter. We note that some symbols appear with different definitions from one chapter to another; and thus, a nomenclature table is provided at the end of each chapter for the reader's convenience.

1.7 Nomenclature

Symbol	Description
$2\delta_{\mathrm{gg}}$	the graphene–graphene equilibrium distance
ϵ_{gg}	the graphene–graphene vdW interaction strength
L_{tot}	the total arc length of the conformation
L_{bend}	the length of the bended regions of the conformation
L_{flat}	the length of the flat regions of the conformation
E_{tot}	the total energy of the conformation
E_{e}	the graphene elastic energy
E_{v}	the vdW interaction energy
$y(x)$	the deflection of the beam or folding profile at the point x
$\square'$	the derivative of $\square$ with respect to x
θ	the deformed beam angle or the slope
γ	the bending rigidity of graphene
M	the bending moment within the beam
V	the shear force within the beam
N	the normal force within the beam
N_0	a constant of integration
κ	the line curvature
s	the arc length of a curve
$u(x)$	a Heaviside unit step function
θ_i/R_i	the angle/radius of the circular arc i
η	the transition line between any adjacent circular arcs
λ	the length of the vertical layers in self–adhered wrinkles

Chapter 2

Mathematical methodology

2.1 Theoretical approach

2.1.1 Line curvature representations

This work focuses on modelling configurations of graphene based on interactions with other nanostructured materials. These configurations are potentially curved, so it is necessary to introduce the mathematical definition of line curvature. Curvature is simply a measure of how much a curve bends. Formally, the curvature of a plane-curve κ may be defined as the rate of change in the tangent unit vector with respect to the arc length, namely

$$\kappa = \frac{\mathrm{d}\theta}{\mathrm{d}s}, \tag{2.1}$$

where s is the arc length, and θ is the angle made by the tangent vector with the horizontal axis. This rate of change is a measure of the degree of bending of the curve, and so any straight line has zero curvature since the tangent angle θ does not change. Furthermore, the inverse of the curvature κ gives the radius of the curvature R, that is $R = 1/\kappa$. Throughout this work, the curvature is denoted by κ, which can be expressed using different

formulas depending on how the curve is parametrised. Next, we present some illustrative representations for κ that we use in this work.

Case 1. We begin with the most general case for a plane-curve where the curve C is parametrised by an arbitrary variable t. Then the position vector of any point on C may be written as

$$\mathbf{r}(t) = x(t)\,\mathbf{i} + y(t)\,\mathbf{j}, \quad t_\mathrm{a} \leq t \leq t_\mathrm{b},$$

where $x(t)$ and $y(t)$ are continuously differentiable functions on $[t_\mathrm{a}, t_\mathrm{b}]$. The arc length of the curve C is then calculated by

$$s(t) = \int_{t_\mathrm{a}}^{t_\mathrm{b}} \sqrt{(\mathrm{d}x/\mathrm{d}t)^2 + (\mathrm{d}y/\mathrm{d}t)^2}\,\mathrm{d}t\,.$$

Thus, we may utilise the fundamental theorem of calculus and write

$$\mathrm{d}s = \sqrt{\dot{x}^2 + \dot{y}^2}\,\mathrm{d}t\,, \tag{2.2}$$

where dots denote derivatives with respect to t. Similarly, at any point on the curve C, the tangent vector $\dot{\mathbf{r}}(t)$ makes the angle $\theta(t)$ with the horizontal axis. The tangent vector to the curve C at $\mathbf{r}(t)$ may also be written as

$$\dot{\mathbf{r}}(t) = \dot{x}(t)\,\mathbf{i} + \dot{y}(t)\,\mathbf{j},$$

and the equivalent expression in polar coordinates is written as

$$\dot{\mathbf{r}}(t) = \|\dot{\mathbf{r}}(t)\|\,(\cos\theta(t)\,\mathbf{i} + \sin\theta(t)\,\mathbf{j})\,.$$

From these expressions of the tangent vector $\dot{\mathbf{r}}(t)$, we obtain

$$\frac{\mathrm{d}y}{\mathrm{d}x} = \frac{\dot{y}(t)}{\dot{x}(t)} = \frac{\sin\theta(t)}{\cos\theta(t)} = \tan\theta(t).$$

Upon differentiating both sides with respect to t, we derive

$$\frac{\mathrm{d}}{\mathrm{d}t}\left(\frac{\dot{y}(t)}{\dot{x}(t)}\right) = \frac{\dot{x}\,\ddot{y} - \ddot{x}\,\dot{y}}{\dot{x}^2} = \sec^2\theta(t)\,\frac{\mathrm{d}\theta}{\mathrm{d}t}.$$

We now make the substitution

$$\sec^2\theta(t) = \tan^2\theta(t) + 1 = \left(\frac{\dot{y}}{\dot{x}}\right)^2 + 1 = \frac{\dot{x}^2 + \dot{y}^2}{\dot{x}^2},$$

to derive

$$\frac{\mathrm{d}\theta}{\mathrm{d}t} = \frac{\dot{x}\,\ddot{y} - \ddot{x}\,\dot{y}}{\dot{x}^2 + \dot{y}^2}. \tag{2.3}$$

We now substitute (2.2)–(2.3) into (2.1) to derive the curvature κ at any point $(x(t), y(t))$ as

$$\kappa(t) = \frac{\mathrm{d}\theta}{\mathrm{d}s} = \frac{\mathrm{d}\theta}{\mathrm{d}t}\frac{\mathrm{d}t}{\mathrm{d}s} = \left(\frac{\dot{x}\,\ddot{y} - \ddot{x}\,\dot{y}}{\dot{x}^2 + \dot{y}^2}\right)\left(\frac{1}{\sqrt{\dot{x}^2 + \dot{y}^2}}\right) = \frac{\dot{x}\,\ddot{y} - \ddot{x}\,\dot{y}}{(\dot{x}^2 + \dot{y}^2)^{3/2}}. \tag{2.4}$$

Case 2. If the curve C is parametrised by x, then the position vector of points on C may be written as

$$\mathbf{r}(x) = x\,\mathbf{i} + y(x)\,\mathbf{j}, \quad x_\mathrm{a} \le x \le x_\mathrm{b}.$$

The arc length of the curve C is then calculated by

$$s(x) = \int_{x_\mathrm{a}}^{x_\mathrm{b}} \sqrt{(1 + (\mathrm{d}y/\mathrm{d}x)^2}\,\mathrm{d}x\,.$$

Thus, by the fundamental theorem of calculus we may write

$$\mathrm{d}s = \sqrt{1 + y'^2}\,\mathrm{d}x\,,$$

where primes denote derivatives with respect to x. Following the same steps as in *Case 1*, the curvature κ at any point $(x, y(x))$ may defined as

$$\kappa(x) = \frac{y''}{(1 + y'^2)^{3/2}}.$$

Note that this formula is a direct consequence of substituting $t = x$ in the general formula (2.4) since $\dot{x} = 1$, and $\dot{y} = y'$.

Case 3. If the curve C is parametrised by arc length s, then the position vector of any point on C may be written as

$$\mathbf{r}(s) = x(s)\,\mathbf{i} + y(s)\,\mathbf{j}, \quad s_\mathrm{a} \le s \le s_\mathrm{b}.$$

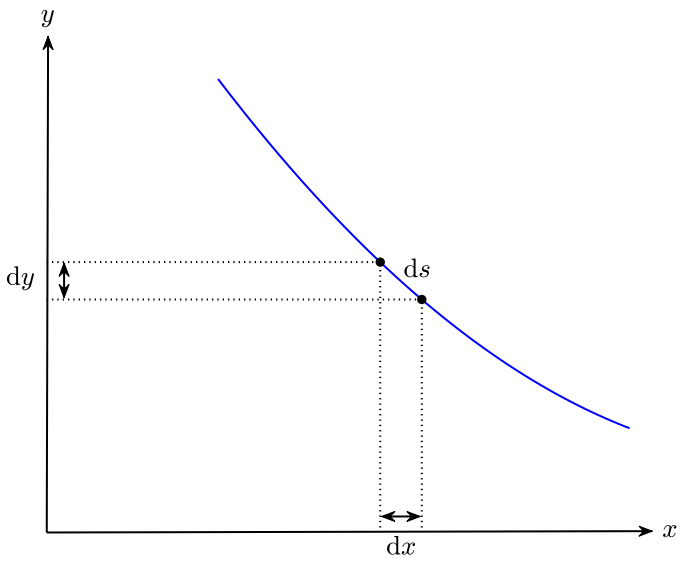

Figure 2.1: Representation of a curve parametrised by s.

In this case, the parameter s has the following property

$$\left(\frac{\mathrm{d}x}{\mathrm{d}s}\right)^2 + \left(\frac{\mathrm{d}y}{\mathrm{d}s}\right)^2 = 1,$$

which ensures that the parameter s measures the arc length along the curve. With reference to Fig. 2.1, we apply Pythagoras's theorem to obtain

$$\mathrm{d}s = \sqrt{(\mathrm{d}x)^2 + (\mathrm{d}y)^2}.$$

Following the same reasoning as in *Case 1*, the curvature κ at any point $(x(s), y(s))$ may defined as

$$\kappa(s) = \frac{\mathrm{d}x}{\mathrm{d}s}\frac{\mathrm{d}^2y}{\mathrm{d}s^2} - \frac{\mathrm{d}^2x}{\mathrm{d}s^2}\frac{\mathrm{d}y}{\mathrm{d}s}.$$

2.1.2 Variational calculus

Minimisation principles are commonly used in applied mathematics and theoretical physics. The calculus of variations is a technique that has been used

in formulating mathematical models across a large number of physical fields, particularly in the field of mechanics including solid–, fluid–, and quantum–mechanics. Variational calculus also can be utilised to formulate optimisation problems for geometrical configurations such as minimal surfaces, geodesics, and optics. In the terminology of variational calculus, the solution to such an optimisation problem is described by a boundary value problem that is governed by differential equation(s) known as the Euler–Lagrange equation(s).

In mathematics, functions map inputs (independent variables) to outputs (dependent variables). However, the functional J is a mapping from a set of functions U (forming a vector space) to the real numbers $\mathbb{R}$. Hence, a functional is a function where the independent variables include functions from an appropriate vector space. The norm vector space $(U, \|\cdot\|)$ comprises a set of functions U defined on fixed domain and range, with an associated *norm* $\|\cdot\|$, which assigns a non-negative number to every function in U. In the calculus of variations, the functional is generally defined with a definite integral that allows us to account for a set of functions and find a particular member from this set that maximises or minimises the functional.

Consider a functional $J : U \to \mathbb{R}$ defined on the norm vector space $(U, \|\cdot\|)$ and assume that $S \subseteq U$. Then the functional J is said to have a local maximum in S at $y \in S$ if there is an $\varepsilon > 0$ for which $J(\tilde{y}) - J(y) \leq 0$, for all $\tilde{y} \in S$ such that $\| \tilde{y} - y \| < \varepsilon$. If y is a local maximum in S for $-J$, then y is a local minimum in S for J. With reference to Fig. 2.2, the varied functions $\tilde{y} \in S$ are assumed to be in an $\varepsilon-$neighbourhood of the function $y \in S$, and therefore it can be written as $\tilde{y} = y + \varepsilon\eta$, where $\eta \in U$. Next, we consider some variational problems and give the necessary conditions for a functional J to have an extremum. The reader is referred to Brunt [62] for detailed derivations of these conditions.

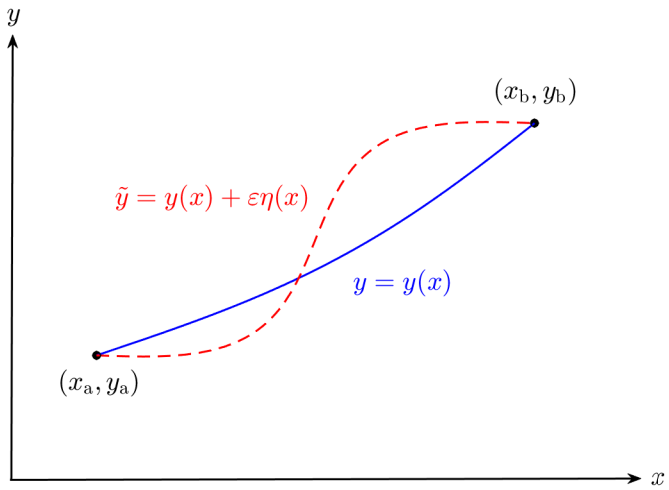

Figure 2.2: Representation of a variational problem with fixed boundary conditions.

The fundamental variational problem

In the simplest case, we consider the set $U = C^2[x_\mathrm{a}, x_\mathrm{b}]$, which contains functions with continuous second derivatives on the interval $[x_\mathrm{a}, x_\mathrm{b}]$. Now, consider a functional $J : U \to \mathbb{R}$ of the form

$$J[y] = \int_{x_\mathrm{a}}^{x_\mathrm{b}} F(x, y(x), y'(x))\,\mathrm{d}x\,, \tag{2.5}$$

with the integrand F, and suppose that J has an extremum for $y \in S$, where

$$S = \{y \in C^2[x_\mathrm{a}, x_\mathrm{b}] : y(x_\mathrm{a}) = y_\mathrm{a}, \text{ and } y(x_\mathrm{b}) = y_\mathrm{b}\}. \tag{2.6}$$

Then, there is an $\varepsilon > 0$ for which $J[\tilde{y}] - J[y] \leq 0$, for all $\tilde{y} \in S$ such that $\| \tilde{y} - y \| < \varepsilon$. Recall that the varied function $\tilde{y}$ can be written as $\tilde{y}(x) = y(x) + \varepsilon\eta(x)$, and since $\tilde{y} \in S$, the function η must vanish at the endpoints, namely $\eta \in \mathcal{H}$ such that

$$\mathcal{H} = \{\eta \in C^2[x_\mathrm{a}, x_\mathrm{b}] : \eta(x_\mathrm{a}) = \eta(x_\mathrm{b}) = 0\}. \tag{2.7}$$

Next, we define the first variation of J as

$$\delta J[y,\eta] = \lim_{\varepsilon\to 0}\frac{1}{\varepsilon}\Big(J[\tilde{y}] - J[y]\Big), \tag{2.8}$$

whereupon we apply Taylor's theorem to rewrite $F(x,\tilde{y},\tilde{y}')$ as

$$\begin{aligned} F(x,\tilde{y},\tilde{y}') &= F(x, y+\varepsilon\eta, y'+\varepsilon\eta') \\ &= F(x,y,y') + \varepsilon\,[F_y\,\eta + F_{y'}\,\eta'] + \mathcal{O}(\varepsilon^2), \end{aligned} \tag{2.9}$$

where subscripts denote partial derivatives. Hence, on substituting (2.9) into (2.8), we find that the first variation of J is

$$\delta J[y,\eta] = \int_{x_\mathrm{a}}^{x_\mathrm{b}} [F_y\,\eta + F_{y'}\,\eta']\,\mathrm{d}x\,. \tag{2.10}$$

The condition that $J[y]$ has an extremum in S requires that $\delta J[y,\eta] = 0$, or

$$\delta J[y,\eta] = \int_{x_\mathrm{a}}^{x_\mathrm{b}} [F_y\,\eta + F_{y'}\,\eta']\,\mathrm{d}x = 0.$$

We now perform integration by parts on the previous equation to eliminate the η' term, which yields

$$\delta J[y,\eta] = [F_{y'}\,\eta]_{x_\mathrm{a}}^{x_\mathrm{b}} + \int_{x_\mathrm{a}}^{x_\mathrm{b}} \left[F_y\,\eta - \frac{\mathrm{d}}{\mathrm{d}x}F_{y'}\,\eta\right]\mathrm{d}x = 0.$$

We note that since $\eta \in \mathcal{H}$, and from the definition of $\mathcal{H}$ (2.7), the function η must vanish at the end points. Thus, we may use the boundary conditions on η to derive

$$\delta J[y,\eta] = \int_{x_\mathrm{a}}^{x_\mathrm{b}} \eta\left[F_y - \frac{\mathrm{d}}{\mathrm{d}x}F_{y'}\right]\mathrm{d}x = 0. \tag{2.11}$$

Now, since η is an arbitrary function, it can be concluded that its coefficient in (2.11) must vanish over the interval $[x_\mathrm{a}, x_\mathrm{b}]$, and this leads to a second–order differential equation

$$\frac{\mathrm{d}}{\mathrm{d}x}F_{y'} - F_y = 0,$$

known as the Euler–Lagrange equation, which is a necessary condition for $J[y]$ to have an extremum for a given function $y(x)$.

Variational problems with higher derivatives

We note that many problems in solid mechanics are described by functionals whose integrands depend on higher–order derivatives. Thus, the vector space U must be restricted to account for the higher–order derivatives. For the problems considered in this work, we only need to deal with functionals whose integrands depend on second–order derivatives. Thus, we extend the previous example by considering the vector space $U = C^4[x_\mathrm{a}, x_\mathrm{b}]$, the set of functions with continuous fourth derivatives. We assume that the functional $J : U \to \mathbb{R}$ of the form

$$J[y] = \int_{x_\mathrm{a}}^{x_\mathrm{b}} F(x, y(x), y'(x), y''(x))\,\mathrm{d}x\,, \tag{2.12}$$

has an extremum in S at $y \in S$, where in this case

$$S = \{y \in C^4[x_\mathrm{a}, x_\mathrm{b}] : y(x_\mathrm{a}) = y_\mathrm{a},\ y'(x_\mathrm{a}) = y'_\mathrm{a},\ y(x_\mathrm{b}) = y_\mathrm{b},\ \text{and}\ y'(x_\mathrm{b}) = y'_\mathrm{b}\}.$$

Following the same reasoning as in the previous section, we derive a necessary condition for $J[y]$ to have an extremum for a given function $y(x)$. In this case, the varied functions $\tilde{y}$ are a family of continuously twice–differentiable functions, and written as

$$\tilde{y}(x) = y(x) + \varepsilon\eta(x),$$

which, in order to satisfy that $\tilde{y} \in S$, we must have $\eta \in \mathcal{H}$ such that

$$\mathcal{H} = \{\eta \in C^4[x_\mathrm{a}, x_\mathrm{b}] : \eta(x_\mathrm{a}) = \eta(x_\mathrm{b}) = \eta'(x_\mathrm{a}) = \eta'(x_\mathrm{b}) = 0\}. \tag{2.13}$$

Considering the definition of $\delta J[y, \eta]$ given by (2.8), we now apply Taylor's theorem to rewrite $F(x, \tilde{y}, \tilde{y}', \tilde{y}'')$ as

$$\begin{aligned} F(x, \tilde{y}, \tilde{y}', \tilde{y}'') &= F(x, y + \varepsilon\eta, y' + \varepsilon\eta', y'' + \varepsilon\eta'') \\ &= F(x, y, y', y'') + \varepsilon\left[F_y\,\eta + F_{y'}\,\eta' + F_{y''}\,\eta''\right] + \mathcal{O}(\varepsilon^2). \end{aligned}$$

Therefore, the first variation for the functional J is then derived as

$$\delta J[y,\eta] = \int_{x_\mathrm{a}}^{x_\mathrm{b}} \left[F_y\,\eta + F_{y'}\,\eta' + F_{y''}\,\eta''\right] \mathrm{d}x\,,$$

and the condition that $J[y]$ has an extremum in S requires that $\delta J[y,\eta] = 0$. In this case the integrand of $\delta J[y,\eta]$ does not only involve the η' term, but also involves the η'' term. Thus we must integrate by parts twice to eliminate these terms, and doing so gives

$$\begin{aligned}\delta J[y,\eta] = &\left[\eta'\,F_{y''} - \eta\left(\frac{\mathrm{d}}{\mathrm{d}x}F_{y''} - F_{y'}\right)\right]_{x_\mathrm{a}}^{x_\mathrm{b}} \\ &+ \int_{x_\mathrm{a}}^{x_\mathrm{b}} \eta\left[F_y - \frac{\mathrm{d}}{\mathrm{d}x}F_{y'} + \frac{\mathrm{d}^2}{\mathrm{d}x^2}F_{y''}\right]\mathrm{d}x = 0,\end{aligned}$$

which after using the boundary conditions from the definition of $\mathcal{H}$ (2.13) becomes

$$\delta J[y,\eta] = \int_{x_\mathrm{a}}^{x_\mathrm{b}} \eta\left[F_y - \frac{\mathrm{d}}{\mathrm{d}x}F_{y'} + \frac{\mathrm{d}^2}{\mathrm{d}x^2}F_{y''}\right]\mathrm{d}x = 0. \tag{2.14}$$

Hence, we conclude that coefficient of $\eta(x)$ in (2.14) must vanish over the interval $[x_\mathrm{a}, x_\mathrm{b}]$, leading to the condition

$$F_y - \frac{\mathrm{d}}{\mathrm{d}x}F_{y'} + \frac{\mathrm{d}^2}{\mathrm{d}x^2}F_{y''} = 0, \tag{2.15}$$

which is known as the Euler–Poisson equation, a necessary condition for $J[y]$ to have an extremum for a given function $y(x)$.

We now consider some special cases for the integrand F and obtain the corresponding simplified Euler–Poisson equations which are generally called first integrals.

Case 1. If the integrand F does not explicitly depend on y, then we have a functional of the form

$$J[y] = \int_{x_\mathrm{a}}^{x_\mathrm{b}} F(x, y', y'')\,\mathrm{d}x\,.$$

With reference to the Euler–Poisson equation (2.15), we note that for this case $F_y = 0$. Therefore, upon integrating (2.15) with respect to x, we obtain the first integral

$$F_{y'} - \frac{\mathrm{d}}{\mathrm{d}x} F_{y''} = P, \tag{2.16}$$

where P is a constant.

Case 2. If the integrand F does not explicitly depend on x, then we have a functional of the form

$$J[y] = \int_{x_\mathrm{a}}^{x_\mathrm{b}} F(y, y', y'')\,\mathrm{d}x\,.$$

We note that the definition of the total derivative for an integrand of the form $F(x, y, y', y'')$ is given by

$$\frac{\mathrm{d}}{\mathrm{d}x} F = F_x + y'\,F_y + y''\,F_{y'} + y'''\,F_{y''}. \tag{2.17}$$

When the integrand F has no explicit dependence on x, namely $F(y, y', y'')$, then $F_x = 0$. Thus, equation (2.17) may be rearranged to give

$$y'\,F_y = \frac{\mathrm{d}}{\mathrm{d}x} F - y''\,F_{y'} - y'''\,F_{y''}. \tag{2.18}$$

Furthermore, an equivalent expression for the term $y'\,F_y$ may be written by multiplying the Euler–Poisson equation (2.15) by y' and then solving for $y'\,F_y$ to obtain

$$y'\,F_y = y'\frac{\mathrm{d}}{\mathrm{d}x} F_{y'} - y'\frac{\mathrm{d}^2}{\mathrm{d}x^2} F_{y''}. \tag{2.19}$$

Equating (2.18) and (2.19) yields

$$y'\frac{\mathrm{d}}{\mathrm{d}x} F_{y'} - y'\frac{\mathrm{d}^2}{\mathrm{d}x^2} F_{y''} - \frac{\mathrm{d}}{\mathrm{d}x} F + y''\,F_{y'} + y'''\,F_{y''} = 0. \tag{2.20}$$

We now give some expressions which are used to simplify the previous equation. These expressions are

$$\frac{\mathrm{d}}{\mathrm{d}x}\left(y'\,F_{y'}\right) = y'\frac{\mathrm{d}}{\mathrm{d}x} F_{y'} + y''\,F_{y'},$$
$$\frac{\mathrm{d}}{\mathrm{d}x}\left(y''\,F_{y''}\right) = y''\frac{\mathrm{d}}{\mathrm{d}x} F_{y''} + y'''\,F_{y''}.$$

Using these expressions, equation (2.20) may be rearranged to derive

$$\frac{\mathrm{d}}{\mathrm{d}x}\left(y'\,F_{y'}\right) - y'\frac{\mathrm{d}^2}{\mathrm{d}x^2}F_{y''} + \frac{\mathrm{d}}{\mathrm{d}x}\left(y''\,F_{y''}\right) - y''\frac{\mathrm{d}}{\mathrm{d}x}F_{y''} - \frac{\mathrm{d}}{\mathrm{d}x}F = 0. \tag{2.21}$$

Note that by the preduct rule

$$\frac{\mathrm{d}}{\mathrm{d}x}\left(y'\,\frac{\mathrm{d}}{\mathrm{d}x}F_{y''}\right) = y'\frac{\mathrm{d}^2}{\mathrm{d}x^2}F_{y''} + y''\frac{\mathrm{d}}{\mathrm{d}x}F_{y''},$$

so that equation (2.21) becomes

$$\frac{\mathrm{d}}{\mathrm{d}x}\left(y'\,F_{y'}\right) - \frac{\mathrm{d}}{\mathrm{d}x}\left(y'\,\frac{\mathrm{d}}{\mathrm{d}x}F_{y''}\right) + \frac{\mathrm{d}}{\mathrm{d}x}\left(y''\,F_{y''}\right) - \frac{\mathrm{d}}{\mathrm{d}x}F = 0,$$

or equivalently,

$$\frac{\mathrm{d}}{\mathrm{d}x}\left[y'\left(F_{y'} - \frac{\mathrm{d}}{\mathrm{d}x}F_{y''}\right) + y''\,F_{y''} - F\right] = 0.$$

Integrating the above equation with respect to x leads to another first integral of the Euler–Poisson equation

$$y'\left(F_{y'} - \frac{\mathrm{d}}{\mathrm{d}x}F_{y''}\right) + y''\,F_{y''} - F = H, \tag{2.22}$$

where H is a constant.

Variational problems with free boundary conditions

Up to this point, we have assumed that the extremal $y(x)$ satisfies the boundary conditions $y(x_\mathrm{a}) = y_\mathrm{a}$, and $y(x_\mathrm{b}) = y_\mathrm{b}$. However, a variational problem may be complicated when the value of $y(x)$ is not prescribed at one or both endpoints as illustrated in Fig. 2.3. In these cases, the difference between $y(x)$ and the varied $\tilde{y}(x) = y(x) + \varepsilon\eta(x)$, as well as their derivatives need not vanish at the endpoint where the condition is missing. Consequently, we are unable to use the assumptions from the definition of $\mathcal{H}$, given by (2.13), to derive an unconstrained Euler–Poisson equation. A more careful derivation

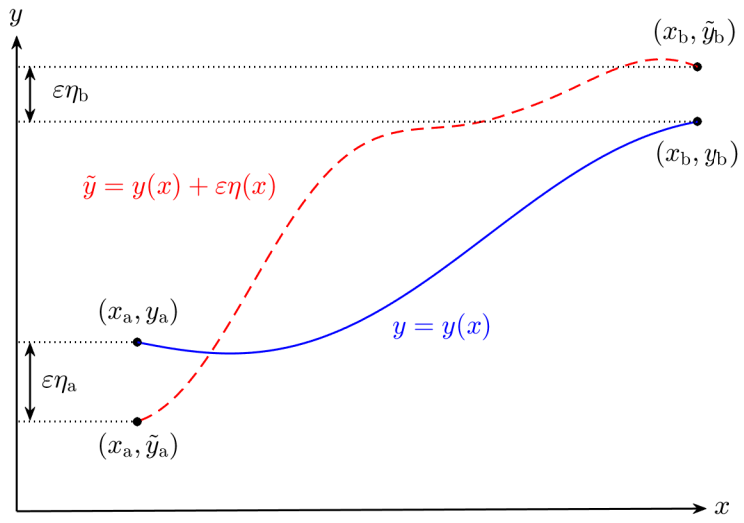

Figure 2.3: Representation of a variational problem with natural boundary conditions on y.

is required to determine the missing conditions, which are termed *natural boundary* conditions.

We consider the functional J of the form (2.12), and assume that J has an extremum in $U = C^4[x_\mathrm{a}, x_\mathrm{b}]$ at y. In this problem, no boundary conditions are imposed on the extremal y. Similarly, the varied functions $\tilde{y} \in U$ are then written as

$$\tilde{y}(x) = y(x) + \varepsilon\eta(x),$$

and accordingly, η is not required to vanish at the endpoints, that is $\eta \in U$. We now follow the same steps as in the previous problem and proceed to

$$\begin{aligned}\delta J[y,\eta] = &\left[\eta' F_{y''} - \eta\left(\frac{\mathrm{d}}{\mathrm{d}x}F_{y''} - F_{y'}\right)\right]_{x_\mathrm{a}}^{x_\mathrm{b}} \\ &+ \int_{x_\mathrm{a}}^{x_\mathrm{b}} \eta\left[F_y - \frac{\mathrm{d}}{\mathrm{d}x}F_{y'} + \frac{\mathrm{d}^2}{\mathrm{d}x^2}F_{y''}\right]\mathrm{d}x = 0.\end{aligned}$$

This equation must be satisfied for all $\eta \in U$, including the functions η that

also satisfy the conditions (2.13). Therefore, the previous problem may be considered as a degenerate case which has led to a condition given by

$$F_y - \frac{\mathrm{d}}{\mathrm{d}x}F_{y'} + \frac{\mathrm{d}^2}{\mathrm{d}x^2}F_{y''} = 0.$$

However, since we account for all of $\eta \in U$, this condition is augmented by

$$\left[\eta'\, F_{y''} - \eta\left(\frac{\mathrm{d}}{\mathrm{d}x}F_{y''} - F_{y'}\right)\right]_{x_\mathrm{a}}^{x_\mathrm{b}} = 0,$$

which, if assuming all endpoints are independent, leads to the following four conditions

$$F_{y''}\big|_{x_\mathrm{a}} = 0, \quad F_{y''}\big|_{x_\mathrm{b}} = 0, \quad \left(\frac{\mathrm{d}}{\mathrm{d}x}F_{y''} - F_{y'}\right)\bigg|_{x_\mathrm{a}} = 0, \quad \left(\frac{\mathrm{d}}{\mathrm{d}x}F_{y''} - F_{y'}\right)\bigg|_{x_\mathrm{b}} = 0,$$

which are known as the natural boundary conditions. We comment that if the boundary conditions are prescribed at one endpoint, then the natural boundary conditions at that endpoint are not needed. For example, if the extremal $y(x) \in S$ where

$$S = \{y \in C^4[x_\mathrm{a}, x_\mathrm{b}] : y(x_\mathrm{a}) = y_\mathrm{a}, \quad \text{and} \quad y'(x_\mathrm{a}) = y'_\mathrm{a}\},$$

then the natural boundary conditions at x_a are not needed, but those at x_b are still used.

Variational problems with variable endpoints

In the previous section, we considered variational problems where the boundary conditions for the y–coordinates are not prescribed. We now consider more general variational problems where both the endpoints of the x– and y–coordinates are determined as part of the solution. Representative plots for a variational problem with free endpoints are shown in Fig. 2.4.

We consider the functional $J : U \to \mathbb{R}$ of the form

$$J[y] = \int_{x_\mathrm{a}}^{x_\mathrm{b}} F(x, y(x), y'(x), y''(x))\,\mathrm{d}x\,,$$

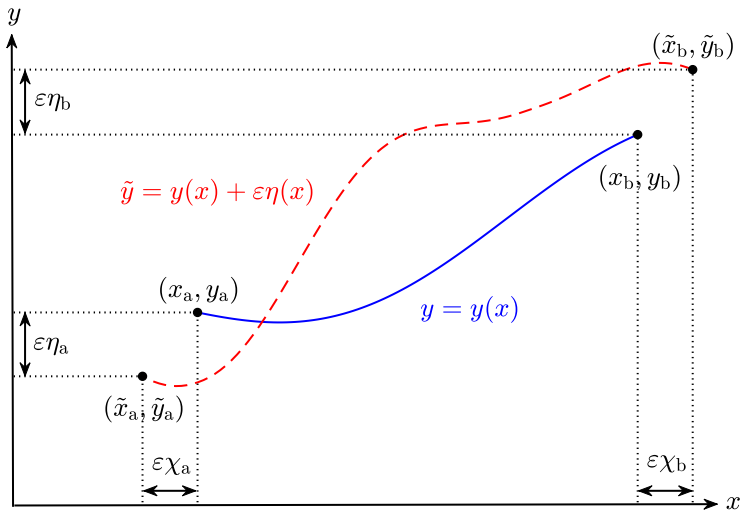

Figure 2.4: Representation of a variational problem with natural boundary conditions on both x and y.

and assume that J has an extremum in $U = C^4[x_\mathrm{a}, x_\mathrm{b}]$ at y. For both the independent and the dependent variables, we introduce the varied functions $\tilde{x}$ and $\tilde{y}$ such that

$$\tilde{x} = x + \varepsilon\chi, \quad \text{and} \quad \tilde{y} = y + \varepsilon\eta.$$

Recall that the definition of the first variation of J is given by

$$\delta J[y, \eta] = \lim_{\varepsilon \to 0} \frac{1}{\varepsilon} \Big(J[\tilde{y}] - J[y] \Big). \tag{2.23}$$

In this problem, the integration limit for the functional $J[\tilde{y}]$ may be variable, that is

$$J[\tilde{y}] = \int_{\tilde{x}_\mathrm{a}}^{\tilde{x}_\mathrm{b}} F(x, \tilde{y}, \tilde{y}', \tilde{y}'')\,\mathrm{d}x = \int_{x_\mathrm{a}+\varepsilon\chi_\mathrm{a}}^{x_\mathrm{b}+\varepsilon\chi_\mathrm{b}} F(x, \tilde{y}, \tilde{y}', \tilde{y}'')\,\mathrm{d}x\,.$$

Then we consider the term $J[\tilde{y}] - J[y]$, which can be written as

$$J[\tilde{y}] - J[y] = \int_{x_\mathrm{a}+\varepsilon\chi_\mathrm{a}}^{x_\mathrm{b}+\varepsilon\chi_\mathrm{b}} F(x, \tilde{y}, \tilde{y}', \tilde{y}'')\,\mathrm{d}x - \int_{x_\mathrm{a}}^{x_\mathrm{b}} F(x, y, y', y'')\,\mathrm{d}x\,,$$

or, equivalently, can be split into three integrals as

$$J[\tilde{y}] - J[y] = I_1 + I_2 - I_3,$$

with

$$\begin{aligned} I_1 &= \int_{x_\mathrm{a}}^{x_\mathrm{b}} (F(x,\tilde{y},\tilde{y}',\tilde{y}'') - F(x,y,y',y''))\,\mathrm{d}x\,, \\ I_2 &= \int_{x_\mathrm{b}}^{x_\mathrm{b}+\varepsilon\chi_\mathrm{b}} F(x,\tilde{y},\tilde{y}',\tilde{y}'')\,\mathrm{d}x\,, \\ I_3 &= \int_{x_\mathrm{a}}^{x_\mathrm{a}+\varepsilon\chi_\mathrm{b}} F(x,\tilde{y},\tilde{y}',\tilde{y}'')\,\mathrm{d}x\,. \end{aligned}$$

Taylor's theorem is applied on the first integral as before to deduce that

$$I_1 = \varepsilon\left\{\left[\eta' F_{y''} - \eta\left(\frac{\mathrm{d}}{\mathrm{d}x}F_{y''} - F_{y'}\right)\right]_{x_\mathrm{a}}^{x_\mathrm{b}} + \int_{x_\mathrm{a}}^{x_\mathrm{b}} \eta\left[F_y - \frac{\mathrm{d}}{\mathrm{d}x}F_{y'} + \frac{\mathrm{d}^2}{\mathrm{d}x^2}F_{y''}\right]\mathrm{d}x\right\},$$

and since ε is small, the second and third integrals are then respectively reduced to

$$I_2 = \varepsilon\chi_\mathrm{b} F(x,y,y',y'')\big|_{x_\mathrm{b}}, \quad \text{and} \quad I_3 = \varepsilon\chi_\mathrm{a} F(x,y,y',y'')\big|_{x_\mathrm{a}}.$$

Hence, on substitution of these quantities into (2.23), the first variation of J may be written as

$$\begin{aligned} \delta J[y,\eta] = &\left[\eta' F_{y''} - \eta\left(\frac{\mathrm{d}}{\mathrm{d}x}F_{y''} - F_{y'}\right)\right]_{x_\mathrm{a}}^{x_\mathrm{b}} + \int_{x_\mathrm{a}}^{x_\mathrm{b}} \eta\left[F_y - \frac{\mathrm{d}}{\mathrm{d}x}F_{y'} + \frac{\mathrm{d}^2}{\mathrm{d}x^2}F_{y''}\right]\mathrm{d}x \\ &+ \chi_\mathrm{b} F(x,y,y',y'')\big|_{x_\mathrm{b}} - \chi_\mathrm{a} F(x,y,y',y'')\big|_{x_\mathrm{a}}. \end{aligned} \tag{2.24}$$

Furthermore, the variation at the endpoint $(x_\mathrm{a}, y_\mathrm{a})$ must satisfy the compatibility condition, that is

$$\tilde{y}_\mathrm{a} = y(\tilde{x}_\mathrm{a}) = y(x_\mathrm{a} + \varepsilon\chi_\mathrm{a}) + \varepsilon\eta(x_\mathrm{a} + \varepsilon\chi_\mathrm{a}) = y_\mathrm{a} + \varepsilon\eta_\mathrm{a},$$

and Taylor's theorem may also be applied to obtain

$$y(\tilde{x}_a) = y(x_\mathrm{a} + \varepsilon\chi_\mathrm{a}) + \varepsilon\eta(x_\mathrm{a} + \varepsilon\chi_\mathrm{a}) = y(x_\mathrm{a}) + \varepsilon\chi_\mathrm{a}\, y'(x_\mathrm{a}) + \varepsilon\eta(x_\mathrm{a}).$$

The two previous expressions may be equated to write $\eta(x_\mathrm{a})$ as

$$\eta(x_\mathrm{a}) = \eta_\mathrm{a} - \chi_\mathrm{a}\, y'(x_\mathrm{a}).$$

Similar steps are then taken to obtain

$$\begin{aligned}
\eta(x_\mathrm{b}) &= \eta_\mathrm{b} - \chi_\mathrm{b}\, y'(x_\mathrm{b}),\\
\eta'(x_\mathrm{a}) &= \eta'_\mathrm{a} - \chi_\mathrm{a}\, y''(x_\mathrm{a}),\\
\eta'(x_\mathrm{b}) &= \eta'_\mathrm{b} - \chi_\mathrm{b}\, y''(x_\mathrm{b}).
\end{aligned}$$

We now use these expressions for the endpoints of η and η' in (2.24) to derive

$$\begin{aligned}
\delta J = &\left\{\left[F_{y'} - \frac{\mathrm{d}}{\mathrm{d}x}F_{y''}\right]\delta y + F_{y''}\delta y' + \left[F - y'\left(F_{y'} - \frac{\mathrm{d}}{\mathrm{d}x}F_{y''}\right) + y''F_{y''}\right]\delta x\right\}_{x_\mathrm{a}}^{x_\mathrm{b}}\\
&+ \int_{x_\mathrm{a}}^{x_\mathrm{b}}\left[F_y - \frac{d}{dx}\,F_{y'} + \frac{d^2}{dx^2}\,F_{y''}\right]\delta y\,\mathrm{d}x\,,
\end{aligned}$$

where

$$\delta x(x_\mathrm{i}) = \chi_\mathrm{i}, \quad \delta y(x_\mathrm{i}) = \eta_\mathrm{i}, \quad \delta y'(x_\mathrm{i}) = \eta'_\mathrm{i}.$$

while i represents a or b. Considering the Hamiltonian formulation of mechanics, an even more concise formula may be written for the variation of J. First, the canonical coordinate transformations are made such that

$$P = F_{y'} - \frac{\mathrm{d}}{\mathrm{d}x}\,F_{y''}, \quad Q = F_{y''}, \tag{2.25}$$

where P and Q denote the coordinates in the phase space. Then the Hamiltonian function corresponding to the functional J is written in terms of P and Q as

$$H(P,Q) = P\,y' + Q\,y'' - F. \tag{2.26}$$

Finally, the definitions of P, Q, and H are used to write the simplified expression of δJ as

$$\delta J = \left[P\,\delta y + Q\,\delta y' - H\,\delta x\right]_{x_\mathrm{a}}^{x_\mathrm{b}} + \int_{x_\mathrm{a}}^{x_\mathrm{b}}\left[F_y - \frac{d}{dx}F_{y'} + \frac{d^2}{dx^2}F_{y''}\right]\delta y\,\mathrm{d}x\,, \tag{2.27}$$

where the second order Euler–Poisson equation with variable boundary is given by

$$F_y - \frac{d}{dx} F_{y'} + \frac{d^2}{dx^2} F_{y''} = 0,$$

and the natural boundary condition

$$[P\,\delta y + Q\,\delta y' - H\,\delta x]_{x_\mathrm{a}}^{x_\mathrm{b}} = 0.$$

We recall from our discussion on first integrals that when the integrand F has no explicit dependence on y, then P is a conserved quantity as shown by (2.16). Similarly, H is a conserved quantity if the integrand F does not depend on x, as shown by (2.22).

Variational problems with two dependent variables

To this point, we have considered only a functional of the form

$$J[y] = \int_{x_\mathrm{a}}^{x_\mathrm{b}} F(x, y(x), y'(x), y''(x))\,\mathrm{d}x\,.$$

where the integrand F depends on a single dependent variable, $y(x)$ and its derivatives. The work is now extended to account for variational problems that depend on one independent variable and two dependent variables. We consider a functional J of the form

$$J[x, y] = \int_{t_\mathrm{a}}^{t_\mathrm{b}} F(t, x(t), y(t), \dot{x}(t), \dot{y}(t), \ddot{x}(t), \ddot{y}(t))\,\mathrm{d}t\,, \tag{2.28}$$

whose extremal is given in a parametric form $(x(t), y(t))$ that depends on the independent variable t and satisfies the prescribed boundary conditions

$$\begin{aligned} &x(t_\mathrm{a}) = x_\mathrm{a}, \quad \dot{x}(t_\mathrm{a}) = \dot{x}_\mathrm{a}, \quad y(t_\mathrm{a}) = y_\mathrm{a}, \quad \dot{y}(t_\mathrm{a}) = \dot{y}_\mathrm{a}, \\ &x(t_\mathrm{b}) = x_\mathrm{b}, \quad \dot{x}(t_\mathrm{b}) = \dot{x}_\mathrm{b}, \quad y(t_\mathrm{b}) = y_\mathrm{b}, \quad \dot{y}(t_\mathrm{b}) = \dot{y}_\mathrm{b}. \end{aligned}$$

We now introduce a pair of varied functions each corresponding to one dependent variable, namely

$$\tilde{x}(t) = x(t) + \varepsilon\chi(t), \quad \tilde{y}(t) = y(t) + \varepsilon\eta(t),$$

where χ and η are arbitrary functions that vanish at the endpoints, that is

$$\chi(t_\mathrm{a}) = \eta(t_\mathrm{a}) = \dot{\chi}(t_\mathrm{a}) = \dot{\eta}(t_\mathrm{a}) = \chi(t_\mathrm{b}) = \eta(t_\mathrm{b}) = \dot{\chi}(t_\mathrm{b}) = \dot{\eta}(t_\mathrm{b}) = 0. \quad (2.29)$$

The definition of the first variation of the functional J with two dependent variables is then given by

$$\begin{aligned}\delta J[x, y, \chi, \eta] &= \lim_{\varepsilon\to 0} \frac{1}{\varepsilon}\Big(J[\tilde{x}, \tilde{y}] - J[x, y]\Big) \\ &= \lim_{\varepsilon\to 0} \frac{1}{\varepsilon}\left[\int_{t_\mathrm{a}}^{t_\mathrm{b}} \big(F(t, \tilde{x}, \tilde{y}, \dot{\tilde{x}}, \dot{\tilde{y}}, \ddot{\tilde{x}}, \ddot{\tilde{y}}) - F(t, x, y, \dot{x}, \dot{y}, \ddot{x}, \ddot{y})\big)\,\mathrm{d}t\right].\end{aligned}$$

Taylor's theorem is now employed as before to obtain

$$\begin{aligned}F(t, \tilde{x}, \tilde{y}, \dot{\tilde{x}}, \dot{\tilde{y}}, \ddot{\tilde{x}}, \ddot{\tilde{y}}) &= F(t, x, y, \dot{x}, \dot{y}, \ddot{x}, \ddot{y}) \\ &\quad + \varepsilon\Big[\chi F_x + \dot{\chi}F_{\dot{x}} + \ddot{\chi}F_{\ddot{x}} + \eta F_y + \dot{\eta}F_{\dot{y}} + \ddot{\eta}F_{\ddot{y}}\Big] + \mathcal{O}(\varepsilon^2).\end{aligned}$$

Thus, the first variation for the functional J is derived as

$$\delta J[x, y, \chi, \eta] = \int_{t_\mathrm{a}}^{t_\mathrm{b}} \Big[\chi F_x + \dot{\chi}F_{\dot{x}} + \ddot{\chi}F_{\ddot{x}} + \eta F_y + \dot{\eta}F_{\dot{y}} + \ddot{\eta}F_{\ddot{y}}\Big]\,\mathrm{d}t\,,$$

and a necessary condition for J to have an extremum at $(x(t), y(t))$ requires that $\delta J[x, y, \chi, \eta] = 0$, for each dependent variable. For the first dependent variable x, the condition is reduced to

$$\int_{t_\mathrm{a}}^{t_\mathrm{b}} \Big[\chi F_x + \dot{\chi}F_{\dot{x}} + \ddot{\chi}F_{\ddot{x}}\Big]\,\mathrm{d}t = 0,$$

and we integrate by parts twice as before while applying the boundary conditions (2.29) to derive

$$F_x - \frac{\mathrm{d}}{\mathrm{d}t}F_{\dot{x}} + \frac{\mathrm{d}^2}{\mathrm{d}t^2}F_{\ddot{x}} = 0.$$

Similar derivations are also used for the second dependent variable y, which yield

$$F_y - \frac{\mathrm{d}}{\mathrm{d}t}F_{\dot{y}} + \frac{\mathrm{d}^2}{\mathrm{d}t^2}F_{\ddot{y}} = 0.$$

Therefore, we may conclude that the Euler–Poisson equation of a functional J with two dependent variables x and y is given by the pair of equations

$$F_x - \frac{\mathrm{d}}{\mathrm{d}t}F_{\dot{x}} + \frac{\mathrm{d}^2}{\mathrm{d}t^2}F_{\ddot{x}} = 0, \quad \text{and} \quad F_y - \frac{\mathrm{d}}{\mathrm{d}t}F_{\dot{y}} + \frac{\mathrm{d}^2}{\mathrm{d}t^2}F_{\ddot{y}} = 0. \tag{2.30}$$

It is worth noting that the generalisation of the theory to the case of n dependent variables extends the Euler–Poisson equation to a series of differential equations each corresponding to a single dependent variable.

Also, we consider the case when the functional (2.28) involves natural boundary conditions or variable endpoints. It has been shown that the Euler–Poisson equation is given a pair of equations due to the presence of two dependent variables x and y. Similarly, the canonical coordinates given by (2.25) are now redefined as

$$P_x = F_{\dot{x}} - \frac{\mathrm{d}}{\mathrm{d}t}\,F_{\ddot{x}}, \quad Q_x = F_{\ddot{x}}, \tag{2.31}$$

$$P_y = F_{\dot{y}} - \frac{\mathrm{d}}{\mathrm{d}t}\,F_{\ddot{y}}, \quad Q_y = F_{\ddot{y}}, \tag{2.32}$$

and the corresponding Hamiltonian function is then given by

$$H(P_{x,y}, Q_{x,y}) = P_x\,\dot{x} + P_y\,\dot{y} + Q_x\,\ddot{x} + Q_y\,\ddot{y} - F. \tag{2.33}$$

Then we may write the equivalent standard equation for the variation of J as

$$\begin{aligned}\delta J = {} & \left[P_x\,\delta x + P_y\,\delta y + Q_x\,\delta\dot{x} + Q_y\,\delta\dot{y} - H\,\delta t\right]_{t_\mathrm{a}}^{t_\mathrm{b}} \\ & + \int_{t_\mathrm{a}}^{t_\mathrm{b}} \left[\left(F_x - \frac{\mathrm{d}}{\mathrm{d}t}F_{\dot{x}} + \frac{\mathrm{d}^2}{\mathrm{d}t^2}F_{\ddot{x}}\right)\,\delta x + \left(F_y - \frac{\mathrm{d}}{\mathrm{d}t}F_{\dot{y}} + \frac{\mathrm{d}^2}{\mathrm{d}t^2}F_{\ddot{y}}\right)\,\delta y\right]\mathrm{d}t\,,\end{aligned} \tag{2.34}$$

where the second order Euler–Poisson equation with variable boundary is given by

$$F_x - \frac{\mathrm{d}}{\mathrm{d}t}F_{\dot{x}} + \frac{\mathrm{d}^2}{\mathrm{d}t^2}F_{\ddot{x}} = 0, \quad \text{and} \quad F_y - \frac{\mathrm{d}}{\mathrm{d}t}F_{\dot{y}} + \frac{\mathrm{d}^2}{\mathrm{d}t^2}F_{\ddot{y}} = 0.$$

with the natural boundary condition

$$[P_x\,\delta x + P_y\,\delta y + Q_x\,\delta\dot{x} + Q_y\,\delta\dot{y} - H\,\delta t]_{t_\mathrm{a}}^{t_\mathrm{b}} = 0.$$

It follows that if the integrand F has no explicit dependence on t, x, or y, then the corresponding quantity H, P_x, or P_y is a constant conserved quantity and a first integral of the Euler–Poisson equation.

2.1.3 Elliptic integrals

Elliptic integrals and functions have several direct applications in mathematical physics. Many physical and geometrical problems are described by nonlinear differential equations such as those given by (2.15)–(2.30), whose solutions may be expressed by elliptic integrals. In particular, determining the equilibrium configurations of some elastic problems can be solved explicitly in terms of elliptic integrals. The use of elliptic integrals to tackle problems in elasticity goes back at least as far as Stern [63]. Considering the main focus of this work is determining graphene configurations based on the elasticity of graphene and other factors, a brief overview of the characteristics of elliptic integrals is now presented.

Consider an integral of the form

$$\int \mathcal{R}\left(t, \sqrt{T(t)}\right) \mathrm{d}t\,, \tag{2.35}$$

where $\mathcal{R}$ is a rational function, and T is a polynomial. If T is a linear or a quadratic polynomial, then the integral (2.35) may be evaluated using standard integration techniques which yield explicit solutions in terms

of trigonometric, exponential or logarithmic functions. If T is a polynomial of higher degree, then evaluating the integral (2.35) is mathematically intractable. However, when T is a polynomial of the third or fourth degree, the integral (2.35) may be rewritten in terms of one of the following three fundamental integrals

$$
\begin{aligned}
F(\tau,k) &= \int_0^{\tau} \left[\left(1-t^2\right)\left(1-k^2t^2\right)\right]^{-1/2} \mathrm{d}t\,, \\
E(\tau,k) &= \int_0^{\tau} \left[\left(1-k^2t^2\right)/\left(1-t^2\right)\right]^{1/2} \mathrm{d}t\,, \\
\Pi(\tau,m,k) &= \int_0^{\tau} \left(1+m\,t^2\right)^{-1} \left[\left(1-t^2\right)\left(1-k^2t\right)\right]^{-1/2} \mathrm{d}t\,,
\end{aligned}
$$

which are referred to as incomplete elliptic integrals of the first, second, and third kind, respectively. The parameter τ is called the amplitude, which ranges between 0 and 1. The parameter k is called the elliptic modulus, which generally takes values $0 \leq k \leq 1$ in many physical problems. The parameter m, appearing in $\Pi(\tau,m,k)$, is called the characteristic, which is a real number that takes values $-\infty < m < \infty$. These elliptic integrals are written above in *Jacobi's notation*, but they can be converted to *Legendre's notation* using the substitution $t = \sin\theta$, which yields

$$
F(\phi,k) = \int_0^{\phi} \left(1-k^2\sin^2\theta\right)^{-1/2} \mathrm{d}\theta\,, \tag{2.36}
$$

$$
E(\phi,k) = \int_0^{\phi} \left(1-k^2\sin^2\theta\right)^{1/2} \mathrm{d}\theta\,, \tag{2.37}
$$

$$
\Pi(\phi,m,k) = \int_0^{\phi} \left(1+m\,\sin^2\theta\right)^{-1} \left(1-k^2\sin^2\theta\right)^{-1/2} \mathrm{d}\theta\,,
$$

where the amplitude in this notation is $\phi \in (0,\pi/2)$. *Legendre's notation* of the elliptic integrals of the first kind $F(\phi,k)$, and the second kind $E(\phi,k)$, is extensively used in this work, and thus it is important to mention some special cases where the amplitude ϕ lies beyond the above-mentioned range.

Case 1. If $\phi = 0$, then trivially we have

$$F(0,k) = 0, \quad E(0,k) = 0.$$

Case 2. If $\phi = \pi/2$, these integrals are then called complete elliptic integrals of the first and second kind, and are denoted by

$$K(k) = F(\pi/2,k) = \int_0^{\pi/2} \left(1 - k^2 \sin^2\theta\right)^{-1/2} \mathrm{d}\theta\,, \tag{2.38}$$

$$E(k) = E(\pi/2,k) = \int_0^{\pi/2} \left(1 - k^2 \sin^2\theta\right)^{1/2} \mathrm{d}\theta\,. \tag{2.39}$$

Case 3. If $\phi < 0$, then we may exploit the fact that the incomplete elliptic functions of the first and second kind are odd functions of ϕ and use the following relationships

$$F(-\phi,k) = -F(\phi,k), \quad E(-\phi,k) = -E(\phi,k). \tag{2.40}$$

Case 4. If the amplitude ϕ exceeds $\pi/2$, then the integral can be written in terms of complete elliptic integrals plus incomplete elliptic integrals, using the following formulae,

$$F(n\pi \pm \phi,k) = 2nK(k) \pm F(\phi,k), \quad E(n\pi \pm \phi,k) = 2nE(k) \pm E(\phi,k).$$

where n is an integer.

When the elliptic modulus $k = 0$ or $k = 1$, the integrals are simply evaluated using standard integration techniques. Detailed information about elliptic integrals and their relationships with other special functions such as *hypergeometric* functions are covered in detail in Ref. [64, 65, 66, 67]. Finally, we comment that symbolic computational programs, such as MATLAB, Maple, and Mathematica, often subtly differ in dealing with elliptic integrals. Each software package uses different conventions for the arguments of the elliptic integrals ϕ and k. Table 2.1 summarises the different representations of the elliptic integrals in each package, where the MATLAB representation is used throughout this work.

2.1.4 Cardano's method

In this subsection, we introduce a useful method for solving a cubic equation known as Cardano's method. This method is named after Gerolamo Cardano, a 16^{th} century Italian mathematician whose book contains the solution to the cubic equation [68]. Suppose we wish to solve an equation of the form

$$a_3\,t^3 + a_2\,t^2 + a_1\,t + a_0 = 0, \tag{2.41}$$

where t is an arbitrary variable and $a_i \in \mathbb{R}$ are constant for $i = 0, \ldots, 3$, and $a_3 \neq 0$. We now follow Cardano's method to find the roots of (2.41). First, we eliminate the square term by using the substitution $t = \omega - (a_2/3a_3)$ which reduces (2.41) to

$$\omega^3 + p\,\omega + q = 0, \tag{2.42}$$

where

$$p = \frac{3\,a_3\,a_1 - a_2^2}{3\,a_3^2}, \quad q = \frac{2\,a_2^3 - 9\,a_3\,a_2\,a_1}{(3\,a_3)^3} + \frac{a_0}{a_3}. \tag{2.43}$$

We now substitute $\omega = \omega_1 + \omega_2$ into (2.42) which leads to

$$\omega_1^3 + \omega_2^3 + (\omega_1 + \omega_2)\,(3\,\omega_1\,\omega_2 + p) + q = 0.$$

Table 2.1: Elliptic integrals representations used in different symbolic computational programs.

Expression	MATLAB	Maple	Mathematica
(2.36)	ellipticF(ϕ, k^2)	EllipticF($\sin\phi$, k)	EllipticF[ϕ, k^2]
(2.37)	ellipticE(ϕ, k^2)	EllipticE($\sin\phi$, k)	EllipticE[ϕ, k^2]
(2.38)	ellipticK(k^2)	EllipticK(k)	EllipticK[k^2]
(2.39)	ellipticE(k^2)	EllipticE(k)	EllipticE[k^2]

If we let $3\,\omega_1\,\omega_2 + p = 0$, we may obtain the following system of equations

$$\omega_1^3 + \omega_2^3 = -q, \quad \omega_1^3\,\omega_2^3 = -\left(\frac{p}{3}\right)^3.$$

The above system of equations presents the sum and the product of ω_1^3 and ω_2^3 which means there is a quadratic equation of the form

$$\bar{\omega}^2 + q\,\bar{\omega} - \left(\frac{p}{3}\right)^3 = 0, \tag{2.44}$$

whose roots are ω_1^3 and ω_2^3 given by

$$\omega_1^3 = -\frac{q}{2} + \sqrt{\frac{q^2}{4} + \frac{p^3}{27}}, \quad \omega_2^3 = -\frac{q}{2} - \sqrt{\frac{q^2}{4} + \frac{p^3}{27}}.$$

We note that there are three cubic roots of ω_1 and ω_2. The type of these roots depends now on the sign of the discriminant $\mathcal{D} = -27\,q^2 - 4\,p^3$. If $\mathcal{D} > 0$, then the roots are complex. If $\mathcal{D} = 0$, then the roots are real with a multiplicity root. If $\mathcal{D} < 0$, then the roots are distinct, with one being real and the other two being complex conjugates. Recall that the solutions of (2.42) we seek are of the form $\omega = \omega_1 + \omega_2$. These solutions must also satisfy our assumption $\omega_1\,\omega_2 = -p/3$, and therefore the solutions are either written as

$$\omega = \omega_1 - \frac{p}{3\,\omega_1}, \quad \text{or} \quad \omega = \omega_2 - \frac{p}{3\,\omega_2}.$$

For instance, if we express our solutions in terms of ω_1 where the discriminant $\mathcal{D} < 0$, then the three solutions of (2.42) are written in the form

$$\omega = \omega_1 - \frac{p}{3\,\omega_1},$$

for each cubic root of ω_1, which are in this case

$$\omega_1 = \left[-\frac{q}{2} + \sqrt{\frac{q^2}{4} + \frac{p^3}{27}}\right]^{1/3}, \tag{2.45}$$

$$\omega_1 = \left(\frac{-1 + i\sqrt{3}}{2}\right)\left[-\frac{q}{2} + \sqrt{\frac{q^2}{4} + \frac{p^3}{27}}\right]^{1/3},$$

$$\omega_1 = \left(\frac{-1 - i\sqrt{3}}{2}\right)\left[-\frac{q}{2} + \sqrt{\frac{q^2}{4} + \frac{p^3}{27}}\right]^{1/3}.$$

2.2 Modelling approach

2.2.1 Lennard-Jones potential

As discussed in Section 1.3, the vdW interactions between graphene layers or between graphene layers and the substrate play a significant role in the formation of graphene ripples, folds, and wrinkles. The vdW interaction arises from a combination of the attractive and the repulsive forces between two atoms or molecules. The non-bonded interaction energy may be calculated directly using a discrete atom–atom formulation by adding the interaction energy between each atom pair, namely

$$V_d = \sum_i \sum_j \Phi(\varrho_{ij}), \tag{2.46}$$

where $\Phi(\varrho_{ij})$ denotes the potential function for each atom pair i and j separated by a distance ϱ_{ij}. When calculating interaction energy for molecules with large number of atoms, this discrete approach is often not convenient due to its computational cost. An alternative approach is to employ a continuum approximation that assumes a uniform distribution of the atoms over an identical surface representing the lattice. In the continuum approximation, the summation is replaced by integrals over the surface area of the lattice,

$S_{\mathrm{u}},\ S_{\mathrm{v}}$. Thus, equation (2.46) may be rewritten as

$$V_c = D_{\mathrm{u}}\, D_{\mathrm{v}} \int_{S_{\mathrm{u}}} \int_{S_{\mathrm{v}}} \Phi(\varrho)\, \mathrm{d}S_{\mathrm{u}}\, \mathrm{d}S_{\mathrm{v}}\,, \tag{2.47}$$

where D_{u} and D_{v} represent the mean surface density of atoms on the molecule u, and the molecule v, respectively, while ϱ denotes the distance between the two typical surface elements $\mathrm{d}S_{\mathrm{u}}$ and $\mathrm{d}S_{\mathrm{v}}$ on each molecule. We comment that the vdW interaction has been modelled with a number of empirical potential functions, including the LJ potential and Morse potential [69, 70]. In this work, the 6–12 LJ potential is used to model the vdW interaction. For the interaction energy between a pair of non-bonded atoms separated by a distance ϱ, the 6–12 LJ potential is given by two equivalent expressions

$$\Phi(\varrho) = 4\xi \left[-\left(\frac{\sigma}{\varrho}\right)^6 + \left(\frac{\sigma}{\varrho}\right)^{12} \right] = -\frac{\mathcal{A}}{\varrho^6} + \frac{\mathcal{B}}{\varrho^{12}},$$

where ξ and σ are known as the LJ potential parameters, which are empirically determined, while $\mathcal{A} = 4\xi\sigma^6$, and $\mathcal{B} = 4\xi\sigma^{12}$ are positive constants of the attraction and repulsion, respectively. Fig. 2.5 shows how the LJ potential is characterised by the parameters ξ and σ. The values of these parameters, where they exist in the literature, usually correspond to interactions between identical chemical species. For interactions between different chemical species u and v, values for these parameters may be calculated using the empirical mixing rules,

$$\xi_{\mathrm{uv}} = \sqrt{\xi_{\mathrm{u}}\xi_{\mathrm{v}}}, \quad \sigma_{\mathrm{uv}} = \frac{\sigma_{\mathrm{u}} + \sigma_{\mathrm{v}}}{2}. \tag{2.48}$$

The continuum approximation and the 6–12 LJ potential have been employed by Baowan et al. [71, Ch. 3], to derive analytical expressions for the vdW interaction energy between different molecules or nanostructures.

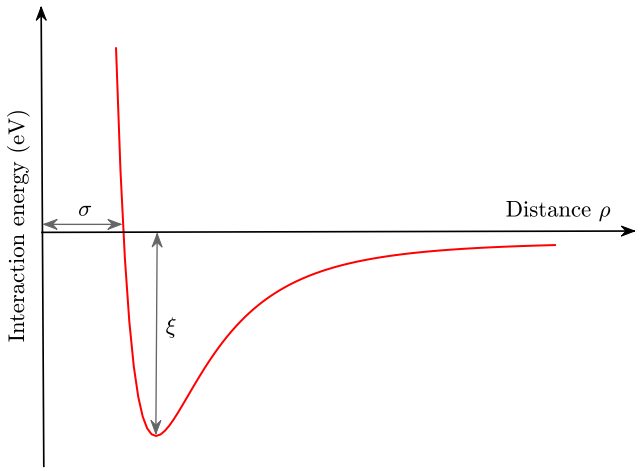

Figure 2.5: The LJ potential illustrating the energy well-depth ξ, and the vdW diameter σ.

Their modelling approach represents the interacting molecules by standard geometrical shapes, such as points, lines, planes, or even blocks, under the assumption of constant atomic density. Throughout this thesis, we follow their methods, and accordingly, the graphene–graphene and graphene–substrate vdW interaction energies are modelled as plane–plane and plane–volume interactions, respectively as represented by Fig. 2.6.

Graphene–Graphene interactions

As a part of modelling graphene configurations in this work, we need to account for the interactions between graphene sheets, which can be described as the interaction between two planes. An analytical formula for this kind of interaction has been derived employing the LJ potential along with the continuum approximation [71]. In this work, the formula is exploited to model the interaction energy between a pair of graphene sheets separated by

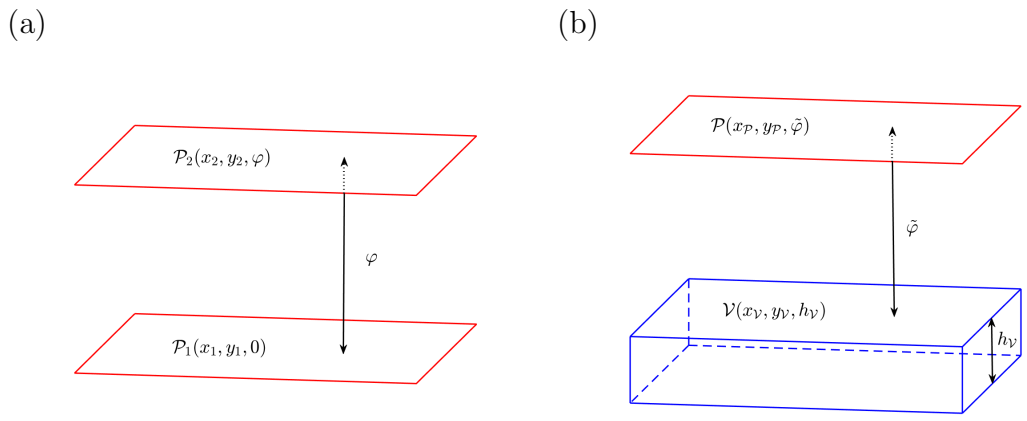

Figure 2.6: The interaction of: (a) two planes at a distance φ, and (b) plane with volume of a height $h_\mathcal{V}$ at a distance $\tilde{\varphi}$.

a distance φ as

$$\epsilon_{\mathrm{gg}}(\varphi) = D_{\mathrm{g}}^2 \left[-\frac{\pi \mathcal{A}_{\mathrm{gg}}}{2\varphi^4} + \frac{\pi \mathcal{B}_{\mathrm{gg}}}{5\varphi^{10}} \right], \tag{2.49}$$

where D_{g} denotes the surface density of carbon atoms on a sheet of graphene, while $\mathcal{A}_{\mathrm{gg}}$ and $\mathcal{B}_{\mathrm{gg}}$ are the graphene–graphene attractive and repulsive constants, respectively.

Graphene–Substrate interactions

Another type of interaction that needs to be taken into account in the modelling is the interaction between a plane and a volume. Such interactions are invoked in this work when modelling configurations of supported graphene. We now derive an analytical expression for the interaction energy between a graphene sheet and a three-dimensional substrate. After some rearrangement of (2.49), we find that the interaction energy between two planes, $\mathcal{P}_1$ and $\mathcal{P}_2$, is

$$\epsilon_{\mathcal{P}_1\mathcal{P}_2}(\varphi) = D_{\mathcal{P}_1} D_{\mathcal{P}_2} \left[-\frac{\pi \mathcal{A}_{\mathcal{P}_1\mathcal{P}_2}}{2\varphi^4} + \frac{\pi \mathcal{B}_{\mathcal{P}_1\mathcal{P}_2}}{5\varphi^{10}} \right]. \tag{2.50}$$

To involve the whole volume of the substrate in accounting for the interaction energy, we may proceed with a further integration on (2.50) to derive an expression for the interaction between a plane $\mathcal{P}$ and a volume $\mathcal{V}$ as

$$\epsilon_{\mathcal{PV}}(\varphi) = D_{\mathcal{P}} D_{\mathcal{V}} \int_0^{\infty} \left[-\frac{\pi \mathcal{A}_{\mathcal{PV}}}{2\left(\varphi + h_{\mathcal{V}}\right)^4} + \frac{\pi \mathcal{B}_{\mathcal{PV}}}{5\left(\varphi + h_{\mathcal{V}}\right)^{10}} \right] \mathrm{d}h_{\mathcal{V}} \,,$$

where the plane density $D_{\mathcal{P}}$ is replaced by the volume density $D_{\mathcal{V}}$. Therefore, the interaction energy between a graphene sheet and a three-dimensional substrate separated by $\tilde{\varphi}$, is modelled as

$$\epsilon_{\mathrm{gs}}(\tilde{\varphi}) = D_{\mathrm{g}} D_{\mathrm{s}} \left[-\frac{\pi \mathcal{A}_{\mathrm{gs}}}{6\tilde{\varphi}^3} + \frac{\pi \mathcal{B}_{\mathrm{gs}}}{45\tilde{\varphi}^9} \right], \tag{2.51}$$

where D_{s} denotes the volume density of the chemical species of the substrate, while $\mathcal{A}_{\mathrm{gs}}$ and $\mathcal{B}_{\mathrm{gs}}$ denote the graphene–substrate attractive and repulsive constants, respectively. In this case, the parameters $\mathcal{A}_{\mathrm{gs}}$ and $\mathcal{B}_{\mathrm{gs}}$ are determined using the empirical mixing rules given by (2.48).

2.2.2 Dominant energies

As discussed earlier, there are several approaches for modelling the configurations of graphene such as small-deformation theory [56] , finite-deformation theory [2], and the variational approach [3]. This thesis utilise the variational approach to model different configurations of graphene dominated by the elastic energy and the vdW energy. Therefore, we adopt the same considerations here to model these dominant energies. The variational approach assumes that any graphene configuration results from a competition between two dominant energies, which are the vdW interaction energy E_{v}, and the elastic bending energy E_{e}. A translational symmetry in the graphene structure is also assumed, which facilitates the modelling by considering 2D problems. Consequently, constants for the strength of the vdW interaction

energy are considered as energy per unit length rather than energy per unit area. The total energy of the system is then written as the sum of E_{v} and E_{e}, namely

$$E_{\mathrm{tot}} = E_{\mathrm{v}} + E_{\mathrm{e}}, \tag{2.52}$$

where these energies are expressed by line integrals, and the details about how they are modelled throughout this work are given in the remainder of this subsection.

Van der Waals interaction energy

The vdW interaction energy is assumed to be the dominant energy whenever the graphene sheet becomes parallel to another graphene sheet or to the substrate when it is supported. In this work, we disregard the vdW interaction energy in the graphene bended region as an approximation that we make in the modelling. Precisely, if we model a configuration represented by a curve C that comprises parallel regions C_p, and bended regions C_b. The vdW interaction energy is then modelled as

$$E_{\mathrm{v}} = -\epsilon \int_C u(x)\ \mathrm{d}s\,, \tag{2.53}$$

where ϵ denotes the vdW interaction energy per unit length, and $u(x)$ is a Heaviside unit step function, given by

$$u(x) = \begin{cases} 1, & \text{in } C_p, \\ 0, & \text{in } C_b. \end{cases}$$

The graphene–graphene vdW interaction energy ϵ_{gg}, and the graphene–substrate vdW interaction energy ϵ_{gs} are modelled using the LJ potential described in the previous subsection.

Elastic bending energy

The elastic bending energy is assumed to be proportional to the square of the curvature. We note that the curvature vanishes in the parallel regions of the curve C, and hence the elastic bending energy only originates in the bended regions of C. Thus, we model the elastic energy E_{e} mathematically with

$$E_{\mathrm{e}} = \gamma \int_C \kappa^2 \, \mathrm{d}s \,, \tag{2.54}$$

where γ is the bending rigidity of graphene, s is the arc length, and κ is the curvature of C given by

$$\kappa = \begin{cases} 0, & \text{in } C_p, \\ \dfrac{y''}{(1+y'^2)^{3/2}}, & \text{in } C_b, \end{cases}$$

where primes denote derivatives with respect to x. We note that the curvature κ may take forms as shown earlier in Section 2.1.1. Recall from Table 1.1 that the bending rigidity of single-layer graphene ranges from 0.83–1.61 eV [15]. Whenever confusion can be avoided, we adopt a linear sample from that range for γ in the analysis, namely $\gamma = \{0.8, 1.0, 1.2, 1.4, 1.6\}$ eV, for comparison purposes. In the next chapter, we utilise the calculus of variations, described in Section 2.1.2, to construct a variational model for a rippled graphene sheet.

2.3 Nomenclature

Symbol	Description
$\dot{\square}$	the derivative of $\square$ with respect to t
$\square'$	the derivative of $\square$ with respect to x
θ	the angle made by the tangent vector with the horizontal axis
κ	the line curvature
s	the arc length of a curve
R	the radius of the curvature
$\mathbf{r}(t)$	the position vector of points on a curve parametrised by t
$\square_{\mathrm{a}}$, $\square_{\mathrm{b}}$	endpoints of the interval for the variable $\square$
J	a functional mapping a set of functions to real numbers
U, S, $\mathcal{H}$	sets of functions defined on a particular vector space
$\tilde{\square}$	ε–neighbourhood variation of the function $\square$
η, χ	arbitrary differentiable functions
δ	the variation of a functional or variable
F	the integrand part of a functional
$F_{\square}$	the partial derivative of F with respect to the variable $\square$
P, Q	the canonical coordinate transformations
$H(P,Q)$	the Hamiltonian function
$\mathcal{R}/T$	rational/polynomial functions
F/K	the incomplete/complete elliptic integrals of the first kind
E/Π	the elliptic integrals of the second/third kind
ϕ/k	the amplitude/elliptic modulus of elliptic integrals
ω	a substitution used to write an equation as a cubic equation
$\mathcal{D}$	the discriminant of a cubic equation
$V_{d/c}$	discrete/continuous formulation for the interaction energy

$D_{\square}$	the mean surface or volume density of atoms on the molecule $\square$
$\Phi(\varrho_{ij})$	the LJ potential function for two unbounded atoms
ϱ_{ij}	the distance between two unbounded atoms i and j
ξ/σ	the energy well depth/vdW diameter
$\mathcal{A}/\mathcal{B}$	positive constants of the attraction/repulsion
$\mathcal{P}$, $\mathcal{V}$, $h_{\mathcal{V}}$	plane, volume, height of volume
$\epsilon_{\mathrm{gg}}(\varphi)$	the graphene–graphene vdW interaction strength at a distance φ
$\mathcal{A}_{\mathrm{gg}}/\mathcal{B}_{\mathrm{gg}}$	positive constants of the graphene–graphene attraction/repulsion
$\epsilon_{\mathrm{gs}}(\tilde{\varphi})$	the graphene–substrate vdW interaction strength at a distance $\tilde{\varphi}$
$\mathcal{A}_{\mathrm{gs}}/\mathcal{B}_{\mathrm{gs}}$	positive constants of the graphene–substrate attraction/repulsion
E_{tot}	the total energy of the conformation
E_{e}	the graphene elastic energy
E_{v}	the vdW interaction energy
$u(x)$	a Heaviside unit step function
ϵ	the vdW interaction strength per unit length
C_p/C_b	the parallel/bended regions of the curve C
γ	the bending rigidity of graphene

Chapter 3

Single–layer graphene ripples

3.1 Introduction

Graphene is ideally thought of as a flat sheet composed of carbon atoms. However, out–of–plane deformations have been observed in CVD-produced graphene, as discussed in Section 1.3. One commonly observed out–of–plane deformation is the ripple, a bump with low-aspect ratio, so that the graphene sheet is close to but not perfectly flat. Ripples are observed in both supported graphene on a substrate [39], and suspended graphene [72]. These ripples often occur at the edges of the graphene or close to defect sites. The pattern of ripples in graphene may be affected by a variety of environmental factors, including temperature, substrate material, and the size of the graphene sheet.

Suspended graphene remains flat with no ripples when the temperature is close to absolute zero, but ripples begin to appear as the temperature increases [73]. When graphene is grown on a substrate by CVD, the amplitude of the ripples depends on the substrate properties, such as roughness and interfacial vdW interactions [39]. It has also been observed that the overall size of the graphene sheet has a significant impact on the amplitude of rip-

ples, with the ripple amplitude increasing proportionally with the size of the sheet [74].

Experimental studies of rippled graphene find that the electronic properties of graphene can be affected by the width and height of the ripples [46, 47]. While flat graphene with a zero-gap in Fermi energies is a very good conductor, ripples introduce a band gap to the graphene, thus making a variable semiconductor. Gui et al. [48] report that the band gap increases proportionally with ripple amplitude, which is the maximum distance between the graphene sheet and the substrate. They evaluate a direct band gap at 0.93 eV, meaning that rippled graphene is a good semiconductor. Ripples also alter the elasticity of the graphene, which suggests rippled graphene as a beneficial material for elastic bio-sensing applications [75].

An important mechanical property of solid matter is Young's modulus which measures the ability of a material to resist elastic deformations under lengthwise tension or compression. While planar graphene has a Young's modulus of 1 TPa [10], the presence of ripples or wrinkles in graphene decreases Young's modulus of graphene [76, 77]. However, it has been reported that Young's modulus increases when ripples are suppressed with a strain [78]; consequently, modifying the structure of graphene requires more force. Although ripples lead to both negative and positive effects, understanding the mechanism of ripple formation can help control their morphologies, and hence, the material properties of the rippled graphene.

In this chapter, we develop a mathematical model for a rippled graphene sheet utilising the calculus of variations. In the following section, a general model of a single graphene ripple on a substrate is formulated. In Section 3.3 the model is non-dimensionalised and the calculus of variations is employed assuming a fixed length (isoperimetric) constraint of both the rip-

pled graphene sheet and the substrate. In Section 3.4 we relax the isoperimetric constraint on the sheet length, but maintain a fixed substrate length. The substrate length is varied in Section 3.5 and an isoperimetric constraint is applied to only the sheet length. The solutions and associated numerical details are provided with each case. The main results and the relationships between the three cases considered here are described in Section 3.6. Discussion and some concluding remarks are made in Section 3.7.

3.2 Model formulation

We now propose a general formulation to determine the conformation of a rippled sheet of graphene on a substrate. The geometry of the rippled graphene sheet is shown in Fig. 3.1. We assume a translational symmetry in the z–direction, which reduces the problem to that of finding a curve in two dimensions. Also, the assumed reflective symmetry about the y–axis allows us to consider only solutions in the right half plane. The solution curve is divided into three sections. The first section C_1 is the curve from the point $(0, h_{\text{rip}})$ to the point (x_0, y_0) where the line curvature is strictly negative. The second section C_2 is from (x_0, y_0) to $(x_1, \delta_{\text{gs}})$ where the line curvature is strictly positive. The third section C_3 is the horizontal line from $(x_1, \delta_{\text{gs}})$ to $(x_2, \delta_{\text{gs}})$ where the line curvature is zero. The concatenation of these sections is denoted by $C = C_1 + C_2 + C_3$. In the preceding position vectors, we use h_{rip} to denote the ripple height, and δ_{gs} to denote the separation distance between the substrate and the flat section of the graphene sheet.

The conformation of a rippled graphene sheet supported on a substrate is modelled by considering two dominant energies. These energies originate from the elastic bending deformation of the graphene sheet and the vdW

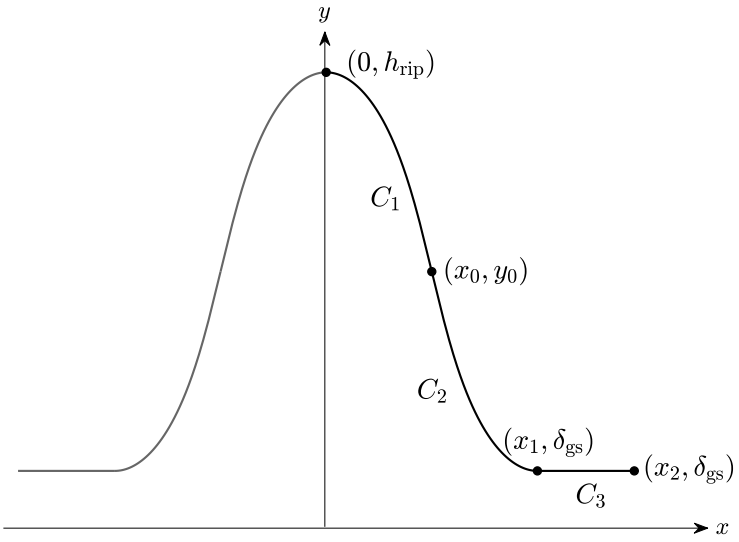

Figure 3.1: Schematic showing the geometry of a rippled graphene sheet.

interactions between graphene and the substrate. The elastic energy E_{e} is modelled with

$$E_{\mathrm{e}} = \gamma \int_C \kappa^2 \, \mathrm{d}s \,,$$

where γ is the bending rigidity of graphene, s is the arc length, and κ is the line curvature of $y = y(x)$ which is given by

$$\kappa = \frac{\ddot{y}}{(1 + \dot{y}^2)^{3/2}},$$

where dots denote differentiation with respect to x. For the purpose of comparison, a linear sample of values for γ is adopted in the analysis, namely $\gamma = \{0.8, 1.0, 1.2, 1.4, 1.6\}$ eV. We model the vdW interaction energy between the graphene and the substrate as

$$E_{\mathrm{v}} = -\epsilon_{\mathrm{gs}} \int_C u(x - x_1) \, \mathrm{d}s \,,$$

where ϵ_{gs} denotes the graphene–substrate vdW interaction energy per unit length, and $u(x - x_1)$ is the Heaviside unit step function.

As discussed in Section 2.2.2, the model in this study assumes that the elastic energy dominates in the bended regions, denoted by C_1 and C_2, while the vdW interaction dominates in the parallel region, denoted by C_3. We comment that the curvature, and therefore the elastic energy, vanishes in C_3. However, discarding the vdW interaction in C_1 and C_2 is an approximation made in the modelling. Therefore, the total energy per unit length may be expressed by

$$E_{\text{tot}} = E_{\text{e}} + E_{\text{v}} = \gamma \int_{C_1+C_2} \kappa^2 \, \mathrm{d}s - \epsilon_{\text{gs}} \left(x_2 - x_1\right), \tag{3.1}$$

subject to the boundary conditions

$$x(0) = 0, \quad y(0) = h_{\text{rip}}, \quad \dot{y}(0) = 0, \quad y(x_1) = \delta_{\text{gs}}, \quad \dot{y}(x_1) = 0, \tag{3.2}$$

where h_{rip} is an input into the model to be prescribed, but the value of x_1 is not prescribed and a natural boundary condition on x. This model is now applied to consider three cases for a rippled graphene sheet located on a substrate, taking into account the location of the ripple edge on the substrate. As illustrated by Fig. 3.2, the transitional case addresses the case when the ripple edge and the substrate coincide, the substrate constrained case applies when the ripple edge overhangs the substrate, and the graphene constrained case accounts for the case when the ripple edge does not extend to the substrate.

As mentioned in Section 1.3, the substrate properties, such as roughness and vdW interaction strength, play an important role in the formation of graphene ripples during the CVD process. This has led to considerable interest in the study of graphene–metal interfaces. A study based on density functional theory is reported by Giovannetti et al. [79], which classifies metal(111) surfaces into two groups. The first group comprises those metals known to bind weakly on graphene such as Cu(111), while the second group

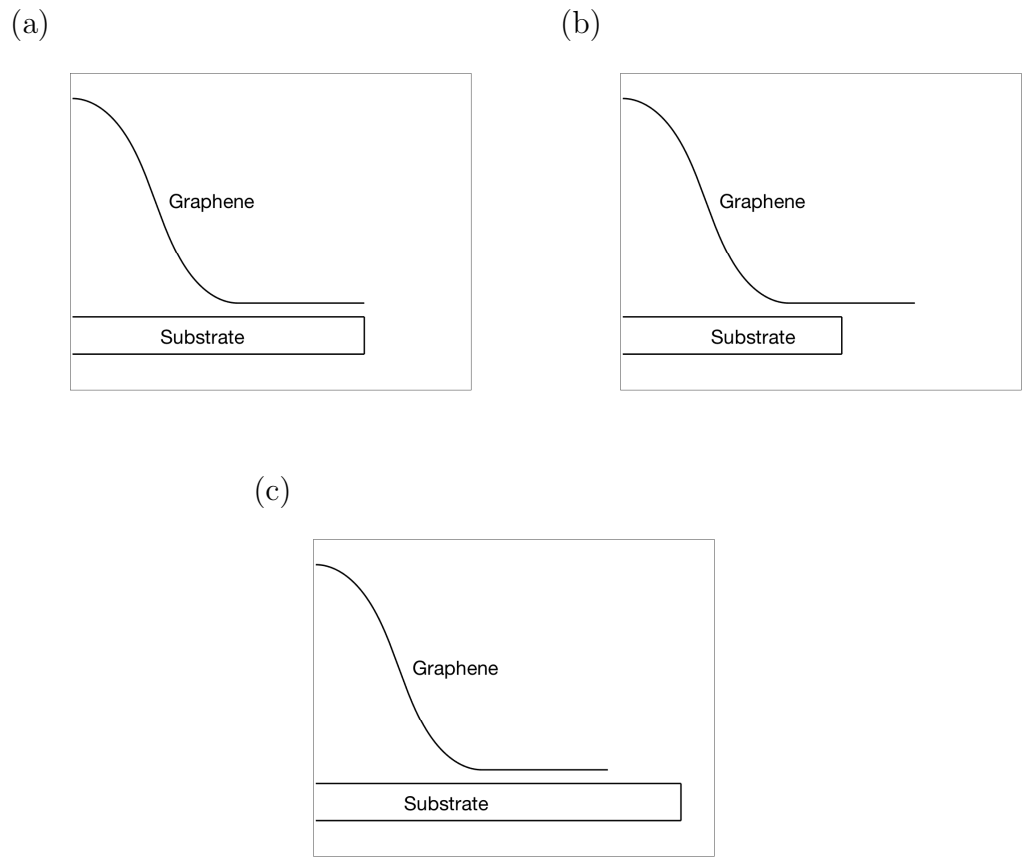

Figure 3.2: Schematic showing the geometries of: (a) the transitional case, (b) the substrate constrained case, and (c) the graphene constrained case.

comprises those metals known to bind strongly such as Ni(111). Therefore, the Cu(111) and Ni(111) substrates are adopted into this model for analysis and comparison purposes. Moreover, a particular value of h_{rip} prescribed for each case of a rippled graphene sheet supported on a different substrate, and the reason for adopting these particular values is explained in Section 3.4. The prescribed ripple height, h_{rip}, and empirical values for the separation distance between graphene and the substrate, δ_{gs}, and the vdW energy of graphene–substrate interactions per unit length, ϵ_{gs}, corresponding to each

substrate are presented in Table 3.1.

3.3 The transitional case

3.3.1 Analytical solutions

The calculus of variations is now applied to determine the conformation of a rippled graphene sheet and derive a solution for which the functional (3.1) is minimised. We impose an isoperimetric constraint on the total arc length of C, given by

$$\int_C \mathrm{d}s = L_{\mathrm{tot}},$$

where L_{tot} is the total arc length of the curve C. Moreover, it is assumed that x_2 is fixed, but x_1 varies (to be determined from a natural boundary condition). Therefore, the new functional we wish to minimise is of the form

$$E_{\mathrm{tot}} = \int_{C_1+C_2} \left(\gamma\kappa^2 + \lambda\right) \mathrm{d}s + \left(\lambda - \epsilon_{\mathrm{gs}}\right)\left(x_2 - x_1\right), \tag{3.3}$$

subject to the boundary conditions (3.2), where λ is a Lagrange multiplier corresponding to the isoperimetric constraint. We nondimensionalise (3.3) by defining $X = x/\alpha$ and $Y = y/\alpha$ where α is a scaling factor, and therefore $\ddot{y} = Y''/\alpha$ and $\dot{y} = Y'$, where primes denote derivatives with respect to

Table 3.1: Empirical values for δ_{gs} and ϵ_{gs}, with the prescribed ripple height h_{rip} for each case of a rippled graphene sheet on a substrate.

Substrate	δ_{gs} (Å)	ϵ_{gs} (eVÅ^{-2})	h_{rip} (Å)
Cu(111)	3.25 [80]	0.02481 [81]	$8.0\,\delta_{\mathrm{gs}}$
Ni(111)	2.10 [82]	0.09133 [81]	$6.7\,\delta_{\mathrm{gs}}$

the nondimensional X coordinate. The substitution of the nondimensional variables into (3.3) yields

$$E_{\text{tot}} = \int_0^{X_1} \left[\frac{\gamma}{\alpha^2} \frac{Y''^2}{\left(1+Y'^2\right)^{5/2}} + \lambda \left(1+Y'^2\right)^{1/2} \right] \alpha \, \mathrm{d}X + \alpha \left(\lambda - \epsilon_{\text{gs}}\right) \left(X_2 - X_1\right).$$

Furthermore, the fixed energy at X_2 is subtracted, and both sides are divided by $\alpha\epsilon_{\text{gs}}$. Thus, we derive the nondimensionalised energy functional as

$$\hat{E}_{\text{tot}} = \int_0^{X_1} \left[\frac{\gamma}{\epsilon_{\text{gs}}\alpha^2} \frac{Y''^2}{\left(1+Y'^2\right)^{5/2}} + \frac{\lambda}{\epsilon_{\text{gs}}} \left(1+Y'^2\right)^{1/2} \right] \mathrm{d}X + \left(1 - \lambda/\epsilon_{\text{gs}}\right) X_1, \tag{3.4}$$

where $\hat{E}_{\text{tot}}$ may be written in terms of E_{tot} as

$$\hat{E}_{\text{tot}} = E_{\text{tot}}/\alpha\epsilon_{\text{gs}} + \left(1 - \lambda/\epsilon_{\text{gs}}\right) X_2.$$

For simplicity, we let $\alpha = \sqrt{\gamma/\epsilon_{\text{gs}}}$ and $\mu = \lambda/\epsilon_{\text{gs}}$ in (3.4) so that

$$\hat{E}_{\text{tot}} = \int_0^{X_1} \left[\frac{Y''^2}{\left(1+Y'^2\right)^{5/2}} + \mu \left(1+Y'^2\right)^{1/2} \right] \mathrm{d}X + (1-\mu) X_1, \tag{3.5}$$

which represents a variational problem containing second–order derivatives with a natural boundary condition that applies at $X = X_1$.

To simplify the following calculations, F is used to denote the integrand of (3.5), that is

$$F(Y', Y'') = \frac{Y''^2}{\left(1+Y'^2\right)^{5/2}} + \mu \left(1+Y'^2\right)^{1/2}. \tag{3.6}$$

As summarised in Section 2.1.2, extremals of a functional of this kind are given by the Euler–Poisson equation

$$F_Y - \frac{\mathrm{d}}{\mathrm{d}X} F_{Y'} + \frac{\mathrm{d}^2}{\mathrm{d}X^2} F_{Y''} = 0, \tag{3.7}$$

where F is assumed to have continuous partial derivatives of the third order with respect to all of its arguments. Since equation (3.6) does not depend on

Y explicitly, then on integrating (3.7) with respect to X, we obtain the first integral

$$F_{Y'} - \frac{\mathrm{d}}{\mathrm{d}X} F_{Y''} = \beta, \tag{3.8}$$

where β is a constant. Furthermore, the integrand has no explicit dependence on X; this provides an additional first integral

$$\left(F_{Y'} - \frac{\mathrm{d}}{\mathrm{d}X} F_{Y''} \right) Y' + F_{Y''} Y'' - F = H,$$

from which we may replace the terms in the parentheses by the constant β from the first integral (3.8) to write the Hamiltonian energy function H as

$$\beta Y' + F_{Y''} Y'' - F = H, \tag{3.9}$$

where H is also a constant. Due to the presence of a natural boundary condition, we also consider the first variation of $\hat{E}_{\mathrm{tot}}$, which is equivalent to that given by (2.27) except that the present problem contains an additional term. Taking the variation of the additional term into account, the standard equation for the first variation of $\hat{E}_{\mathrm{tot}}$ is given by

$$\begin{aligned} \delta \hat{E}_{\mathrm{tot}} = {} & [P\,\delta Y + Q\,\delta Y' - H\,\delta X]_{X=X_1} \\ & + \int_0^{X_1} \left(F_Y - \frac{\mathrm{d}}{\mathrm{d}X} F_{Y'} + \frac{\mathrm{d}^2}{\mathrm{d}X^2} F_{Y''} \right) \delta Y \,\mathrm{d}X + (1-\mu)[\delta X]_{X=X_1}, \end{aligned}$$

where

$$P = F_{Y'} - \frac{\mathrm{d}}{\mathrm{d}X} F_{Y''}, \quad Q = F_{Y''}, \quad \text{and} \quad H(P,Q) = PY' + QY'' - F.$$

The natural boundary condition, which applies when the X–coordinate at the end point $X = X_1$ is not prescribed, requires $H = (1-\mu)$. Therefore, by combining (3.8) and (3.9), we obtain

$$\beta Y' + F_{Y''} Y'' - F = (1-\mu).$$

After the substitution of (3.6), we may derive

$$\hat{\kappa}^2 = \frac{Y''^2}{(1+Y'^2)^3} = \mu + \frac{(1-\mu) - \beta Y'}{(1+Y'^2)^{1/2}},$$

or equivalently

$$\hat{\kappa} = \pm \left(\mu + \frac{(1-\mu) - \beta Y'}{(1+Y'^2)^{1/2}} \right)^{1/2},$$

which gives the nondimensional curvature $\hat{\kappa}$ in terms of the first derivative of Y. In order to obtain the parametric solutions, we make the substitution of $Y' = \tan\theta$, which yields

$$\hat{\kappa} = \pm \left[\mu + (1-\mu)\cos\theta - \beta \sin\theta \right]^{1/2}.$$

The above expression may be written as follows

$$\hat{\kappa} = \pm \left\{ \mu + (1-\mu)\sec\psi \left[\cos\psi \, \cos\theta - \cos\psi \, \sin\theta \right] \right\}^{1/2},$$

where the new parameter ψ is defined such that

$$\cos\psi = \frac{1-\mu}{\sqrt{(1-\mu)^2 + \beta^2}}, \quad \text{and} \quad \sin\psi = \frac{\beta}{\sqrt{(1-\mu)^2 + \beta^2}}.$$

This leads to the succinct formula

$$\hat{\kappa} = \pm \left[\mu + (1-\mu)\sec\psi \, \cos(\psi + \theta) \right]^{1/2}. \tag{3.10}$$

Upon using the fact that

$$\hat{\kappa} = \cos\theta \, \frac{\mathrm{d}\theta}{\mathrm{d}X} = \sin\theta \, \frac{\mathrm{d}\theta}{\mathrm{d}Y},$$

two first order differential equations are derived, namely

$$\begin{aligned} \frac{\mathrm{d}X}{\mathrm{d}\theta} &= \pm \frac{\cos\theta}{\left[\mu + (1-\mu)\sec\psi \cos(\psi+\theta) \right]^{1/2}}, \\ \frac{\mathrm{d}Y}{\mathrm{d}\theta} &= \pm \frac{\sin\theta}{\left[\mu + (1-\mu)\sec\psi \cos(\psi+\theta) \right]^{1/2}}. \end{aligned} \tag{3.11}$$

To facilitate further integration, we change the parametric variable of our equations from θ to ϕ such that $\theta = 2\phi - \psi$; thus, equation (3.11) takes the following forms

$$\begin{aligned}\frac{\mathrm{d}X}{\mathrm{d}\phi} &= \pm\left[\frac{2\left(\cos\psi\cos 2\phi + \sin\psi\sin 2\phi\right)}{\left(\mu + (1-\mu)\sec\psi - 2(1-\mu)\sec\psi\sin^2\phi\right)^{1/2}}\right],\\ \frac{\mathrm{d}Y}{\mathrm{d}\phi} &= \pm\left[\frac{2\left(\cos\psi\sin 2\phi - \sin\psi\cos 2\phi\right)}{\left(\mu + (1-\mu)\sec\psi - 2(1-\mu)\sec\psi\sin^2\phi\right)^{1/2}}\right],\end{aligned} \tag{3.12}$$

and so general solutions are obtained by integrating (3.12). This yields

$$\begin{aligned}X(\phi) &= c_1 \pm A\left[\cos\psi\left(E(\phi,k) - BF(\phi,k)\right) - \sin\psi\left(1 - k^2\sin^2\phi\right)^{1/2}\right],\\ Y(\phi) &= c_2 \mp A\left[\sin\psi\left(E(\phi,k) - BF(\phi,k)\right) + \cos\psi\left(1 - k^2\sin^2\phi\right)^{1/2}\right],\end{aligned}$$

with the parameters

$$A = \frac{2(\mu + (1-\mu)\sec\psi)^{1/2}}{(1-\mu)\sec\psi}, \quad B = \frac{\mu}{\mu + (1-\mu)\sec\psi},$$
$$k = \left(\frac{2(1-\mu)\sec\psi}{\mu + (1-\mu)\sec\psi}\right)^{1/2},$$

where $F(\phi,k)$ and $E(\phi,k)$ represent incomplete elliptic integrals of the first and second kind, respectively, with elliptic modulus k, and c_1, c_2 being arbitrary constants of integration.

We now define two functions which play a significant role in determining our parametric solutions, namely

$$\begin{aligned}g_1(\phi) &= A\left(1 - k^2\sin^2\phi\right)^{1/2},\\ g_2(\phi) &= A\left[\left(E(\phi,k) - E(\phi_0,k)\right) - B\left(F(\phi,k) - F(\phi_0,k)\right)\right].\end{aligned} \tag{3.13}$$

The line curvature changes sign at $\phi_0 = \sin^{-1}(1/k)$ corresponding to (X_0, Y_0) which is the boundary point between the two curves C_1 and C_2, which has coordinates

$$\begin{aligned}X_0 &= \left[\sin\psi\, g_1(\psi/2) - \cos\psi\, g_2(\psi/2)\right],\\ Y_0 &= \frac{h_{\mathrm{rip}}}{\alpha} - \left[\sin\psi\, g_2(\psi/2) + \cos\psi\, g_1(\psi/2)\right].\end{aligned} \tag{3.14}$$

Moreover, the solutions are shown to have a rotational symmetry about this critical point (X_0, Y_0) where ϕ varies over the range $[\psi/2, \phi_0]$. Thus, the nondimensional parametric solutions of C_1 and C_2 may be written in terms of X_0 and Y_0 as

$$X_{C_1/C_2}(\phi) = X_0 \pm [\cos\psi\, g_2(\phi) - \sin\psi\, g_1(\phi)]\,,$$
$$Y_{C_1/C_2}(\phi) = Y_0 \pm [\sin\psi\, g_2(\phi) + \cos\psi\, g_1(\phi)]\,.$$

Now, using the boundary condition $Y_{C_2}(\psi/2) = \delta_{\rm gs}/\alpha$, we may obtain

$$\frac{\delta_{\rm gs} - h_{\rm rip}}{2\alpha} = -\,[\sin\psi\, g_2(\psi/2) + \cos\psi\, g_1(\psi/2)]\,.$$

Hence, the second equation in (3.14) may be written as

$$Y_0 = \frac{h_{\rm rip} + \delta_{\rm gs}}{2\alpha},$$

which introduces the Y component of the critical point as the midpoint of the ripple amplitude and the flat section of the graphene sheet. It is also noted that $x = \alpha X$ and $y = \alpha Y$, so multiplying these solutions by the scaling factor $\alpha = \sqrt{\gamma/\epsilon_{\rm gs}}$ recovers the dimensional solutions.

3.3.2 Numerical results

We are left with two parameters to determine, namely ψ and μ. Their values are found by solving the following system of equations numerically

$$y_{C_2}(\psi/2) = \delta_{\rm gs}, \quad \text{and} \quad \int_C \mathrm{d}s = L_{\rm tot},$$

where $\delta_{\rm gs}$ takes a specific empirically determined value for each substrate as given in Table 3.1, and L is the assumed fixed arc length of C. After finding the unknowns ψ and μ, the solution is fully determined and representative plots are shown in Fig. 3.3.

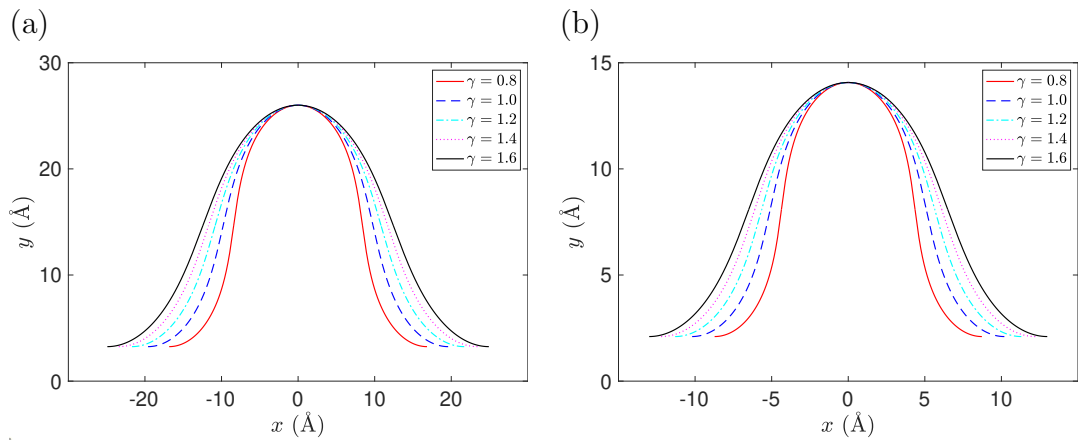

Figure 3.3: Rippled graphene sheet located on: (a) Cu(111) substrate and (b) Ni(111) substrate for various values of γ, in the transitional case. The substrate surface is set to be at the horizontal axis.

At this point, we can obtain an expression for the total half arc length of the ripple L_{rip} by integrating $\mathrm{d}s$ over the curve $C_1 + C_2$,

$$L_{\text{rip}} = \sqrt{\gamma/\epsilon_{\text{gs}}}\Bigg[\int_{\theta_0}^{\theta 1} \left[\mu + (1-\mu)\sec\psi\,\cos\left(\psi+\theta\right)\right]^{-1/2}\mathrm{d}\theta - \int_{\theta_1}^{\theta_2} \left[\mu + (1-\mu)\sec\psi\,\cos\left(\psi+\theta\right)\right]^{-1/2}\mathrm{d}\theta\Bigg].$$

Again, using the substitution $\theta = 2\phi - \psi$ we deduce that

$$L_{\text{rip}} = \frac{2}{\rho}\sqrt{\gamma/\epsilon_{\text{gs}}}\Bigg[\int_{\psi/2}^{\phi_0}\left(1-k^2\sin^2\phi\right)^{-1/2}\mathrm{d}\phi - \int_{\phi_0}^{\psi/2}\left(1-k^2\sin^2\phi\right)^{-1/2}\mathrm{d}\phi\Bigg],$$

where $\rho = \sqrt{\mu + (1-\mu)\sec\psi}$. Hence, the total half arc length of the ripple is given by

$$L_{\text{rip}} = \frac{4}{\rho}\sqrt{\gamma/\epsilon_{\text{gs}}}\Big[F(\phi_0,k) - F(\psi/2,k)\Big]. \tag{3.15}$$

The elastic energy may also be calculated by integrating the square of the line curvature over the total length of $C_1 + C_2$, as follows

$$E_{\text{e}} = 2\rho\sqrt{\gamma\epsilon_{\text{gs}}}\Bigg[\int_{\psi/2}^{\phi_0}\left(1-k^2\sin^2\phi\right)^{1/2}\mathrm{d}\phi - \int_{\phi_0}^{\psi/2}\left(1-k^2\sin^2\phi\right)^{1/2}\mathrm{d}\phi\Bigg],$$

and therefore, the elastic energy is

$$E_{\mathrm{e}} = 4\rho\sqrt{\gamma\epsilon_{\mathrm{gs}}}\,[E(\phi_0, k) - E(\psi/2, k)]\,.$$

Hence, the total energy per unit length for this model is

$$E_{\mathrm{tot}} = 4\rho\sqrt{\gamma\epsilon_{\mathrm{gs}}}\,[E(\phi_0, k) - E(\psi/2, k)] - \epsilon_{\mathrm{gs}}\,(x_2 - x_1)\,. \tag{3.16}$$

Numerical values for the x–component of the critical point (x_0, y_0) and the total half arc length of the ripple L_{rip} are presented in Table 3.2, for a range of values of the bending rigidity γ. The vdW interaction ϵ_{gs} takes a specific empirically derived value for each substrate as given in Table 3.1.

3.4 The substrate constrained case

3.4.1 Analytical solutions

The particular case, shown in Fig. 3.2(b), is now considered, which involves removing the assumed isoperimetric constraint on the total arc length of

Table 3.2: The x–component of the critical point and the ripple half arc length L_{rip} for various bending rigidities γ, in the transitional case.

γ (eV)	Cu(111) substrate		Ni(111) substrate	
	x_0 (Å)	L_{rip} (Å)	x_0 (Å)	L_{rip} (Å)
0.8	8.42	30.86	4.36	16.17
1.0	9.80	32.29	5.10	16.92
1.2	10.84	33.52	5.65	17.57
1.4	11.71	34.61	6.11	18.14
1.6	12.45	35.59	6.50	18.65

C to allow graphene to overhang the substrate. Therefore, we discard the variation of x_2 and substitute $\lambda = 0$, and $\alpha = \sqrt{\gamma/\epsilon_{\rm gs}}$ into (3.4) to obtain the functional that we wish to minimise, that is

$$\hat{E}_{\rm tot} = \int_0^{X_1} \frac{Y''^2}{(1+Y'^2)^{5/2}}\,\mathrm{d}X + X_1. \tag{3.17}$$

This expression is identical to (3.5) with $\mu = 0$, and so, by the same reasoning as in Section 3.3, we obtain

$$\hat{\kappa}(\theta) = \pm\left[\sec\psi\,\cos(\psi+\theta)\right]^{1/2}.$$

Using the substitution $\theta = 2\phi - \psi$, we utilise the solutions from Section 3.3, but redefine some of our parameters so that we now have

$$A = 2\left(\sec\psi\right)^{-1/2}, \quad B = 0, \quad k = \sqrt{2}.$$

The line curvature $\hat{\kappa}(\phi)$ changes sign at the point (X_0, Y_0) corresponding to ϕ_0. We may deduce that $\phi_0 = \pi/4$, by solving $\hat{\kappa}(\phi_0) = 0$, for ϕ_0. The point (X_0, Y_0) has similar coordinates to that in (3.14), and taking the redefined parameters into account, these coordinates are

$$\begin{aligned} X_0 &= \left[\sin\psi\, g_1(\psi/2) - \cos\psi\, g_2(\psi/2)\right], \\ Y_0 &= \frac{h_{\rm rip}}{\alpha} - \left[\sin\psi\, g_2(\psi/2) + \cos\psi\, g_1(\psi/2)\right]. \end{aligned}$$

Similarly, with the rotational symmetry of the solutions about the point (X_0, Y_0), and the variation of ϕ over $[\psi/2, \pi/4]$, the curves C_1 and C_2 can still be written as

$$\begin{aligned} X_{C_1/C_2}(\phi) &= X_0 \pm \left[\cos\psi\, g_2(\phi) - \sin\psi\, g_1(\phi)\right], \\ Y_{C_1/C_2}(\phi) &= Y_0 \pm \left[\sin\psi\, g_2(\phi) + \cos\psi\, g_1(\phi)\right]. \end{aligned}$$

Using the same derivation as in Section 3.3, the Y–component of the critical point in this case may be written as

$$Y_0 = \frac{h_{\rm rip} + \delta_{\rm gs}}{2\alpha}.$$

As before, multiplying the solutions above by the scaling factor $\alpha = \sqrt{\gamma/\epsilon_{\rm gs}}$ recovers the dimensional solutions for the curves C_1 and C_2.

3.4.2 Numerical results

In this particular case, there is only one parameter to be determined, namely ψ. The value of ψ is determined numerically using the boundary condition $y_{C_2}(\psi/2) = \delta_{\rm gs}$. After computing ψ, the solution is fully determined and representative plots are shown in Fig. 3.4. We comment here that the side of the ripple for $\gamma = 0.8$ in the neighbourhood of the critical point becomes vertical when the ripple amplitude $h_{\rm rip} \approx 8.0\,\delta_{\rm gs}$ for the Cu(111) substrate, and $h_{\rm rip} \approx 6.7\,\delta_{\rm gs}$ for the Ni(111) substrate while $\delta_{\rm gs}$ takes a specific empirical value for each substrate as presented in Table 3.1. Increasing the ripple height causes the graphene sheet to start bending over itself, which is the transition point from the rippled state to the wrinkled state. Furthermore, higher bending rigidities require higher ripple amplitudes for the side of the ripple to become vertical. However, we adopt a particular value of $h_{\rm rip}$ for each substrate material in all plots to enable comparison between various values of the bending rigidity γ.

The total half arc length of the ripple $L_{\rm rip}$ and the total energy $E_{\rm tot}$ for this case can be calculated from (3.15) and (3.16), respectively, with the new parameters $\mu = 0$ and $\phi_0 = \pi/4$. Thus, the total half arc length of the ripple is given by

$$L_{\rm rip} = \frac{4}{\rho}\sqrt{\gamma/\epsilon_{\rm gs}}\Big[F(\pi/4, k) - F(\psi/2, k)\Big],$$

and the total energy per unit length is given by

$$E_{\rm tot} = 4\rho\sqrt{\gamma\epsilon_{\rm gs}}\,[E(\pi/4, k) - E(\psi/2, k)] - \epsilon_{\rm gs}\,(x_2 - x_1)\,.$$

Numerical values for the x–component of the critical point (x_0, y_0) and the

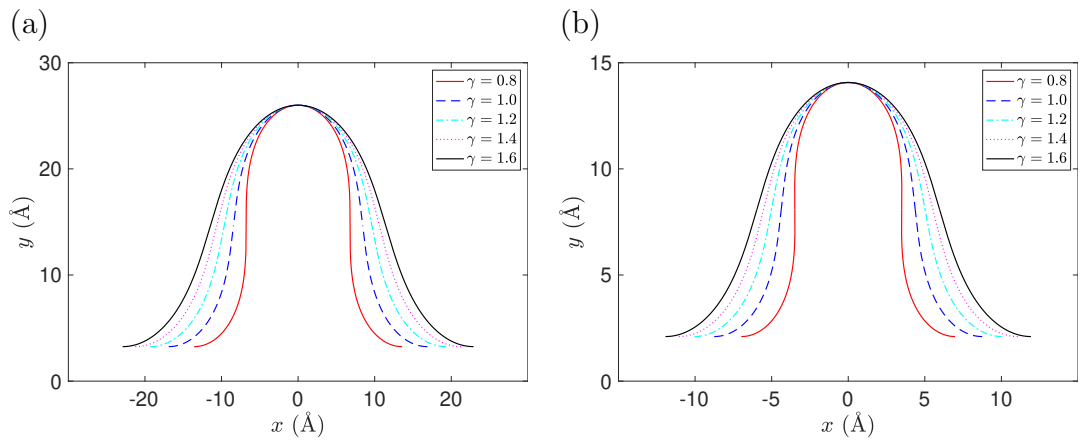

Figure 3.4: Rippled graphene sheet located on: (a) Cu(111) substrate and (b) Ni(111) substrate for various values of γ, in the substrate constrained case. The substrate surface is set to be at the horizontal axis.

total half arc length of the ripple are shown in Table 3.3, for a range of values for the bending rigidity γ. Again the vdW interaction strength ϵ_{gs} takes a specific empirically derived value for each substrate as given in Table 3.1.

Table 3.3: The x–component of the critical point and the ripple half arc length L_{rip} for various bending rigidities γ, in the substrate constrained case.

γ (eV)	Cu(111) substrate		Ni(111) substrate	
	x_0 (Å)	L_{rip} (Å)	x_0 (Å)	L_{rip} (Å)
0.8	6.79	29.81	3.49	15.63
1.0	8.44	31.13	4.37	16.32
1.2	9.65	32.34	5.02	16.95
1.4	10.63	33.43	5.53	17.52
1.6	11.45	34.44	5.97	18.04

3.5 The graphene constrained case

3.5.1 Analytical solutions

We now consider a second particular case being the graphene constrained case, as shown in Fig. 3.2(c). In addition to the assumed isoperimetric constraint on the total arc length of C, the variations of x_2 are also taken into account in this case. We assume that x_2 varies proportionally with x_1, that is

$$x_2 - x_1 = L_{\text{tot}} - \int_{C_1+C_2} \mathrm{d}s = L_{\text{tot}} - \int_{C_1+C_2} \left(1 + \dot{y}^2\right)^{1/2} \mathrm{d}x \,.$$

In terms of the nondimensional variables, this relationship yields

$$X_2 - X_1 = L_{\text{tot}}/\alpha - \int_{C_1+C_2} \left(1 + Y'^2\right)^{1/2} \mathrm{d}X \,. \tag{3.18}$$

Repeating the same nondimensionalisation steps taken in Section 3.3, the total energy per unit length for this case is

$$\hat{E}_{\text{tot}} = \int_{C_1+C_2} \left[\frac{\gamma}{\alpha} \frac{Y''^2}{\left(1 + Y'^2\right)^{5/2}} + \lambda\alpha \left(1 + Y'^2\right)^{1/2} \right] \mathrm{d}X + \alpha(\lambda - \epsilon_{\text{gs}})(X_2 - X_1),$$

which after using the relationship in (3.18) is reduced to

$$\hat{E}_{\text{tot}} = \int_{C_1+C_2} \left[\frac{\gamma}{\alpha} \frac{Y''^2}{\left(1 + Y'^2\right)^{5/2}} + \epsilon_{\text{gs}}\alpha \left(1 + Y'^2\right)^{1/2} \right] \mathrm{d}X + \alpha \left(\lambda - \epsilon_{\text{gs}}\right) \left(L/\alpha\right).$$

We now divide both sides by $\epsilon_{\text{gs}}\alpha$ and set $\alpha = \sqrt{\gamma/\epsilon_{\text{gs}}}$. Further, the aim is to determine the shape of $Y = Y(X)$ which minimises $\hat{E}_{\text{tot}}$, and here λ has no impact on the solution, so $\lambda = \epsilon_{\text{gs}}$ is chosen to simplify the calculation. The final form of the energy functional to be minimised is

$$\hat{E}_{\text{tot}} = \int_{C_1+C_2} \left[\frac{Y''^2}{\left(1 + Y'^2\right)^{5/2}} + \left(1 + Y'^2\right)^{1/2} \right] \mathrm{d}X \,, \tag{3.19}$$

subject to the boundary conditions provided in Section 3.2. Comparing (3.19) and (3.5), we find that $\mu = 1$. In a similar way as in the previous two cases, the use of calculus of variations then yields

$$\hat{\kappa}(\theta) = \pm \left[1 - \beta \sin\theta\right]^{1/2}. \tag{3.20}$$

Similarly, by comparing (3.20) with the equivalent expression for the transitional case (3.10), we note that (3.20) is a special case where $\psi = \pi/2$ and β acts in place of the term $(1-\mu)\sec\psi = \sqrt{(1-\mu)^2 + \beta^2}$ as μ approaches 1. Therefore, we use the substitution $\theta = 2\phi - \pi/2$ in (3.20) and consequently redefine the parameters A, B, and k in (3.13) for this case such that

$$A = \frac{2(1+\beta)^{1/2}}{\beta}, \quad B = \frac{1}{1+\beta}, \quad \text{and} \quad k = \left(\frac{2\beta}{1+\beta}\right)^{1/2}.$$

The critical point (X_0, Y_0) represents the point of the rotational symmetry which again corresponds to $\phi_0 = \sin^{-1}(1/k)$, and the coordinates of this point are given by

$$X_0 = g_1(\pi/4), \quad Y_0 = \frac{h_{\text{rip}}}{\alpha} - g_2(\pi/4).$$

Similarly, the solutions on the curves C_1 and C_2 where $\phi \in [\phi_0, \pi/4]$ are

$$X_{C_1/C_2}(\phi) = X_0 \mp g_1(\phi), \quad Y_{C_1/C_2}(\phi) = Y_0 \pm g_2(\phi).$$

The boundary condition $Y_{C_2}(\pi/4) = \delta_{\text{gs}}/\alpha$, is again used to rewrite the Y–component of the critical point as

$$Y_0 = \frac{h_{\text{rip}} + \delta_{\text{gs}}}{2\alpha}.$$

The dimensional solutions for the curves C_1 and C_2 may be obtained by scaling these solutions by $\alpha = \sqrt{\gamma/\epsilon_{\text{gs}}}$.

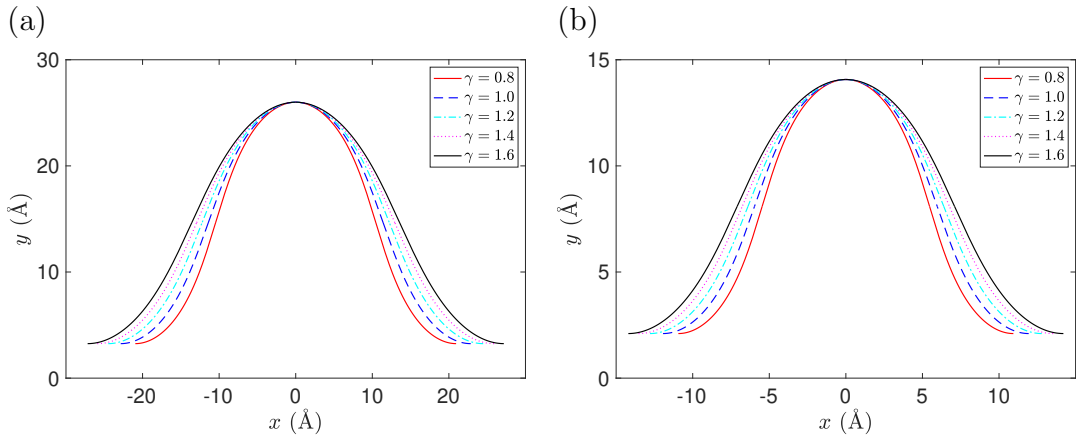

Figure 3.5: Rippled graphene sheet located on: (a) Cu(111) substrate and (b) Ni(111) substrate for various values of γ, in the graphene constrained case. The substrate surface is set to be at the horizontal axis.

3.5.2 Numerical results

In this case, we are left with only one parameter to determine, namely β. The value of β is determined numerically using the boundary condition $y_{C_2}(\pi/4) = \delta_{\rm gs}$. After finding β, the solution is fully determined and representative plots are shown in Fig. 3.5. The total half arc length of the ripple $L_{\rm rip}$ for this case can be evaluated from (3.15) with $\psi = \pi/2$ and $\rho = \sqrt{1+\beta}$ to give

$$L_{\rm rip} = \frac{4}{\rho}\sqrt{\gamma/\epsilon_{\rm gs}}\Big[F(\phi_0, k) - F(\pi/4, k)\Big].$$

Similarly, the total energy per unit length $E_{\rm tot}$ for this case is obtained from (3.16), which yields

$$E_{\rm tot} = 4\rho\sqrt{\gamma\epsilon_{\rm gs}}\big[E(\phi_0, k) - E(\pi/4, k)\big] - \epsilon_{\rm gs}\,(x_2 - x_1)\,.$$

Numerical values for the x–component of the critical point (x_0, y_0) and the total half arc length of the ripple $L_{\rm rip}$ are presented in Table 3.4 for a range

of values of the bending rigidity γ. As before, the vdW interaction ϵ_{gs} takes a specific empirically derived value for each substrate as given in Table 3.1.

3.6 Results

We firstly comment that this model is largely governed by the characteristic parameter μ, which is the ratio of the Lagrange multiplier λ, to the graphene–substrate vdW interaction coefficient ϵ_{gs}. The model is generally represented by the transitional case, but two degenerate cases are also considered according to the characteristic parameter μ. In the absence of an isoperimetric constraint on the graphene sheet, we have the substrate constrained case considered where $\mu = 0$. Where an isoperimetric constraint is imposed on the graphene sheet, along with the presumption $\lambda = \epsilon_{\text{gs}}$, we have the graphene constrained case considered where $\mu = 1$. Fig. 3.6 shows a smooth transition between the three considered cases in this model depending on the value of the characteristic parameter μ and a bending rigidity $\gamma = 1.6\,\text{eV}$.

Table 3.4: The x–component of the critical point and the ripple half arc length L_{rip} for various bending rigidities γ, in the graphene constrained case.

γ (eV)	Cu(111) substrate		Ni(111) substrate	
	x_0 (Å)	L_{rip} (Å)	x_0 (Å)	L_{rip} (Å)
0.80	10.47	32.76	5.47	17.18
1.00	11.43	34.00	5.97	17.83
1.20	12.24	35.11	6.39	18.41
1.40	12.95	36.11	6.77	18.93
1.60	13.59	37.02	7.10	19.41

For the purpose of comparison, a fixed total length $L_{\text{tot}} = 700\,\text{Å}$ is assumed for the rippled graphene sheet on a flat substrate. The goal here is to obtain a relationship between the variation of the substrate half length L_{sub} and the total energy per unit length for the rippled graphene E_{tot}. We incorporate all three cases so that the substrate constrained case is applied when $L_{\text{sub}} < x_2$, the transitional case is applied when $L_{\text{sub}} = x_2$, and the graphene constrained case is applied when $L_{\text{sub}} > x_2$. The point x_2 represents the location where the graphene edge ends, and can be independently calculated for each case using $x_2 = x_1 + L_{\text{tot}} - L_{\text{rip}}$. For example, we use x_{2s} to denote the location where the graphene edge ends in the substrate constrained case. We comment that $x_{2s} < x_{2g}$ where x_{2g} corresponds to the graphene constrained case, while x_{2t} can be found in the range $[x_{2s}, x_{2g}]$ depending on the value we prescribe L_{rip} in the transitional case.

Fig. 3.7 presents a continuous relationship between varying the substrate half length and the total energy per unit length utilising the three cases. The substrate constrained case is formulated to describe the regime where $L_{\text{sub}} < x_{2s}$, provided that, as L_{sub} gets closer to x_{2s}, the total energy per unit length E_{tot} decreases due to the vdW interactions that occur when L_{sub} increases. The graphene constrained case can be adapted to address the regime when $L_{\text{sub}} > x_{2g}$, and in this case the total energy per unit length E_{tot} remains constant since there are no more interactions that are involved for this section. Finally, the transitional case is used to evaluate the total energy per unit length E_{tot} when $L_{\text{sub}} \approx x_2$. Multiple values for x_{2t} were chosen from the interval $[x_{2s}, x_{2g}]$ to fill the gap between the substrate constrained case and the graphene constrained case where x_{2t} denotes the location of the graphene edge in the transitional case.

A graphene sheet of a total half length $L_{\text{tot}} = 700\,\text{Å}$ remains flat when it is

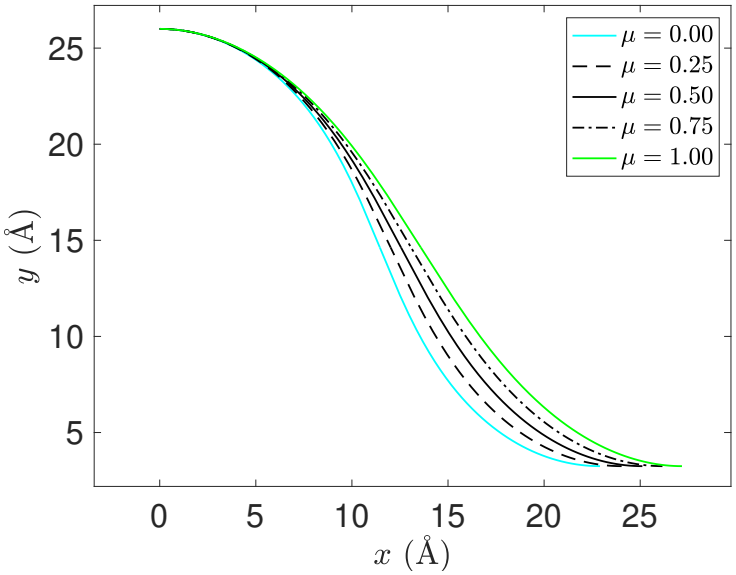

Figure 3.6: Various conformations for the right-half of a graphene ripple using the substrate constrained case ($\mu = 0$), the transitional case ($\mu = 0.25, 0.50, 0.75$), and the graphene constrained case ($\mu = 1$).

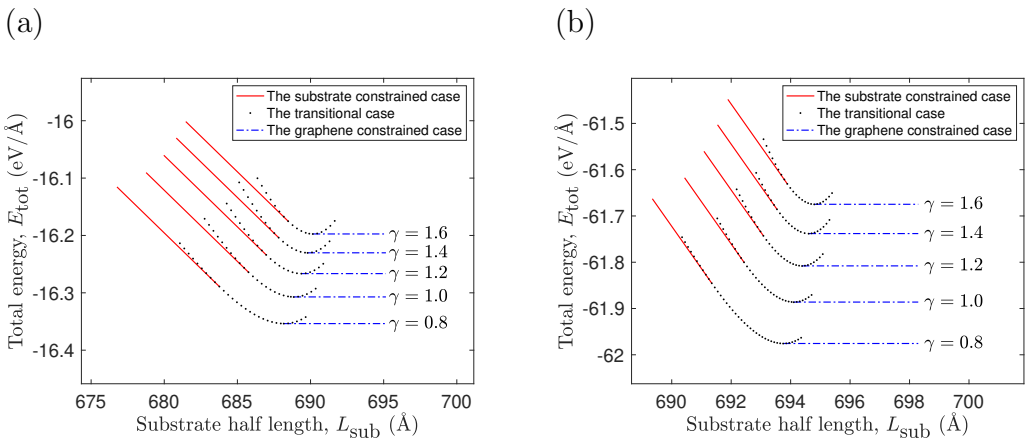

Figure 3.7: The relationship between varying the substrate length of: (a) Cu(111) substrate, (b) Ni(111) substrate and the total energy per unit length.

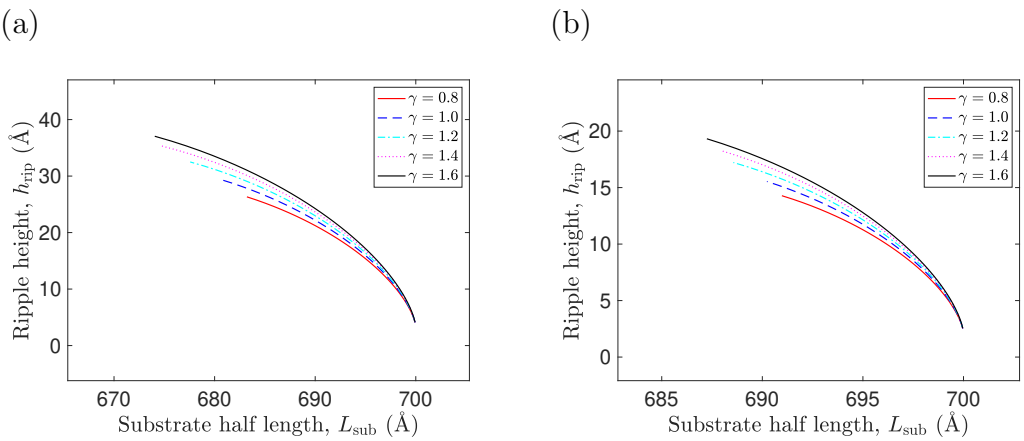

Figure 3.8: The relationship between reducing the substrate length of: (a) Cu(111) substrate, (b) Ni(111) substrate and the ripple amplitude.

placed on a flat substrate of the same half length. The substrate constrained case can be adapted to investigate the impact of reducing the substrate length on the conformation of the graphene sheet. Fig. 3.8 shows that ripples form in this scenario, and that there is an increase in the ripple amplitude as the substrate length decreases. Graphene of lower bending rigidity reaches the ripple height for which the side of the ripple becomes vertical at a relatively longer substrate than graphene with a higher bending rigidity. The substrate length at which the side of the ripple becomes vertical corresponds to the left endpoint of each curve in Fig. 3.8.

The impact of reducing the substrate length on the total energy per unit length is presented in Fig. 3.9. The elastic energy vanishes when the graphene sheet is flat; and consequently, reduces (3.1) to $E_{\text{tot}} = -\epsilon_{\text{gs}}\,(x_2 - x_1)$. Thus, the total energy per unit length for a flat graphene sheet of a total half length $L_{\text{tot}} = 700\,\text{Å}$ is approximately $-17.2\,\text{eV}\,\text{Å}^{-1}$ when it is placed on copper, and $-63.5\,\text{eV}\,\text{Å}^{-1}$ in the case of a nickel substrate. It increases when the substrate length decreases, as expected due to reduced vdW interactions between the

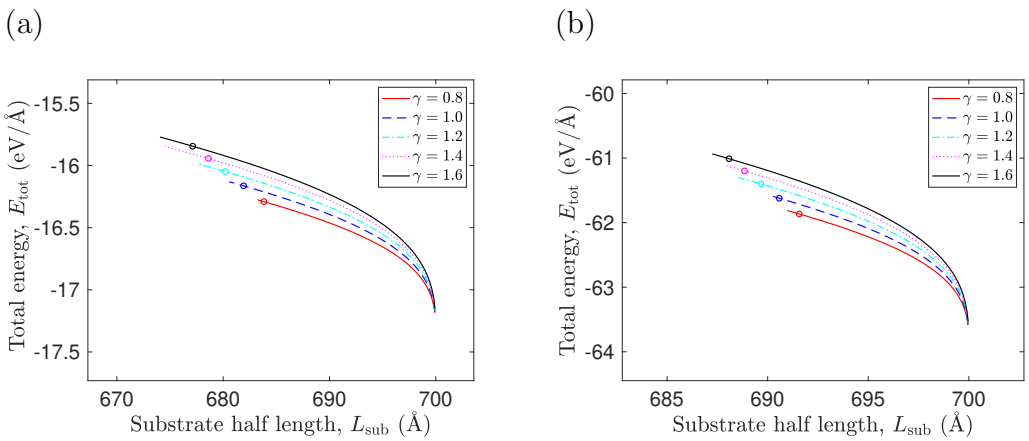

Figure 3.9: The relationship between reducing the substrate length of: (a) Cu(111) substrate, (b) Ni(111) substrate and the total energy per unit length.

graphene sheet and the substrate, as well as the elastic energy stored in the ripple. The points marked with circles represent $(L_{\text{sub}_0}, E_{\text{tot}}(L_{\text{sub}_0}))$ where L_{sub_0} denotes the substrate half length when the gradient of the total energy per unit length curve approaches $-\epsilon_{\text{gs}}$.

Starting from a flat graphene sheet lying on a shrinking substrate, the system might form a ripple or remain flat and begin to overhang the substrate. The ripple formation pathway follows the transitional case and the flat pathway follows the substrate constrained case. In an ideal setting, ripples would not form because the energy required to follow the first pathway exceeds the energy lost in following the second. However, we comment that many experimental situations include confounding effects such as impurities and defects in the graphene structure, which are not accounted for in this model.

Recently, morphologies of graphene wrinkles on a copper substrate were experimentally investigated by Wang et al. [6]. They observed unexpected profiles of wrinkles with widths in the range of tens of nanometres, and

heights in the range of a few nanometres. Their theoretical methods and MD simulations agree that the expected maximum width of wrinkles is less than 2.7 nm, which is significantly smaller than those experimentally observed. As they reported, the presence of interlayer molecules between the graphene and the copper substrate is the main mechanism that enlarges both the width and height of the wrinkled graphene. Since interlayer molecules are not taken into account in this study, the model developed here is comparable with their MD simulations without interlayer molecules. Their MD simulation model, as reprinted in Fig. 3.10(a)-(b), is a stack of two rectangular materials, upper cyan graphene and lower red copper which is best modelled by the transitional case in our model. Therefore, the conformations of rippled (or wrinkled) graphene on a copper substrate, obtained by the transitional case, with bending rigidity $\gamma = 1.2\,\mathrm{eV}$ and different heights are adopted to compare with the results of MD simulations of graphene wrinkles obtained by Wang et al. [6], as shown in Fig. 3.10(c). Despite the fact that the present model uses the value of $2.481\,\mathrm{eV\,nm^{-2}}$ for the vdW energy of graphene–Cu(111) interactions per unit length, but their model used the value of $4.494\,\mathrm{eV\,nm^{-2}}$, both results are in excellent agreement in predicting the profiles of graphene ripples (or wrinkles). Finally, we comment that the value of the graphene–Cu(111) vdW interactions energy indicates how strongly graphene binds to Cu(111); and hence, their value means that graphene binds to Cu(111) more strongly compared to our value. Therefore, the use of their value in our model would affect the predicted profiles, leading to thinner ripples with slightly lower heights.

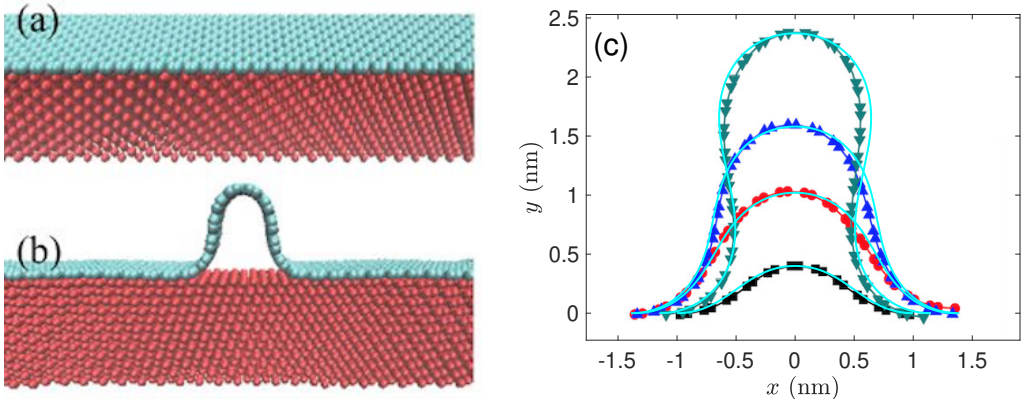

Figure 3.10: MD simulation models and results of graphene wrinkles reprinted (or adapted) from Ref. [6] licensed under a Creative Commons Attribution 4.0 International License. (a)-(b) The MD simulation model, performed by Wang et al. [6], is presented here in order to adopt the appropriate case among those developed in this model for comparison purposes. (c) The profiles of graphene ripples or wrinkles obtained by the present model (cyan lines) superimposed upon the results of MD simulation.

3.7 Conclusion

In this chapter, we utilise the calculus of variations to develop a mathematical model for a rippled graphene sheet that is located on a flat metal substrate. A translational symmetry is assumed along the ripple, which reduces the problem to a 2D problem. Furthermore, the reflective symmetry of the ripple about the y–axis allows consideration of solutions in the upper–right quadrant only. Variational calculus is employed to minimise the elastic energy arising from the curvature squared and to maximise the vdW interaction energy between the flat section of the graphene and the metal substrate.

We account for the length of the substrate by considering three distinct cases for a rippled graphene sheet on a substrate. The transitional case

addresses the case in which the edges of the rippled graphene sheet and the substrate coincide. The substrate constrained case occurs when the edge of the graphene sheet overhangs the substrate edge. The graphene constrained case applies to a rippled graphene sheet for which the edge of the sheet does not extend to the substrate edge. Analytical solutions are derived for the three cases and a smooth transition between the three cases is precisely determined.

We assume a fixed half length of the graphene sheet, and consider all three cases to obtain a continuous relationship between the total energy per unit length of the graphene and the length of the substrate as shown in Fig. 3.7. The substrate constrained case is used to illustrate the effect of reducing the substrate length on the ripple height and the total energy of the graphene, as shown in Fig. 3.8 and Fig. 3.9. Using the transitional case, the model developed here is shown to agree with the results of earlier MD simulations of graphene ripples (or wrinkles) on a Cu(111) substrate. Finally, we comment that this model is specialised for graphene ripples, but there are other graphene configurations that may form when ripples reach their maximum heights including graphene arch-shaped and self-adhered wrinkles, as discussed in Section 1.3. These graphene wrinkles have previously been considered by Cox et al. [87] in a mathematical model utilising a similar variational approach.

3.8 Nomenclature

Symbol	Description
$\dot{\square}$	derivatives of $\square$ with respect to the dimensional x
$\square'$	derivatives of $\square$ with respect to the nondimensional X
C	the right half part of the ripple
C_1/C_2	the negative/positive curvature regions of the curve C
C_3	the zero curvature region of the curve C
(x_0, y_0)	the point where curvature changes sign
h_{rip}	the height or amplitude of the ripple
δ_{gs}	the graphene–substrate equilibrium distance
E_{e}	the graphene elastic energy
κ	the line curvature
s	the arc length of a curve
γ	the bending rigidity of graphene
E_{v}	the vdW interaction energy
$u(x)$	a Heaviside unit step function
ϵ_{gs}	the graphene–substrate vdW interaction energy per unit length
E_{tot}	the total energy
L_{tot}	the total arc length of C, or total half arc length of the graphene sheet
λ	a Lagrange multiplier
α	a scaling factor
μ	a parameter depending on ϵ_{gs} and λ
$\hat{\square}$	the nondimensional expression of $\square$
F	the integrand part of a functional
$F_{\square}$	the partial derivative of F with respect to the variable $\square$
β	a constant of integration

H	the Hamiltonian energy function
δ	the variation of a functional or variable
ψ	a parameter depending on μ and β
g_1, g_2	functions from which the solution curves are constructed
A, B	parameters used for simplification purposes
ρ	a parameter involving ψ and μ
X_{C_i}/Y_{C_i}	the nondimensional parametric solution for the curve C_i
x_{C_i}/y_{C_i}	the dimensional parametric solution for the curve C_i
L_{rip}	the total half arc length of the ripple
L_{sub}	the substrate half length
L_{sub_0}	the substrate half length when the energy close to $-\epsilon_{\text{gs}}$

Chapter 4

Multi-layer graphene folds on a substrate

4.1 Introduction

Section 1.5 discusses three approaches that have been used for modelling the fold of single-layer graphene, namely the small-deformation model, the finite-deformation model, and the variational model. Aside from the variational model, these approaches have previously been extended to model the fold of multi-layer graphene [56, 57]. This chapter extends the variational approach to model the folding conformation of multi-layer graphene supported by a substrate. We validate the proposed model with a comparison to experimentally observed folding profiles of supported multi-layer graphene. Then in the following chapter, the model is modified to study the folding behaviour of unsupported multi-layer graphene and investigate the effective bending rigidity.

The folding conformation of multi-layer graphene sheets may be substantially influenced by various factors including (among others) the number of

layers and the vdW interaction energy. Lopez-Bezanilla et al. [58] outline several differences in the folding profiles, depending on the number of graphene layers. Therefore, we take these differences into account by calculating the total curvature for a number of lines, each denoting an individual graphene layer. We comment that earlier models have neglected some curvature effects for reasons of simplification. Consequently, their related model of a folded single-layer graphene is generalised through multiplying the bending rigidity by the number of layers [57]. In this chapter, we derive analytical expressions for the total curvature for different numbers of layers using Taylor series expansions. Thereafter, we examine the folding conformation under three different approximations for the total curvature through a comparison with experimental measurements.

In addition to the considerations of the previous paragraph, the vdW interactions between neighbouring graphene sheets, and between each graphene sheet and the substrate when they are supported, are expected to affect the folding mechanics of multi-layer graphene sheets. The effects of vdW interactions have not previously been incorporated into a mathematical model, partly due to limited experimental studies reported in the literature. When modelling the fold of unsupported multi-layer graphene, Meng et al. [57] approximate the strength of vdW interaction between N layers of graphene as 1.125 of that between two graphene layers. However, the LJ potential is employed in this work to model the strengths of the vdW interaction energy for different numbers of layers independently. Furthermore, we account for the change in the equilibrium distances as the number of layers change.

In this chapter, we propose a mathematical model for the fold of multi-layer graphene located on a substrate. In the following section, the general mathematical model is formulated and the total squared curvatures is approx-

imated using a Taylor series expansion. In Section 4.3, the model is nondimensionalised and variational calculus methods are applied to derive three expressions for the line curvature, each under a different approximation. Following this, the general parametric solution is presented in Section 4.4. Then in Section 4.5, specific substrate materials are prescribed, and values for the vdW interaction energy between the substrate and graphene are obtained. In Section 4.6, our results are presented, illustrated by figures and numerical tables, and a comparison is made with theoretical and experimental studies. A brief summary is given in the final section of this chapter.

4.2 Model formulation

We now propose a general formulation to model the folding conformation of multi-layer graphene sheets supported on a substrate. The model is constructed based upon the mid-line of a multi-layer graphene stack. The mid-line coincides with a physical graphene layer when the total number of layers is odd ($N = 2n+1$), or represents a notional layer when the total number of layers is even ($N = 2n$) for some positive integer n. As an example, Fig. 4.1 shows the geometry of a folded 3–layer graphene stack located on a substrate. Furthermore, a 2D problem is considered sufficient due to the assumed translational symmetry in the direction of the fold. The solid curve in Fig. 4.1 represents the mid-line of the fold which consists of a curved region of length L_{fold} and an upper flat region of length $L_{\text{flat}} = x_3 - x_2$.

The mid-line is also partitioned into three parts according to the sign of the line curvature and line gradient. The first part is denoted by C_1 which connects the point (x_0, y_0) to the point (x_1, y_1) with a strictly negative curvature. The second part, C_2, connects the point (x_1, y_1) to the point

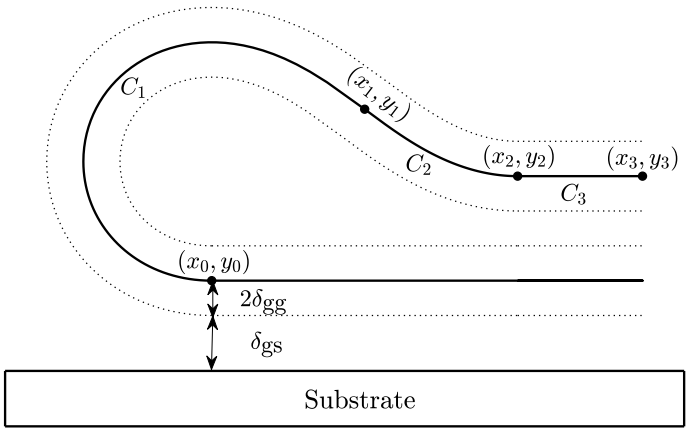

Figure 4.1: Schematic showing the geometry of folded 3–layer graphene sheets supported on a substrate.

(x_2, y_2) where the line curvature here is strictly positive. The horizontal straight line C_3 from the point (x_2, y_2) to the point (x_3, y_3) has zero curvature. Also we use C to denote the concatenation of these three curves C_1, C_2, and C_3.

The radius of curvature of the mid-line is denoted by $R_{\mathrm{m}} = |1/\kappa_{\mathrm{m}}|$, with κ_{m} denotes the associated line curvature given by

$$\kappa_{\mathrm{m}}(s) = \frac{\mathrm{d}x}{\mathrm{d}s}\frac{\mathrm{d}^2y}{\mathrm{d}s^2} - \frac{\mathrm{d}^2x}{\mathrm{d}s^2}\frac{\mathrm{d}y}{\mathrm{d}s},$$

where the mid-line curve is parametrised using the natural parameter s. We assume that the layers maintain an equal distance $2\delta_{\mathrm{gg}}$ from one another, taking into account the decrease in δ_{gg} as the number of layers increases (values of δ_{gg} are calculated in Section 4.5 for different values of N). Hence, the radius of curvature of the j^{th} outer/inner curve is given by

$$R_{j,\mathrm{o/i}} = R_{\mathrm{m}} \pm \nu\delta_{\mathrm{gg}},$$

where $j \in \{1, \ldots, n\}$, while $\nu = 2j$ when N is odd, and $\nu = 2j - 1$ when N is even. Consequently, the corresponding j^{th} outer/inner line curvature is given by

$$\kappa_{j,\text{o/i}} = \frac{|\kappa_\text{m}|}{1 \pm \nu\delta_\text{gg}\,|\kappa_\text{m}|}.$$

We comment that throughout this chapter, δ_gg is used to denote the half spacing distance between any two closest graphene layers, and δ_gs is used to denote the spacing distance from the substrate to the first (closest) graphene layer.

The dominant energies here are the same as those considered when modelling the fold of a single-layer graphene sheet, namely the elastic bending energy and the vdW interaction energy [3]. Moreover, we model the elastic energy E_e by integrating the sum of the squared curvature of each graphene layer over the total length of the curve C multiplied by its bending rigidity. In this study, all graphene layers are assumed to have the same bending rigidity. Thus, the elastic energy may be expressed as

$$E_\text{e} = \int_C \gamma\kappa_\text{tot}^2\,\mathrm{d}s\,,$$

where γ is the bending rigidity of the multi-layer graphene stack, s is the arc length, and κ_tot^2 is the total squared curvatures given by

$$\kappa_\text{tot}^2 = \begin{cases} \displaystyle\sum_{j=1}^{n} \left(\kappa_{j,\text{i}}^2 + \kappa_{j,\text{o}}^2\right) + \kappa_\text{m}^2, & \text{where } N = 2n+1, \text{ is odd,} \\ \displaystyle\sum_{j=1}^{n} \left(\kappa_{j,\text{i}}^2 + \kappa_{j,\text{o}}^2\right), & \text{where } N = 2n, \text{ is even.} \end{cases} \tag{4.1}$$

Generally, for each pair of inner and outer curves a distance $\nu\delta_\text{gg}$ away from the mid-line, their squared curvatures may be combined to simplify (4.1). Thus, we may write

$$\kappa_\text{i}^2 + \kappa_\text{o}^2 = \frac{\kappa_\text{m}^2}{\left(1 - \nu\delta_\text{gg}\,|\kappa_\text{m}|\right)^2} + \frac{\kappa_\text{m}^2}{\left(1 + \nu\delta_\text{gg}\,|\kappa_\text{m}|\right)^2} = \frac{2\kappa_\text{m}^2\left[1 + \left(\nu\delta_\text{gg}\kappa_\text{m}\right)^2\right]}{\left[1 - \left(\nu\delta_\text{gg}\kappa_\text{m}\right)^2\right]^2}, \tag{4.2}$$

and using the Taylor series expansion for the term $[1-(\nu\delta_{\rm gg}\kappa_{\rm m})^2]^{-2}$ in (4.2), we deduce

$$\kappa_{\rm i}^2+\kappa_{\rm o}^2 \approx 2\kappa_{\rm m}^2+6\,\nu^2\delta_{\rm gg}^2\kappa_{\rm m}^4+10\,\nu^4\delta_{\rm gg}^4\kappa_{\rm m}^6, \tag{4.3}$$

for small $\nu\delta_{\rm gg}\kappa_{\rm m}$. Hence, equation (4.1) may be expressed in terms of $\kappa_{\rm m}$, the line curvature of the mid-line, as

$$\kappa_{\rm tot}^2 \approx\ N\kappa_{\rm m}^2+6\,a\,\delta_{\rm gg}^2\kappa_{\rm m}^4+10\,b\,\delta_{\rm gg}^4\kappa_{\rm m}^6, \tag{4.4}$$

where

$$a=\begin{cases}\displaystyle\sum_{j=1}^{n}(2j)^2=\frac{2n\,(n+1)\,(2n+1)}{3}, & \text{where } N \text{ odd},\\ \displaystyle\sum_{j=1}^{n}(2j-1)^2=\frac{n\,(4n^2-1)}{3}, & \text{where } N \text{ even},\end{cases}$$

and

$$b=\begin{cases}\displaystyle\sum_{j=1}^{n}(2j)^4=\frac{8n\,(n+1)\,(2n+1)\,(3n^2+3n-1)}{15}, & \text{where } N \text{ odd},\\ \displaystyle\sum_{j=1}^{n}(2j-1)^4=\frac{n\,(2n+1)\,(24n^3-12n^2-14n+7)}{15}, & \text{where } N \text{ even}.\end{cases}$$

For either odd or even N, we deduce that

$$a=\frac{N\,(N^2-1)}{6}, \quad \text{and} \quad b=\frac{N\,(N^2-1)\,(3N^2-7)}{30}.$$

Therefore, we rewrite (4.4) as

$$\kappa_{\rm tot}^2 \approx N\kappa_{\rm m}^2+N\left(N^2-1\right)\delta_{\rm gg}^2\kappa_{\rm m}^4+N\left(N^2-1\right)\left(N^2-7/3\right)\delta_{\rm gg}^4\kappa_{\rm m}^6, \tag{4.5}$$

which yields the basis for an approximation of the total squared curvatures $\kappa_{\rm tot}^2$.

The vdW interaction energy between graphene and the substrate is modelled using a Heaviside unit step function $u(x)$. The vdW interaction is disregarded in the folded region as an assumption of the modelling, but it is

assumed that it makes the dominant contribution to the energy in the flat region. Thus, the vdW interaction energy is modelled as

$$E_{\mathrm{v}} = -\epsilon \int_C u(x - x_2)\, \mathrm{d}s\,,$$

where ϵ is a positive constant that denotes the vdW interaction energy per unit length, and $u(x)$ is a Heaviside unit step function. Noting that only C_1 and C_2 contribute to the elastic energy where $\dot{y} = 0$ and $\mathrm{d}s = \mathrm{d}x$ in C_3, the total energy per unit length is then expressed as

$$E_{\mathrm{tot}} = E_{\mathrm{e}} + E_{\mathrm{v}} = \int_{C_1+C_2} \gamma \kappa_{\mathrm{tot}}^2\, \mathrm{d}s - \epsilon\,(x_3 - x_2)\,. \tag{4.6}$$

Furthermore, an isoperimetric constraint is applied on the total arc length of the curve C, that is given by

$$\int_C \mathrm{d}s = L_{\mathrm{tot}} = L_{\mathrm{fold}} + L_{\mathrm{flat}} = \int_{C_1+C_2} \mathrm{d}s + (x_3 - x_2)\,.$$

Under this length constraint, a Lagrange multiplier λ is introduced into the total energy functional (4.6) which becomes

$$\begin{aligned} E_{\mathrm{tot}} &= \int_{C_1+C_2} \left(\gamma \kappa_{\mathrm{tot}}^2 + \lambda\right) \mathrm{d}s + (\lambda - \epsilon)\,(x_3 - x_2) \\ &= \int_{C_1+C_2} \left(\gamma \kappa_{\mathrm{tot}}^2 + \lambda\right) \mathrm{d}s + (\lambda - \epsilon) \left(L_{\mathrm{tot}} - \int_{C_1+C_2} \mathrm{d}s\right) \\ &= \int_{C_1+C_2} \left(\gamma \kappa_{\mathrm{tot}}^2 + \epsilon\right) \mathrm{d}s + (\lambda - \epsilon)\, L_{\mathrm{tot}}. \end{aligned} \tag{4.7}$$

In the above expression, the Lagrange multiplier λ plays no role in determining the mid-line that minimises the functional E_{tot}. So, the substitution $\lambda = \epsilon$ is made in (4.7); and hence, the functional to be minimised is now of the form

$$E_{\mathrm{tot}} = \int_0^{s_2} \left(\gamma \kappa_{\mathrm{tot}}^2 + \epsilon\right) \mathrm{d}s\,, \tag{4.8}$$

subject to the boundary conditions, at $s = 0$:

$$x = 0, \quad y = y_0, \quad \mathrm{d}x/\mathrm{d}s = -1, \quad \mathrm{d}y/\mathrm{d}s = 0,$$

and at the endpoint $s = s_2$:

$$x = x_2, \quad y = y_2, \quad \mathrm{d}x/\mathrm{d}s = 1, \quad \mathrm{d}y/\mathrm{d}s = 0,$$

where s_2 the arc length at the point (x_2, y_2) while $y_0 = \delta_{\mathrm{gs}} + (N-1)\,\delta_{\mathrm{gg}}$, $y_2 = \delta_{\mathrm{gs}} + (3N-1)\,\delta_{\mathrm{gg}}$, and the value of x_2 is to be determined from a natural boundary condition.

4.3 Variational calculus

Before considering the variation of the functional (4.8), we first nondimensionalise it by introducing a scaling factor α (to be determined later in this section) such that $x = \alpha X$ and $y = \alpha Y$. In terms of the new variables, κ_{m} and $\mathrm{d}s$ are now given by $\kappa_{\mathrm{m}} = \hat{\kappa}_{\mathrm{m}}/\alpha$ and $\mathrm{d}s = \alpha\ \mathrm{d}S$, respectively. Making use of the new variables X and Y, the nondimensionalised energy functional is given by

$$\bar{E}_{\mathrm{tot}} = \frac{\hat{E}_{\mathrm{tot}}}{\epsilon} = \int_0^{S_2} \left(\frac{\gamma}{\epsilon}\hat{\kappa}_{\mathrm{tot}}^2 + 1\right) \mathrm{d}S\,, \tag{4.9}$$

where S_2 is the nondimensional arc length at the point (X_2, Y_2). Throughout this chapter, F is used to denote the integrand in (4.9), that is

$$F(\hat{\kappa}_{\mathrm{tot}}^2) = \frac{\gamma}{\epsilon}\hat{\kappa}_{\mathrm{tot}}^2 + 1. \tag{4.10}$$

The functional (4.9) is a variational problem containing second–order derivatives with two dependent variables X and Y, and one independent variable S. Following the same derivation as in Section 2.1.2, a necessary condition for the functional (4.9) to have an extremal is given by the pair of Euler–Poisson equations

$$F_X - \frac{\mathrm{d}}{\mathrm{d}S}F_{\dot{X}} + \frac{\mathrm{d}^2}{\mathrm{d}S^2}F_{\ddot{X}} = 0, \quad F_Y - \frac{\mathrm{d}}{\mathrm{d}S}F_{\dot{Y}} + \frac{\mathrm{d}^2}{\mathrm{d}S^2}F_{\ddot{Y}} = 0, \tag{4.11}$$

where dots denote differentiation with respect to the nondimensional arc length S. The integrand F is a function of $\hat{\kappa}_{\mathrm{m}}(\dot{X}, \ddot{X}, \dot{Y}, \ddot{Y})$ and has no explicit dependence on X or Y. Thus, on integrating the pair of equations (4.11) with respect to S, we obtain first integrals given by

$$F_{\dot{X}} - \frac{\mathrm{d}}{\mathrm{d}S} F_{\ddot{X}} = \beta_X, \quad F_{\dot{Y}} - \frac{\mathrm{d}}{\mathrm{d}S} F_{\ddot{Y}} = \beta_Y, \tag{4.12}$$

where β_X and β_Y are the integration constants. Since F has no explicit dependence on S, this provides another first integral given by

$$\dot{X}\left(F_{\dot{X}} - \frac{\mathrm{d}}{\mathrm{d}S} F_{\ddot{X}}\right) + \dot{Y}\left(F_{\dot{Y}} - \frac{\mathrm{d}}{\mathrm{d}S} F_{\ddot{Y}}\right) + \ddot{X} F_{\ddot{X}} + \ddot{Y} F_{\ddot{Y}} - F = H,$$

which may be simplified by substituting β_X and β_Y from (4.12) as

$$\beta_X \dot{X} + \beta_Y \dot{Y} + \ddot{X} F_{\ddot{X}} + \ddot{Y} F_{\ddot{Y}} - F = H, \tag{4.13}$$

where H is a constant. With the presence of a natural boundary condition at X_2, we also consider the standard equation for the first variation of $\bar{E}_{\mathrm{tot}}$ given by

$$\begin{aligned}\delta \bar{E}_{\mathrm{tot}} = &\left[\beta_X\, \delta X + \beta_Y\, \delta Y + F_{\ddot{X}}\, \delta \dot{X} + F_{\ddot{Y}}\, \delta \dot{Y} - H\, \delta S\right]_{S=0}^{S_2} \\ &+ \int_0^{S_2} \left[\left(F_X - \frac{\mathrm{d}F_{\dot{X}}}{\mathrm{d}S} + \frac{\mathrm{d}^2 F_{\ddot{X}}}{\mathrm{d}S^2}\right)\delta X + \left(F_Y - \frac{\mathrm{d}F_{\dot{Y}}}{\mathrm{d}S} + \frac{\mathrm{d}^2 F_{\ddot{Y}}}{\mathrm{d}S^2}\right)\delta Y\right] \mathrm{d}S\,,\end{aligned}$$

which is equivalent to the expression derived in Section 2.1.2 and given by (2.34). Since the endpoint of the x–coordinate X_2 is not prescribed, the length S_2 is also not prescribed. Therefore, we require both $\beta_X = 0$ and $H = 0$, due to the natural boundary condition. Thus, equation (4.13) is now reduced to

$$\ddot{X} F_{\ddot{X}} + \ddot{Y} F_{\ddot{Y}} - F = -\beta_Y \dot{Y}. \tag{4.14}$$

In the next three subsections, we prescribe three different quantities for the integrand F based on various approximations of $\hat{\kappa}_{\mathrm{tot}}^2$, and then apply (4.14)

to derive the corresponding expression for $\hat{\kappa}_{\mathrm{m}}$ for each approximation. Then, we derive parametric solutions for each approximation based on the obtained expression for $\hat{\kappa}_{\mathrm{m}}$, and the comparison between these solutions will be made in Section 4.6.

4.3.1 The one-term approximation

In this subsection, the simplest approximation of κ_{tot}^2 is considered by including only the first term of (4.5) into the model. That is

$$\kappa_{\mathrm{tot}}^2 = N\kappa_{\mathrm{m}}^2.$$

Under this approximation, the function F in (4.10) is now given by

$$F(\dot{X},\dot{Y},\ddot{X},\ddot{Y}) = \frac{N\gamma}{\epsilon\alpha^2}\left(\dot{X}\ddot{Y}-\ddot{X}\dot{Y}\right)^2 + 1,$$

which after substituting the scaling factor α by $\sqrt{N\gamma/\epsilon}$ becomes

$$F(\dot{X},\dot{Y},\ddot{X},\ddot{Y}) = \left(\dot{X}\ddot{Y}-\ddot{X}\dot{Y}\right)^2 + 1. \tag{4.15}$$

Upon the substitutions of $F_{\ddot{X}}$, $F_{\ddot{Y}}$, and F from (4.15) into (4.14), we may derive

$$\left(\dot{X}\ddot{Y}-\ddot{X}\dot{Y}\right)^2 = 1-\beta_Y\dot{Y}, \tag{4.16}$$

whereupon we make the change of variables such that

$$\frac{\mathrm{d}}{\mathrm{d}S} = \left(\frac{\mathrm{d}\theta}{\mathrm{d}S}\right)\frac{\mathrm{d}}{\mathrm{d}\theta}, \quad \text{where} \quad \frac{\mathrm{d}S}{\mathrm{d}\theta} = \left(X'^2+Y'^2\right)^{1/2}, \tag{4.17}$$

and where primes denote derivatives with respect to θ, a tangential angle to the curve measured from the positive direction of the x–axis. Therefore, equation (4.16) may be rewritten as

$$\frac{\left(X'Y''-X''Y'\right)^2}{\left(X'^2+Y'^2\right)^3} = 1-\frac{\beta_Y Y'}{\left(X'^2+Y'^2\right)^{1/2}}.$$

We now make the substitutions

$$X' = \frac{\cos\theta}{\hat{\kappa}_{\mathrm{m}}(\theta)}, \quad Y' = \frac{\sin\theta}{\hat{\kappa}_{\mathrm{m}}(\theta)}, \tag{4.18}$$

which lead to an expression relating to the nondimensional curvature given by

$$\hat{\kappa}_{\mathrm{m}}(\theta) = \pm\left(1 - \beta_Y \sin\theta\right)^{1/2}. \tag{4.19}$$

We comment that this expression is identical to (3.20), except that a slightly different derivation is used here and the definition of the scaling factor α in this chapter involves $N\gamma$ rather than γ.

4.3.2 The two-term approximation

In this subsection, an additional term from the Taylor series for κ_{tot}^2 is taken into account with both the first and second terms of (4.5) now included in the model. That is

$$\kappa_{\mathrm{tot}}^2 = N\kappa_{\mathrm{m}}^2 + N\left(N^2-1\right)\delta_{\mathrm{gg}}^2\kappa_{\mathrm{m}}^4.$$

This expression converges to the one-term approximation for $\delta_{\mathrm{gg}}\kappa_{\mathrm{m}} \ll 1$. Following the same steps as in Section 4.3.1, we substitute $\alpha = \sqrt{N\gamma/\epsilon}$ and rewrite the function F in (4.10) as

$$F(\dot{X},\dot{Y},\ddot{X},\ddot{Y}) = \left(\dot{X}\ddot{Y} - \ddot{X}\dot{Y}\right)^2 + \mu\left(\dot{X}\ddot{Y} - \ddot{X}\dot{Y}\right)^4 + 1,$$

with

$$\mu = \left(\frac{\epsilon\delta_{\mathrm{gg}}^2}{N\gamma}\right)\left(N^2-1\right). \tag{4.20}$$

Furthermore, we employ (4.14) to derive the following expression

$$\left(\dot{X}\ddot{Y} - \ddot{X}\dot{Y}\right)^2 + 3\mu\left(\dot{X}\ddot{Y} - \ddot{X}\dot{Y}\right)^4 = 1 - \beta_Y\dot{Y}.$$

We now make the change of variables as in (4.17) to obtain

$$\frac{\left(X'Y''-X''Y'\right)^2}{\left(X'^2+Y'^2\right)^3}+3\mu\,\frac{\left(X'Y''-X''Y'\right)^4}{\left(X'^2+Y'^2\right)^6}=1-\frac{\beta_Y Y'}{\left(X'^2+Y'^2\right)^{1/2}}, \tag{4.21}$$

which may be rearranged to give

$$\hat{\kappa}_{\mathrm{m}}^4(\theta)+\frac{\hat{\kappa}_{\mathrm{m}}^2(\theta)}{3\mu}+\frac{1}{36\mu^2}=\frac{1}{3\mu}\left[1-\frac{\beta_Y Y'}{\left(X'^2+Y'^2\right)^{1/2}}+\frac{1}{12\mu}\right]. \tag{4.22}$$

Solving (4.22) for real valued solutions of $\hat{\kappa}_{\mathrm{m}}(\theta)$ leads to the nondimensional curvature of the mid-line, that is

$$\hat{\kappa}_{\mathrm{m}}(\theta)=\pm\left[\frac{1}{\sqrt{3\mu}}\left(1-\frac{\beta_Y Y'}{\left(X'^2+Y'^2\right)^{1/2}}+\frac{1}{12\mu}\right)^{1/2}-\frac{1}{6\mu}\right]^{1/2},$$

and by making the substitutions (4.18), we deduce that

$$\hat{\kappa}_{\mathrm{m}}(\theta)=\pm\left[\frac{1}{\sqrt{3\mu}}\left(1-\beta_Y\sin\theta+\frac{1}{12\mu}\right)^{1/2}-\frac{1}{6\mu}\right]^{1/2}. \tag{4.23}$$

We mention that the expression (4.23) is obtained after rearranging the fourth degree expression (4.21) and completing square in terms of $\hat{\kappa}_{\mathrm{m}}^2(\theta)$ while neglecting the solution with a negative sign to avoid complex roots.

4.3.3 The three-term approximation

In this subsection, we consider an additional third term in κ_{tot}^2 with all of the explicit terms of (4.5) now included in the model. That is

$$\kappa_{\mathrm{tot}}^2=N\kappa_{\mathrm{m}}^2+N\left(N^2-1\right)\delta_{\mathrm{gg}}^2\kappa_{\mathrm{m}}^4+N\left(N^2-1\right)\left(N^2-7/3\right)\delta_{\mathrm{gg}}^4\kappa_{\mathrm{m}}^6.$$

As before, we note that this expression approaches the two-term and one-term approximations for $\delta_{\mathrm{gg}}\kappa_{\mathrm{m}}\ll 1$. Again, the same expression for α is used, and the function F in (4.10) is now given by

$$F(\dot{X},\dot{Y},\ddot{X},\ddot{Y})=\left(\dot{X}\ddot{Y}-\ddot{X}\dot{Y}\right)^2+\mu\left(\dot{X}\ddot{Y}-\ddot{X}\dot{Y}\right)^4+\rho\left(\dot{X}\ddot{Y}-\ddot{X}\dot{Y}\right)^6+1,$$

where μ is given by (4.20), and

$$\rho = \left(\frac{\epsilon\delta_{\rm gg}^2}{N\gamma}\right)^2 \left(N^2-1\right)\left(N^2-7/3\right).$$

After the substitution of the new integrand F into (4.14), we may derive the following equation

$$\left(\dot{X}\ddot{Y}-\ddot{X}\dot{Y}\right)^2 + 3\mu\left(\dot{X}\ddot{Y}-\ddot{X}\dot{Y}\right)^4 + 5\rho\left(\dot{X}\ddot{Y}-\ddot{X}\dot{Y}\right)^6 = 1-\beta_Y\dot{Y}.$$

Making use of the same change of variables as in the last two subsections we derive

$$\hat{\kappa}_{\rm m}^2(\theta) + 3\mu\,\hat{\kappa}_{\rm m}^4(\theta) + 5\rho\,\hat{\kappa}_{\rm m}^6(\theta) = 1 - \frac{\beta_Y Y'}{(X'^2+Y'^2)^{1/2}}. \tag{4.24}$$

It is now necessary to solve (4.24) for real valued solutions of $\hat{\kappa}_{\rm m}(\theta)$ in order to obtain the relative expression for the line curvature of the mid-line. To simplify the algebra, we use the substitution $\omega = \hat{\kappa}_{\rm m}^2(\theta) + \mu/(5\rho)$, which, after some rearrangement, reduces (4.24) to

$$\omega^3 + p\,\omega + q = 0, \tag{4.25}$$

with

$$p = \frac{5\rho-3\mu^2}{(5\rho)^2}, \quad \text{and} \quad q = \mu\,\frac{2\mu^2-5\rho}{(5\rho)^3} - \frac{1}{5\rho}\left[1-\frac{\beta_Y Y'}{(X'^2+Y'^2)^{1/2}}\right].$$

We now apply Cardano's method, as explained in Section 2.1.4, to solve the cubic equation (4.25). It may be shown numerically that the discriminant $\mathcal{D} = -27q^2 - 4p^3$, is always negative. Hence, there are three distinct roots: two that are complex conjugates, and a third that is the only real root. The real root may be expressed as

$$\omega(\theta) = \left[\sqrt{\frac{q^2}{4}+\frac{p^3}{27}} - \frac{q}{2}\right]^{1/3} - \frac{p}{3}\left[\sqrt{\frac{q^2}{4}+\frac{p^3}{27}} - \frac{q}{2}\right]^{-1/3}.$$

Thus, using the substitution $\hat{\kappa}_{\rm m}^2(\theta) = \omega(\theta) - \mu/(5\rho)$ we deduce that the line curvature $\hat{\kappa}_{\rm m}$ is

$$\hat{\kappa}_{\rm m}(\theta) = \pm\sqrt{\omega(\theta) - \mu/(5\rho)},$$

or equivalently

$$\hat{\kappa}_{\rm m}(\theta) = \pm\left[\left(\sqrt{\frac{q^2}{4}+\frac{p^3}{27}}-\frac{q}{2}\right)^{1/3} - \frac{p}{3}\left(\sqrt{\frac{q^2}{4}+\frac{p^3}{27}}-\frac{q}{2}\right)^{-1/3} - \frac{\mu}{5\rho}\right]^{1/2}, \tag{4.26}$$

where p, μ, and ρ are parameters as defined earlier in this section, but using the substitutions (4.18), q here is a function of θ given by

$$q(\theta) = \mu\,\frac{2\mu^2 - 5\rho}{(5\rho)^3} - \frac{1}{5\rho}\left(1 - \beta_Y \sin\theta\right).$$

4.4 Parametric solution

After determining the expression for the curvature of the mid-line $\hat{\kappa}_{\rm m}(\theta)$ relating to three approximations of $\kappa_{\rm tot}^2$, the two differential equations given in (4.18) are now used to derive parametric solutions of the folded region of the curve C. Analytical solutions, for the one-term approximation, and numerical solutions, for the two-term and three-term approximations, are presented in the next two subsections.

4.4.1 The one-term approximation

The expression of line curvature $\hat{\kappa}_{\rm m}(\theta)$ given by (4.19), has been used in Section 3.5 to obtain an analytical solution for the conformation of a rippled graphene sheet. That solution is written in terms of the key functions $g_1(\phi)$ and $g_2(\phi)$ after using the substitution $\theta = 2\phi - \psi$, as given by (3.13). In this

section, a similar analytical solution is proposed for the folding conformation of a supported multi-layer graphene stack, which also can be written in terms of $g_1(\phi)$ and $g_2(\phi)$ by substituting $\psi = \pi/2$. For consistency and future use, these functions are redefined such that

$$\begin{aligned} g_1(\phi) &= A\left(1 - k^2 \sin^2\phi\right)^{1/2}, \\ g_2(\phi) &= A\left[E(\phi,k) - BF(\phi,k)\right], \end{aligned} \tag{4.27}$$

with the parameters

$$A = \frac{2\left(1+\beta_Y\right)^{1/2}}{\beta_Y}, \quad B = \frac{1}{1+\beta_Y}, \quad k = \left(\frac{2\beta_Y}{1+\beta_Y}\right)^{1/2}. \tag{4.28}$$

For C_1, the part of the solution with negative curvature, the curve ranges between the starting point (X_0, Y_0) at $\theta = \theta_0$ and the point of zero curvature (X_1, Y_1) at $\theta = \theta_1$. We note that $\theta_0 = -\pi$ which implies $\phi_0 = -\pi/4$, and the value of $\phi_1 = \sin^{-1}(1/k)$ is determined by solving $\hat{\kappa}_{\mathrm{m}}(\phi_1) = 0$ for ϕ_1. The solution for C_1 is then given by

$$\begin{aligned} X_{C_1}(\phi) &= g_1(-\pi/4) - g_1(\phi), \\ Y_{C_1}(\phi) &= Y_0 - g_2(-\pi/4) + g_2(\phi), \end{aligned}$$

where $Y_0 = y_0/\alpha$ and $\phi \in [-\pi/4, \phi_1]$.

For C_2, the part of the solution with positive curvature, we require a continuous curve in the transition from C_1 to C_2 at the point (X_1, Y_1) where $\hat{\kappa}_{\mathrm{m}}$ changes sign. To satisfy this constraint, the same derivation as for the curve C_1 is repeated, but the opposite signs of $g_1(\phi)$ and $g_2(\phi)$ are used. The solution for this part is given by

$$\begin{aligned} X_{C_2}(\phi) &= g_1(-\pi/4) + g_1(\phi), \\ Y_{C_2}(\phi) &= Y_0 - g_2(-\pi/4) - g_2(\phi) + 2g_2(\phi_1), \end{aligned}$$

where $\phi \in [\phi_1, \pi/4]$.

4.4.2 The two-term and three-term approximations

Due to the complexity of the expressions of $\hat{\kappa}_{\rm m}(\theta)$ given by (4.23)–(4.26), parametric solutions for the two-term and the three-term approximations are expressed in integral forms and then evaluated numerically. The line curvature $\hat{\kappa}_{\rm m}(\theta)$ changes sign at the point (X_1, Y_1) which corresponds to $\theta = \theta_1$. Thus, we may deduce that $\theta_1 = \sin^{-1}(1/\beta_Y)$ for each approximation by solving $\hat{\kappa}_{\rm m}(\theta_1) = 0$, for θ_1 in (4.23)–(4.26). For C_1, the part of the solution with negative curvature, we have $\theta \in [-\pi, \theta_1]$ and by taking into consideration the boundary conditions at the starting point $\theta_0 = -\pi$, we deduce that

$$X_{C_1}(\theta) = \int_{-\pi}^{\theta} \frac{\cos\tilde{\theta}}{\hat{\kappa}_{\rm m}(\tilde{\theta})}\,{\rm d}\tilde{\theta}\,, \quad Y_{C_1}(\theta) = Y_0 - \int_{-\pi}^{\theta} \frac{\sin\tilde{\theta}}{\hat{\kappa}_{\rm m}(\tilde{\theta})}\,{\rm d}\tilde{\theta}\,.$$

For C_2, the part of the solution with positive curvature, we again require continuity at the point (X_1, Y_1) where $\hat{\kappa}_{\rm m}$ changes sign. To satisfy this constraint, the same steps as for the curve C_1 are followed, but the opposite sign of $\hat{\kappa}_{\rm m}(\theta)$ is chosen. The solution for this part is given by

$$X_{C_2}(\theta) = X_{C_1}(\theta_1) + \int_{\theta}^{\theta_1} \frac{\cos\tilde{\theta}}{\hat{\kappa}_{\rm m}(\tilde{\theta})}\,{\rm d}\tilde{\theta}\,,$$
$$Y_{C_2}(\theta) = Y_{C_1}(\theta_1) - \int_{\theta}^{\theta_1} \frac{\sin\tilde{\theta}}{\hat{\kappa}_{\rm m}(\tilde{\theta})}\,{\rm d}\tilde{\theta}\,,$$

where $\theta \in [0, \theta_1]$.

Furthermore, the solution of the $j^{\rm th}$ outer/inner curve may be obtained using

$$X_{j,{\rm i/o}}(\theta) = X(\theta) \pm \frac{\nu\delta_{\rm gg}}{\alpha}\left(\frac{Y'}{\sqrt{X'^2 + Y'^2}}\right),$$
$$Y_{j,{\rm i/o}}(\theta) = Y(\theta) \mp \frac{\nu\delta_{\rm gg}}{\alpha}\left(\frac{X'}{\sqrt{X'^2 + Y'^2}}\right),$$

where $X(\theta)$ and $\rm Y(\theta)$ represent the parametric solutions of the mid-line, $\delta_{\rm gg}$ is the half spacing distance between adjacent layers, and ν is defined earlier

in Section 4.2. Multiplying these solutions by the scaling factor $\alpha = \sqrt{N\gamma/\epsilon}$ recovers the dimensional solutions for the folded curve of C. To this point, the model behaviour is governed by the material parameters of the graphene and supporting substrate. These are the bending rigidity of the graphene, which we assume is fixed, and the vdW interaction of the graphene and the substrate, which we calculate in the following section.

4.5 Substrate parameters

The existing experimental data reported in the literature on folding multi-layer graphene sheets on SiO_2 [7], provides a good opportunity to validate the accuracy of these approximations. This substrate material has been widely used in the fabrication of graphene-based electrical devices [83]. Based on these considerations, this model is specialised to determine the folding behaviour of multi-layer graphene sheets supported on a SiO_2 substrate.

The LJ potential, described in Section 2.2.1, is now employed to model the vdW interaction strength ϵ. Recall that from (2.49), the interaction between two graphene layers at a distance φ is modelled as

$$\epsilon_{\mathrm{gg}}(\varphi) = D_{\mathrm{g}}^2 \left(-\frac{\pi \mathcal{A}_{\mathrm{gg}}}{2\varphi^4} + \frac{\pi \mathcal{B}_{\mathrm{gg}}}{5\varphi^{10}} \right),$$

where D_{g} denotes the surface density of carbon atoms on a sheet of graphene, while $\mathcal{A}_{\mathrm{gg}}$ and $\mathcal{B}_{\mathrm{gg}}$ are the graphene–graphene attractive and repulsive constants, respectively. From (2.51), the interaction energy between a graphene sheet and a three-dimensional substrate separated by $\tilde{\varphi}$ is modelled as

$$\epsilon_{\mathrm{gs}}(\tilde{\varphi}) = D_{\mathrm{g}} D_{\mathrm{s}} \left(-\frac{\pi \mathcal{A}_{\mathrm{gs}}}{6\tilde{\varphi}^3} + \frac{\pi \mathcal{B}_{\mathrm{gs}}}{45\tilde{\varphi}^9} \right),$$

where D_{s} denotes the volume density of the chemical element of the substrate, while $\mathcal{A}_{\mathrm{gs}}$ and $\mathcal{B}_{\mathrm{gs}}$ denote the graphene–substrate attractive and repulsive

constants, respectively. Since the SiO_2 substrate is prescribed in this section, we must account for the graphene–silicon and graphene–oxygen interactions. Therefore, we model $\epsilon_{\rm gs}(\tilde{\varphi})$ as

$$\begin{aligned}\epsilon_{\rm gs}(\tilde{\varphi}) &= \epsilon_{\rm gSi}(\tilde{\varphi}) + \epsilon_{\rm gO}(\tilde{\varphi}) \\ &= D_{\rm g}\left[D_{\rm Si}\left(-\frac{\pi\mathcal{A}_{\rm gSi}}{6\tilde{\varphi}^3}+\frac{\pi\mathcal{B}_{\rm gSi}}{45\tilde{\varphi}^9}\right)+D_{\rm O}\left(-\frac{\pi\mathcal{A}_{\rm gO}}{6\tilde{\varphi}^3}+\frac{\pi\mathcal{B}_{\rm gO}}{45\tilde{\varphi}^9}\right)\right],\end{aligned}$$

with $\mathcal{A}_{\rm gSi/gO}$ and $\mathcal{B}_{\rm gSi/gO}$ being the graphene–silicon/graphene–oxygen attractive and repulsive constants, respectively.

Since in this chapter we model the fold of multi-layer graphene sheets supported on a substrate, we take into account all graphene–graphene and graphene–substrate interactions to model ϵ as a linear combination of three energy components. With reference to Fig. 4.1, we consider three regions for the interaction energy to approximate ϵ as

$$\epsilon = \epsilon_{2N\rm gs} - \epsilon_{N\rm gs} - \epsilon_{N\rm g},$$

where $\epsilon_{2N\rm gs}$ denotes the interaction energy between $2N$ graphene layers and the substrate in the flat region, $\epsilon_{N\rm gs}$ denotes the interaction energy between N graphene layers and the substrate in the folded region near the substrate, and $\epsilon_{N\rm g}$ denotes the interaction energy between N graphene layers in the folded region away from the substrate. The interaction energy between N graphene layers $\epsilon_{N\rm g}$ is calculated by

$$\epsilon_{N\rm g}(\varphi) = \sum_{j=1}^{N-1}(N-j)\,\epsilon_{\rm gg}(j\varphi), \tag{4.29}$$

from which we take into account the change in the graphene–graphene equilibrium distance as the number of layers changes. The value for the equilibrium separation distance $\delta_{\rm gg}$ is determined for different numbers of layers N, independently. As illustrated by Fig. 4.2, the value of $\delta_{\rm gg}$ is prescribed such that (4.29) takes a minimum value, that is $\left[{\rm d}\epsilon_{N\rm g}/{\rm d}\varphi\right]_{\varphi=2\delta_{\rm gg}} = 0$.

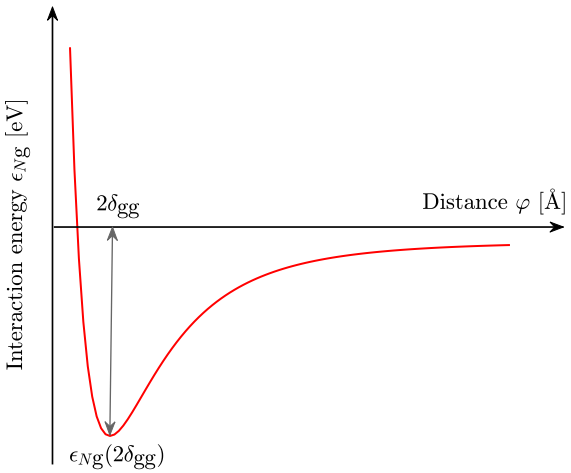

Figure 4.2: The LJ potential showing the interaction energy between N graphene layers $\epsilon_{N\mathrm{g}}(\varphi)$.

The interaction energy between N graphene layers and the substrate $\epsilon_{N\mathrm{gs}}$ is calculated by

$$\epsilon_{N\mathrm{gs}}(\tilde{\varphi}) = \epsilon_{N\mathrm{g}}(2\delta_{\mathrm{gg}}) + \sum_{j=1}^{N-1} \epsilon_{\mathrm{gs}}(\tilde{\varphi} + 2j\delta_{\mathrm{gg}}). \tag{4.30}$$

In a similar way, we account for the change in the graphene–substrate equilibrium distance as the number of layers changes. The values of δ_{gs} are determined for different numbers of layers N such that (4.30) takes a minimum value, that is $[\mathrm{d}\epsilon_{N\mathrm{gs}}/\mathrm{d}\tilde{\varphi}]_{\tilde{\varphi}=\delta_{\mathrm{gs}}} = 0$.

The LJ parameters for the graphene–substrate interaction, $\mathcal{A}_{\mathrm{gs}} = 4\xi_{\mathrm{gs}}\sigma_{\mathrm{gs}}^6$ and $\mathcal{B}_{\mathrm{gs}} = 4\xi_{\mathrm{gs}}\sigma_{\mathrm{gs}}^{12}$, are determined by the empirical mixing rules, which are given by $\xi_{\mathrm{gs}} = \sqrt{\xi_{\mathrm{g}}\xi_{\mathrm{s}}}$ and $\sigma_{\mathrm{gs}} = (\sigma_{\mathrm{g}} + \sigma_{\mathrm{s}})/2$, and their values are taken from Ref. [84]. In this study, $D_{\mathrm{g}} = 0.3812\,\text{Å}^{-2}$ is used to denote the surface density of carbon atoms on a sheet of graphene, while $D_{\mathrm{Si}} = 0.02654\,\text{Å}^{-3}$ and $D_{\mathrm{O}} = 0.05308\,\text{Å}^{-3}$ are used to denote the volume densities of silicon and oxygen

atoms in the SiO_2 substrate, respectively. Table 4.1 summarises the obtained values for δ_{gg}, δ_{gs}, and ϵ for different numbers of graphene layers folded on a SiO_2 substrate. Substitution of the parameter values from Table 4.1 into our solutions presented in Section 4.4, leaves only one parameter still to be determined, namely β_Y. The value of β_Y may be calculated such that the endpoint $y_{C_2}(\theta = 0)$ satisfies the boundary condition $y_2 = \delta_{gs} + (3N - 1)\delta_{gg}$, making it possible to fully determine our solution.

4.6 Results

In this section, we first investigate the effects of different approximations of the total squared curvatures κ^2_{tot} on the folding conformation of multi-layer graphene located on a SiO_2 substrate. The values of bending rigidity $\gamma = 1.0\,eV$, and number of layers $N = 2$ are adopted for this analysis. In Fig. 4.3, the predicted profile of the folded 2–layer graphene sheets on a SiO_2 substrate is presented for each considered approximation of κ^2_{tot}. The analysis reveals significant differences between these approximations in the hump height of the fold, that is the measured height from the point where

Table 4.1: Numerical values for δ_{gg}, δ_{gs}, and ϵ obtained using LJ potential.

N	δ_{gg} (Å)	δ_{gs} (Å)	ϵ (eV/Å^2)
2	1.7155	3.0171	0.03699
3	1.7111	3.0130	0.03825
4	1.7093	3.0117	0.03871
5	1.7084	3.0112	0.03893
6	1.7078	3.0110	0.03905

the folding edge becomes flat to the maximum height obtained. Using the one-term approximation, a hump height of $h_{\mathrm{h}} = 0.93\,\text{Å}$ is obtained, which is significantly smaller than the hump heights of $h_{\mathrm{h}} = 5.23, 5.68\,\text{Å}$ obtained from the two-term and the three-term approximations, respectively. Since the one-term approximation is shown not to be consistent with previous experimental measurements [7], it is not used in further comparisons. However, the one-term approximation is largely equivalent to the model used by Meng et al. [57] where the folding conformation of unsupported multi-layer graphene is modelled. The folding profile of 8–layer graphene is accurately predicted in Ref. [57], using both the finite-deformation model and molecular dynamics simulations. The difference in predicting the folding profile may be justified by the significance of the vdW interaction energy in each model. Since the model presented here is applied to supported multi-layer graphene, the vdW interactions between graphene layers and the substrate are more important.

Further, we compare our solutions to experimental measurements of hump heights. The one-term approximation is not consistent with previous results reported by Chen et al. [7], while the two-term and three-term approximations are consistent for 2–3 and 2–5 layers, respectively. A representative plot for the comparison is shown in Fig. 4.4. As the number of layers N increases, our model predicts the hump height more accurately as more terms are included in the total squared curvatures approximation κ^2_{tot}. However, for $N \geq 6$, it appears that even the three-term approximation would be insufficient to accurately predict hump heights. A representative selection of folding profiles are presented in Fig. 4.5 for different numbers of layers N using the two-term and three-term approximations. Although we do not take into consideration any defects in the graphene structure, our model shows good agreement with the experimental measurements of the hump height re-

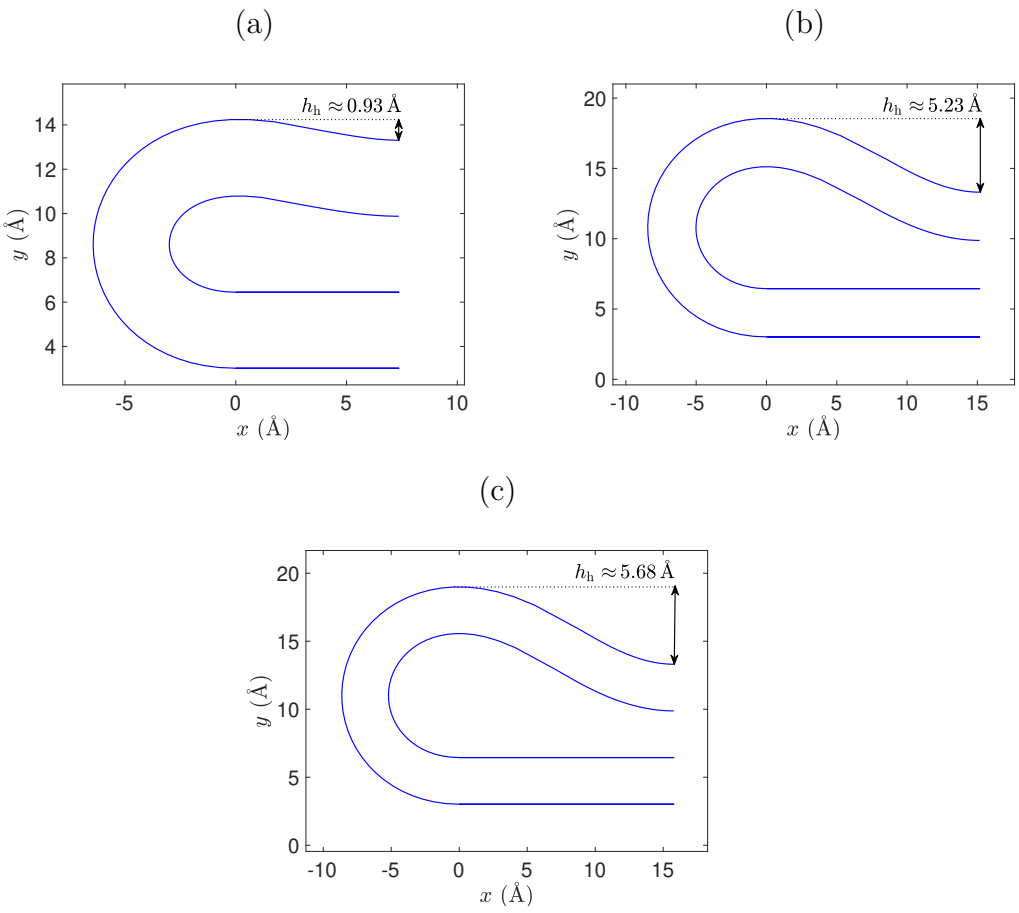

Figure 4.3: The predicted folding profiles of 2–layer graphene sheets located on a SiO_2 substrate using: (a) the one-term approximation, (b) the two-term approximation, and (c) the three-term approximation.

ported by Chen et al. [7]. They also employ their nonlinear mechanics model in conjunction with atomic force microscopy to investigate the bending rigidity multi-layer graphene, and a comparison to their results in this regard will be made in Chapter 5.

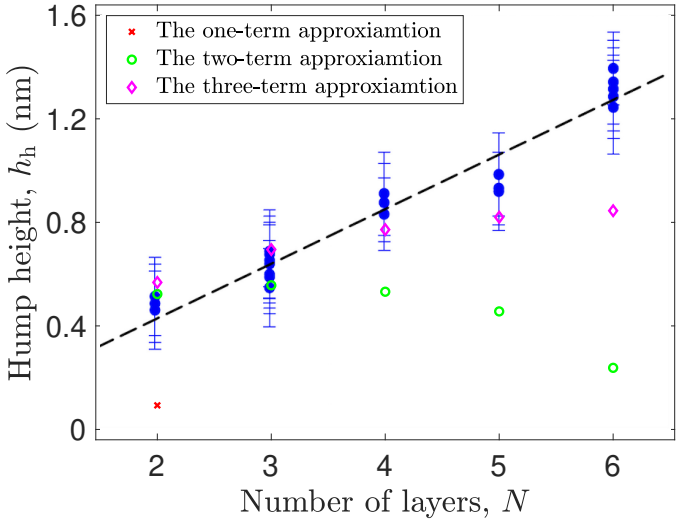

Figure 4.4: Hump heights obtained from the present model using $\gamma = 1.0\,\text{eV}$ superimposed upon the experimental results, reprinted from [7] with the permission of AIP Publishing, for comparison purposes.

4.7 Conclusion

In this chapter, a mathematical model is developed to determine the folding conformation of multi-layer graphene sheets located on a substrate. Due to the assumed translational symmetry of the fold, a 2D problem is proposed. The model is nondimensionalised, and the calculus of variations is used to minimise the energy functional and determine the shape of the fold. Solutions are derived for different approximations of the total squared curvature κ_{tot}^2 based on the mid-line, which is introduced as a notional curve when the number of layers is even. In analysing our solution, we consider SiO_2 as the supporting substrate, and the vdW interaction energy between graphene layers and the substrate, as well as the equilibrium spacing distances, are obtained using the LJ potential and presented in Table 4.1. The bound-

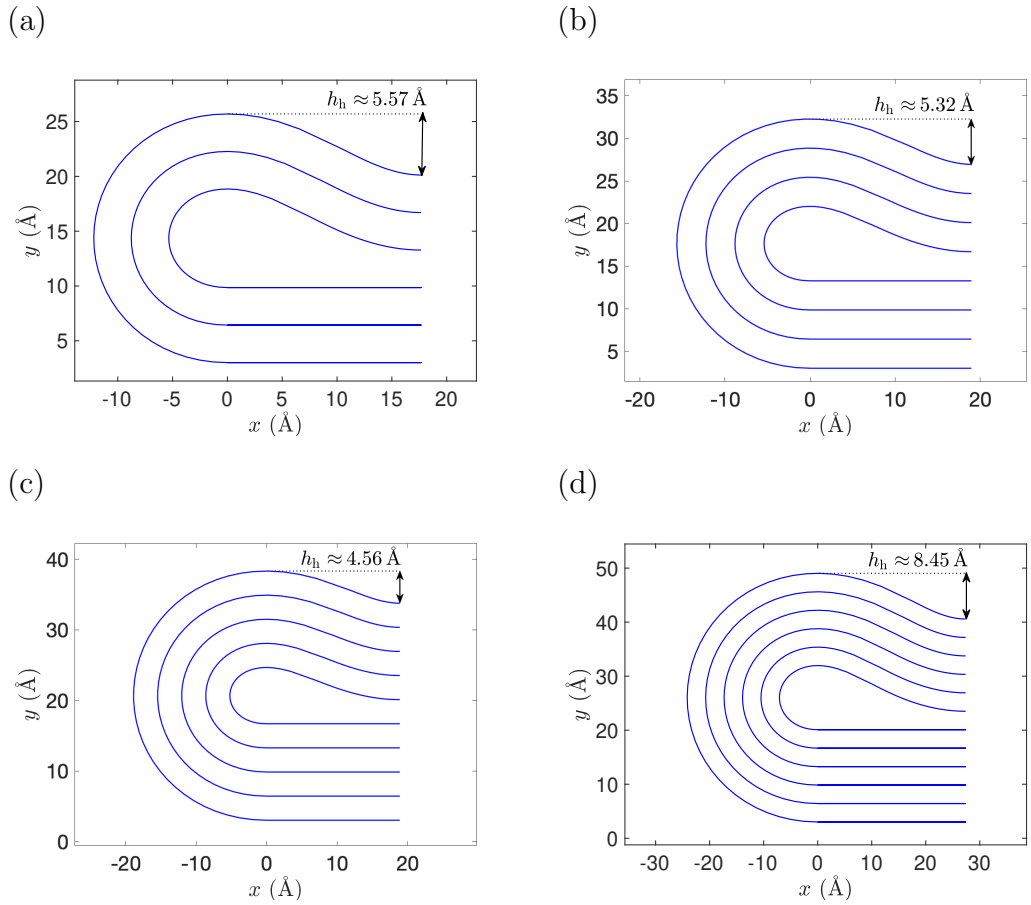

Figure 4.5: The predicted folding profiles of: (a) 3–layer (the two-term approximation), (b) 4–layer (the two-term approximation), (c) 5–layer (the two-term approximation), and (d) 6–layer (the three-term approximation), graphene sheets located on a SiO_2 substrate.

ary condition on y at the end point s_2 is used to determine the value of the unknown constant β_Y that arises after integrating the Euler–Lagrange equations.

The folding conformation of multi-layer graphene located on a SiO_2 substrate is investigated using three different approximations of κ^2_{tot}. The one-term approximation yields a much smaller hump height than the other two approximations. Furthermore, hump heights obtained from our model are compared with the experimental data reported by Chen et al. [7] for different numbers of graphene layers. Representative plots for predicted folding profiles and a comparison of hump heights is shown in Fig. 4.3, 4.4, and 4.5. While this model is applied to supported multi-layer graphene and accounts for the interaction energy between graphene layers and the substrate; the two-term and three-term approximations are shown to be consistent with experimental data for folded graphene with 2–3 and 2–5 layers, respectively.

4.8 Nomenclature

Symbol	Description
$\dot{\square}$	derivatives of $\square$ with respect to S
$\square'$	derivatives of $\square$ with respect to θ
N	the total number of graphene layers
C	the curve from (x_0, y_0) to (x_3, y_3)
C_1/C_2	the negative/positive curvature regions of the curve C
C_3	the zero curvature region of the curve C
(x_1, y_1)	the point where curvature changes sign
L_{fold}	the arc length of the folded region
L_{flat}	the length of the flat region
$2\delta_{\text{gg}}$	the graphene–graphene equilibrium distance
δ_{gs}	the graphene–substrate equilibrium distance
R_{m}, $R_{j,\text{o/i}}$	the curvature radius of mid-line, outer/inner curve
κ_{m}, $\kappa_{j,\text{o/i}}$	the line curvature of mid-line, outer/inner curve
s_i	the arc length at the point (x_i, y_i)
S_i	the nondimensional arc length at the point (X_i, Y_i)
E_{e}	the elastic energy
γ	the bending rigidity of graphene
κ_{tot}^2	the total squared curvatures of multiple curves
E_{v}	the vdW interaction energy
ϵ	the vdW interaction energy per unit length
$u(x)$	a Heaviside unit step function
E_{tot}	the total energy
L_{tot}	the total arc length of C
$\hat{\square}$	the nondimensional expression of $\square$

λ	a Lagrange multiplier
F	the integrand part of a functional
$F_{\square}$	the partial derivative of F with respect to the variable $\square$
β_X, β_Y	constants of integration
δ	the variation of a functional or variable
α	a scaling factor
μ, ρ	parameters used to simplify calculations
θ	the angle made by the tangent vector with the horizontal axis
ω	a substitution used to write an equation as a cubic equation
$\mathcal{D}$	the discriminant of a cubic equation
p, q	notations used to simplify calculations
g_1, g_2	functions from which the solution curves are constructed
A, B	parameters used for simplification purposes
X_{C_i}/Y_{C_i}	the nondimensional parametric solution for the curve C_i
x_{C_i}/y_{C_i}	the dimensional parametric solution for the curve C_i
$\epsilon_{N\mathrm{g}}$	the vdW interaction strength between N graphene layers
$\epsilon_{N\mathrm{gs}}$	the vdW interaction strength between N graphene layers and the substrate
$\epsilon_{\mathrm{gg}}(\varphi)$	the graphene–graphene vdW interaction strength at a distance φ
D_{g}	the surface density of carbon atoms on a sheet of graphene
$\epsilon_{\mathrm{gs}}(\tilde{\varphi})$	the graphene–substrate vdW interaction strength at a distance $\tilde{\varphi}$
D_{s}	the volume density of the chemical element of the substrate
$\mathcal{A}_{\mathrm{g}\square}/\mathcal{B}_{\mathrm{g}\square}$	positive constants of the graphene–$\square$ attraction/repulsion
$\xi_{\mathrm{g}\square}/\sigma_{\mathrm{g}\square}$	the graphene–$\square$ energy well depth/vdW diameter
h_{h}	the hump height of the fold

Chapter 5

The effective bending rigidity of multi-layer graphene

5.1 Introduction

In Section 1.2, we introduce the idea that the reconfiguration of the planar graphene sheet notionally leads to novel carbon nanostructures with new properties. Two examples that illustrate this point are single- and multi-walled carbon nanotubes, which may be thought of as rolled up single- and multi-layer graphene, respectively [24]. Thus, the bending rigidity of graphene is often a key factor in determining the geometry and properties of novel carbon nanostructures. Theoretical studies have reported that the bending rigidity of single-layer graphene is in the range of 0.83–1.60 eV [15], which largely agrees with experimental observations that report that a value of 1.20 eV fits the measurement range very well [31]. The bending rigidity of single-layer graphene is relatively well explored, but there is less understanding of the bending rigidity for multi-layer graphene.

Although the bending rigidity of multi-layer graphene has not been in-

vestigated in as much depth as single-layer graphene, some theoretical approaches have been explored. Examining self-folding conformations on a flat substrate, Chen et al. [7] report that the bending rigidity of 2– to 6–layer graphene follows a quadratic relationship with its thickness. On the other hand, Shen and Wu [85] employ continuum theory combined with atomistic simulations and find that the bending rigidity is linearly proportional to the number of layers when the number of layers exceeds five. The fold of unsupported multi-layer graphene has been modelled previously by Meng et al. [57], where they utilised their earlier model for a folded single-layer graphene. In that study, the bending rigidity of multi-layer graphene is modelled by multiplying the bending rigidity of the single-layer graphene by the number of layers, which represents a linear relationship between the bending rigidity and the number of layers. Experimental measurements of the bending rigidity of multi-layer graphene are reported by Han et al. [86] for several different numbers of graphene layers, and they hypothesise a sharp decrease in the bending rigidity depending on the bending angle.

In this chapter, we propose a novel analytical prediction for the effective bending rigidity γ_{eff} of multi-layer graphene sheets. A mathematical model for the folding of supported multi-layer graphene is developed in Chapter 4, where different approximations for the total curvature have been examined. In that chapter, we find that the three-term approximation renders results that are consistent with experimental measurements for up to five layers. To derive a model for unsupported multi-layer folds, we modify the model developed in Chapter 4 to produce a novel model for the folding of unsupported multi-layer graphene, employing the three-term approximation. Following this, we compare our solution to a solution derived earlier for folded single-layer graphene [3]. By treating the bending rigidity of the single-layer

graphene as a fitting parameter, we define the effective bending rigidity γ_{eff} as a function of the number of layers N.

The remainder of this chapter is divided into five sections. In the next section, a general mathematical formulation to model the folding conformation of graphene is presented. In Section 5.3, parametric solutions for folded multi-layer graphene are derived, that take into account the curvature of each graphene layer. Following this, in Section 5.4, reduced solutions for the mid-line of the fold are determined, considering only the curvature of the mid-line while treating the bending rigidity as a parameter somewhat like a fitting parameter. In Section 5.5, we investigate the effective bending rigidity of multi-layer graphene and compare our results with those reported in the literature. A summary and some concluding remarks are presented in Section 5.6.

5.2 Model formulation

In Chapter 4, variational calculus is employed to formulate a continuous model for the folding conformation of multi-layer graphene sheets supported on a substrate. In this chapter, similar techniques are employed to model the folding conformation of unsupported multi-layer graphene sheets and investigate the effective bending rigidity γ_{eff}. For example, a representative plot for the geometry of folded 3–layer graphene sheets is shown in Fig. 5.1. The model is constructed based on the mid-line of a multi-layer graphene stack, which is the middle graphene layer when the number of layers is odd ($N = 2n+1$), or a notional layer when the number of layers is even ($N = 2n$), for some integer n. Assuming a translational symmetry in the fold direction, a 2D problem is considered in this work. Furthermore, the fold is assumed

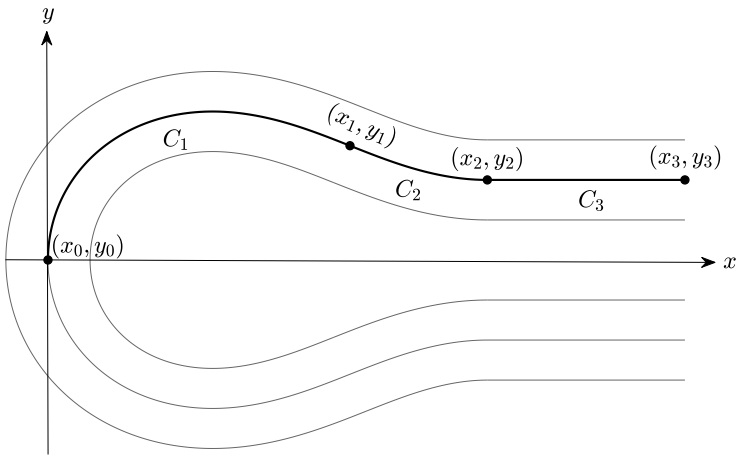

Figure 5.1: Schematic showing the geometry of folded unsupported 3–layer graphene stack.

to possess a reflective symmetry in the x–axis, and therefore we need only analyse the upper half of the mid-line which is the solid curve in Fig. 5.1.

In addition to the considerations above, the upper half of the mid-line is divided into three curves according to the sign of the line curvature κ_{m} and line gradient $\mathrm{d}y/\mathrm{d}x$. The first curve is bounded by the points (x_0, y_0) and (x_1, y_1) with a strictly negative curvature and is denoted by C_1. The second curve is bounded by the points (x_1, y_1) and (x_2, y_2) with a strictly positive curvature and is denoted by C_2. The flat region is denoted by C_3, from the point (x_2, y_2) to the point (x_3, y_3) and has zero curvature. The concatenation of all these three curves is denoted by C.

The folding conformation of graphene is determined from the elastic bending energy of the graphene and the vdW interaction energy between the graphene layers [3]. The elastic bending energy is assumed to be proportional to the square of the curvature. The curvature vanishes in C_3; hence,

the elastic bending energy is only due to the bended regions of the curve C. Thus, we express the elastic energy E_{e} mathematically as

$$E_{\mathrm{e}} = \int_{C_1+C_2} \gamma \kappa_{\mathrm{tot}}^2 \, \mathrm{d}s \,,$$

where γ is a positive constant denoting the bending rigidity of graphene, s is the arc length, and κ_{tot}^2 is the total squared curvature. Additionally, the contribution of the vdW interaction energy is approximated such that it dominates only in the flat region that is the curve C_3. Hence, it is modelled as

$$E_{\mathrm{v}} = -\epsilon \, (x_3 - x_2) \,,$$

where ϵ is a positive constant that denotes the vdW interaction energy per unit length between graphene layers. Hence, the total energy for this problem is given by

$$E_{\mathrm{tot}} = E_{\mathrm{e}} + E_{\mathrm{v}} = \int_{C_1+C_2} \gamma \kappa_{\mathrm{tot}}^2 \, \mathrm{d}s - \epsilon \, (x_3 - x_2) \,. \tag{5.1}$$

Furthermore, the graphene is assumed to have a fixed length; therefore, an isoperimetric constraint is imposed on the total arc length of the curve C, that is

$$L_{\mathrm{tot}} = \int_C \mathrm{d}s = \int_{C_1+C_2} \mathrm{d}s + (x_3 - x_2) \,, \tag{5.2}$$

where $2L$ is the total arc length of the mid-line including the lower half. These considerations are identical to those considered in Section 4.2, which lead to a total energy functional that is identical to (4.8). Therefore, the functional to be minimised for this model is

$$E_{\mathrm{tot}} = \int_0^{s_2} \left(\gamma \, \kappa_{\mathrm{tot}}^2 + \epsilon \right) \, \mathrm{d}s \,, \tag{5.3}$$

where s_2 is the arc length from the point (x_0, y_0) to the point (x_2, y_2). As shown in Fig. 5.1, the fold of the mid-line is assumed to start at the origin of

the plane, so that the functional (5.3) is subject to the boundary conditions, at $s = 0$:

$$x = 0, \quad y = 0, \quad \mathrm{d}x/\mathrm{d}s = 0, \quad \mathrm{d}y/\mathrm{d}s = 1,$$

and at the endpoint $s = s_2$:

$$x = x_2, \quad y = N\delta_{\mathrm{gg}}, \quad \mathrm{d}x/\mathrm{d}s = 1, \quad \mathrm{d}y/\mathrm{d}s = 0,$$

where the layers are assumed to maintain an equal distance $2\delta_{\mathrm{gg}}$ from one another and the value of x_2 is not fixed *a priori*.

It is anticipated that, as the number of layers N is increased, the vdW interaction energy ϵ increases, and the spacing distance between adjacent layers $2\delta_{\mathrm{gg}}$ decreases. Therefore, the LJ potential is employed to model values for δ_{gg} and ϵ for different numbers of layers N. With reference to Fig. 5.1, we model the interaction energy ϵ considering the flat and bended regions, which we approximate by

$$\epsilon = \epsilon_{2N\mathrm{g}} - 2\epsilon_{N\mathrm{g}},$$

where the first term $\epsilon_{2N\mathrm{g}}$ accounts for the interaction energy between $2N$ graphene layers in the flat region, and the second term $2\epsilon_{N\mathrm{g}}$ accounts for the interaction energy between N graphene layers in two bended regions. As in Section 4.5, the interaction energy between N graphene layers $\epsilon_{N\mathrm{g}}$ is calculated by

$$\epsilon_{N\mathrm{g}}(\varphi) = \sum_{j=1}^{N-1} (N - j)\, \epsilon_{\mathrm{gg}}(j\varphi),$$

where we recall from Section 2.2.1 that the strength of the graphene–graphene vdW interaction ϵ_{gg} at a distance φ may be modelled by

$$\epsilon_{\mathrm{gg}}(\varphi) = D_{\mathrm{g}}^2 \left(-\frac{\pi \mathcal{A}_{\mathrm{gg}}}{2\varphi^4} + \frac{\pi \mathcal{B}_{\mathrm{gg}}}{5\varphi^{10}} \right).$$

The value of δ_{gg} is determined such that the equation $[\mathrm{d}\epsilon_{N\mathrm{g}}/\mathrm{d}\varphi]_{\varphi=2\delta_{\mathrm{gg}}} = 0$, is satisfied. Table 5.1 presents the values of δ_{gg} and ϵ used in this chapter. In the following two sections, two calculations for the total squared curvature κ^2_{tot}, based on different assumptions, are described. In Section 5.3, we take into account the curvature effect of each graphene layer in the calculation of κ^2_{tot}. In Section 5.4, the calculation is simplified by considering only the mid-line curvature. We also present the corresponding parametric solution for the mid-line in each case.

5.3 Multi-layer solution

In this section, we propose a model of the folding conformation of N graphene layers stacked one on top of the other. As reported by Wei et al. [15], the bending rigidity of single-layer graphene is found to be in the range of 0.83–1.60 eV. For the purpose of the analysis here, the bending rigidity of each graphene layer is prescribed to be $\gamma = 1.0\,\mathrm{eV}$. In this section, we also account for the curvature of each graphene layer, and the three-term approximation

Table 5.1: Numerical values for δ_{gg}, and ϵ obtained using the LJ potential.

N	δ_{gg} (Å)	ϵ (eV/Å^2)
2	1.7155	0.0361
3	1.7111	0.0378
4	1.7093	0.0384
5	1.7084	0.0387
6	1.7078	0.0389
7	1.7074	0.0390

derived in Section 4.2 is adopted here for the total squared curvature $\kappa_{\rm tot}^2$. That is

$$\kappa_{\rm tot}^2 \approx N\kappa_{\rm m}^2 + N(N^2-1)\delta_{\rm gg}^2\kappa_{\rm m}^4 + N(N^2-1)(N^2-7/3)\delta_{\rm gg}^4\kappa_{\rm m}^6, \qquad (5.4)$$

where $\kappa_{\rm m}$ denotes the mid-line curvature and is given by

$$\kappa_{\rm m}(s) = \dot{x}\ddot{y} - \ddot{x}\dot{y},$$

and dots here denote differentiation with respect to s. Substituting (5.4) into (5.3) gives the functional to be minimised subject to the boundary conditions given in Section 5.2.

Variational calculus and nondimensionalisation methods are employed in Section 4.3 to minimise this functional. A change of variables is also made such that

$$\frac{\mathrm{d}}{\mathrm{d}S} = \left(\frac{\mathrm{d}\theta}{\mathrm{d}S}\right)\frac{\mathrm{d}}{\mathrm{d}\theta}, \quad \text{and} \quad \frac{\mathrm{d}S}{\mathrm{d}\theta} = \left(X'^2 + Y'^2\right)^{1/2},$$

where S is the nondimensional arc length and primes denote derivatives with respect to θ, the angle made by the tangent vector with the horizontal axis. Then, the expression for the nondimensional curvature $\hat{\kappa}_{\rm m}(\theta)$ is

$$\hat{\kappa}_{\rm m}(\theta) = \pm\left[\left(\sqrt{\frac{q^2}{4}+\frac{p^3}{27}}-\frac{q}{2}\right)^{1/3} - \frac{p}{3}\left(\sqrt{\frac{q^2}{4}+\frac{p^3}{27}}-\frac{q}{2}\right)^{-1/3} - \frac{\mu}{5\rho}\right]^{1/2},$$

with

$$\mu = \left(\frac{\epsilon\delta_{\rm gg}^2}{N\gamma}\right)(N^2-1), \qquad \rho = \left(\frac{\epsilon\delta_{\rm gg}^2}{N\gamma}\right)^2(N^2-1)(N^2-7/3),$$
$$p = \frac{5\rho-3\mu^2}{(5\rho)^2}, \quad \text{and} \quad q(\theta) = \mu\,\frac{2\mu^2-5\rho}{(5\rho)^3} - \frac{1}{5\rho}\left(1-\beta_Y\sin\theta\right),$$

where β_Y is an arbitrary constant arising from a first integral of the Euler–Lagrange equation.

Taking into account the boundary conditions, the mid-line is represented by a parametric solution arrived at by integrating the following pair of differential equations

$$X' = \frac{\cos\theta}{\hat{\kappa}_{\mathrm{m}}(\theta)}, \quad Y' = \frac{\sin\theta}{\hat{\kappa}_{\mathrm{m}}(\theta)}.$$

Note that (X_1, Y_1) is the boundary point between the curve C_1 with the negative curvature and the curve C_2 with the positive curvature. This point has zero curvature and corresponds to $\theta = \theta_1$. By solving $\hat{\kappa}_{\mathrm{m}}(\theta_1) = 0$, we may obtain $\theta_1 = \sin^{-1}(1/\beta_Y)$.

For the curve C_1, we have $\theta \in [-\pi/2, \theta_1]$ and the parametric solution is

$$X_{C_1}(\theta) = \int_{-\pi/2}^{\theta} \frac{\cos\tilde{\theta}}{\hat{\kappa}_{\mathrm{m}}(\tilde{\theta})}\,\mathrm{d}\tilde{\theta}\,, \quad Y_{C_1}(\theta) = -\int_{-\pi/2}^{\theta} \frac{\sin\tilde{\theta}}{\hat{\kappa}_{\mathrm{m}}(\tilde{\theta})}\,\mathrm{d}\tilde{\theta}\,.$$

For the curve C_2, our solution must be continuous at the point (X_1, Y_1) where $\hat{\kappa}_{\mathrm{m}}$ changes sign, so that to satisfy this condition we adopt different signs of $\hat{\kappa}_{\mathrm{m}}(\tilde{\theta})$ than those used for C_1. Hence, the parametric solution for the curve C_2 is given by

$$X_{C_2}(\theta) = X_{C_1}(\theta_1) - \int_{\theta_1}^{\theta} \frac{\cos\tilde{\theta}}{\hat{\kappa}_{\mathrm{m}}(\tilde{\theta})}\,\mathrm{d}\tilde{\theta}\,,$$
$$Y_{C_2}(\theta) = Y_{C_1}(\theta_1) + \int_{\theta_1}^{\theta} \frac{\sin\tilde{\theta}}{\hat{\kappa}_{\mathrm{m}}(\tilde{\theta})}\,\mathrm{d}\tilde{\theta}\,,$$

where $\theta \in [0, \theta_1]$.

Parametric solutions for the j^{th} outer/inner curve may be determined using the equations

$$X_{j,\mathrm{i/o}}(\theta) = X(\theta) \pm \frac{\nu\delta_{\mathrm{gg}}}{\alpha_{\mathrm{m}}}\left(\frac{Y'}{\sqrt{X'^2 + Y'^2}}\right),$$
$$Y_{j,\mathrm{i/o}}(\theta) = Y(\theta) \mp \frac{\nu\delta_{\mathrm{gg}}}{\alpha_{\mathrm{m}}}\left(\frac{X'}{\sqrt{X'^2 + Y'^2}}\right),$$

where $X(\theta)$ and $Y(\theta)$ represent the parametric solution of the mid-line, and $\nu = 2j$ when N is odd, or $\nu = 2j - 1$ when N is even, for $j \in \{1, \ldots, n\}$. As

in Section 4.4.2, multiplying these nondimensional solutions by the scaling factor $\alpha_{\mathrm{m}} = \sqrt{N\gamma/\epsilon}$ recovers the dimensional solutions for the folded curve of C. The unknown parameter β_Y is determined using the boundary condition $y_2 = N\delta_{\mathrm{gg}}$, and hence our solution for the mid-line of the fold is fully determined.

5.4 Single-layer solution

In this section, a reduced model that can be used to obtain the conformation of the mid-line of the fold is developed. Here, only the curvature of the mid-line is considered; thus, the total squared curvature κ_{tot}^2 reduces to

$$\kappa_{\mathrm{tot}}^2 = \kappa_{\mathrm{m}}^2 = (\dot{x}\ddot{y} - \ddot{x}\dot{y})^2 . \tag{5.5}$$

Substituting (5.5) into the total energy functional (5.3) gives the functional to be minimised subject to the boundary conditions given in Section 5.2. A solution to this style of problem has been previously derived by Cox et al. [3] to model the fold of a single-layer graphene sheet. With two modifications, their solution is exploited here to generate a simplified solutions for the fold of the mid-line of multi-layer graphene. First, the parameter γ is treated here as a fitting parameter rather than a material property. Second, the endpoints must satisfy the boundary conditions of the functional (5.3).

The substitution $\theta = 2\phi - \pi/2$, can be used to obtain a solution that can be described by the two functions $g_1(\phi)$ and $g_2(\phi)$ given by (4.27). However, the parameters in (4.28) are defined so that

$$A = \frac{2(\alpha_{\mathrm{s}} + \beta)^{1/2}}{\beta}, \quad B = \frac{\alpha_{\mathrm{s}}}{\alpha_{\mathrm{s}} + \beta}, \quad k = \left(\frac{2\beta}{\alpha_{\mathrm{s}} + \beta}\right)^{1/2},$$

where β is an arbitrary constant of integration, and $\alpha_{\mathrm{s}} = \epsilon/\gamma$, as defined in [3]. For C_1, the curve with negative curvature, the parametric solution is

given by

$$x_{C_1}(\phi) = g_1(0) - g_1(\phi), \quad y_{C_1}(\phi) = g_2(\phi),$$

where $\phi \in [0, \phi_1]$, and $\phi_1 = \sin^{-1}(1/k)$ corresponds to the point of zero curvature (x_1, y_1). For C_2, the curve with positive curvature, the parametric solution is given by

$$x_{C_2}(\phi) = g_1(0) + g_1(\phi), \quad y_{C_2}(\phi) = 2g_2(\phi_1) - g_2(\phi),$$

where $\phi \in [\phi_1, \pi/4]$. We comment that these solutions are dimensional. The parameter β may be determined by solving $y_{C_2}(\pi/4) = N\delta_{\text{gg}}$ numerically; hence, our solution for the mid-line is fully determined.

5.5 Results

In this section, the effective bending rigidity γ_{eff} of multi-layer graphene is investigated by examining the folding conformation of the mid-line of the graphene stack. We employ the multi-layer solution from Section 5.3 and the single-layer solution form Section 5.4 in the analysis. Recall that the single-layer solution has been previously derived by Cox et al. [3] for the fold of single-layer graphene, but we modify their solution in Section 5.4 to produce a simplified solution for the fold of multi-layer graphene. Fig. 5.2 illustrates our approach of reporting the effective bending rigidity γ_{eff} of 2–layer graphene. As in Fig. 5.2(a), the predicted folding profile of the mid-line, obtained from the solutions presented in Section 5.3, is compared to several curves, obtained from the solution presented in Section 5.4, with a range of values for the parameter γ. The area between each curve and the mid-line (A) is calculated as shown in Fig. 5.2(b), and the value of γ_{eff} is prescribed such that this area is minimised ($\text{A} = \text{A}_{\text{min}}$). Representative plots for the

predicted folding profiles of multi-layer graphene with $\gamma = 1.0\,\text{eV}$, and the predicted folding profile of single-layer graphene with $\gamma = \gamma_{\text{eff}}$ are shown in Fig. 5.2(c) and Fig. 5.3 where the numerical data is included in Table 5.2. We comment that as the number of layers N increases, the minimum area A_{min} also increases; hence, it can be concluded that the approach employed here is only suitable for predicting γ_{eff} when the number of layers N is relatively few (our results suggest that $N \leq 6$). This approach becomes increasingly inapplicable for larger N due to significant differences between the multi-layer solution and the single-layer solution in predicting the folding conformation.

It is worth noting that these values of γ_{eff} are reported according to the folding conformations obtained from the multi-layer solution where $\gamma = 1.0\,\text{eV}$ is used for the bending rigidity of each layer in the graphene stack. It is also noted that the effective bending rigidity for multi-layer graphene follows an approximate quadratic relationship with the number of layers N; hence, the effective bending rigidity may be expressed in terms of γ and N as

$$\gamma_{\text{eff}} \approx \gamma N^2, \tag{5.6}$$

where this relationship is also confirmed by a log–log plot as shown in Fig. 5.4(a). Although the curve shows that an exponent slightly less than 2 might be even better, we find an exponent of 2 is a good integer approximation. It is evident from Fig. 5.4(b) that the values obtained from this model for the effective bending rigidity of 2– to 6–layer graphene are slightly higher than the existing results reported by Chen et al. [7]. However, the results of this study confirm and capture their idea of the approximate quadratic relationship very well. Furthermore, the obtained values of γ_{eff} for 2–layer, 3–layer, 5–layer, and 7–layer graphene are in line with the experimental results reported by Han et al. [86], which are 2.6–5.8 eV, 3.7–12.2 eV, 26.0 eV,

and 12.0–53.0 eV, respectively.

In contrast to the assumed linear relationship [57], this model shows that simply using the single-layer solution, with the bending rigidity being multiplied by the number of layers, does not lead to an accurate folding conformation of multi-layer graphene. These obtained values of γ_{eff} are based on the choice of $\gamma = 1.0\,\text{eV}$ for the multi-layer solution; any lower (or higher) value of γ, within the physically meaningful range of 0.83–1.60 eV [15], would lead to better (or worse) agreement with the experimental results [7]. However, the aim of this work is to develop an analytical approach for estimating the effective bending rigidity of multi-layer graphene. Table 5.3 summarises the obtained (or assumed) relationships between the bending rigidity of multi-layer graphene and the number of layers N, as reported in the literature. While there is some disagreement with regards to the relationship between the bending rigidity and the number of layers, we mention that other researchers report that the bending rigidity exhibits an approximately linear proportionality to the number of layers when $N \geq 6$ [85].

Table 5.2: Numerical values for A_{min} and γ_{eff} for different numbers of layers N.

N	A_{min} (Å^2)	γ_{eff} (eV)
2	2.97	4.21
3	6.55	8.88
4	10.25	14.93
5	13.89	22.59
6	17.30	32.03
7	21.45	43.58

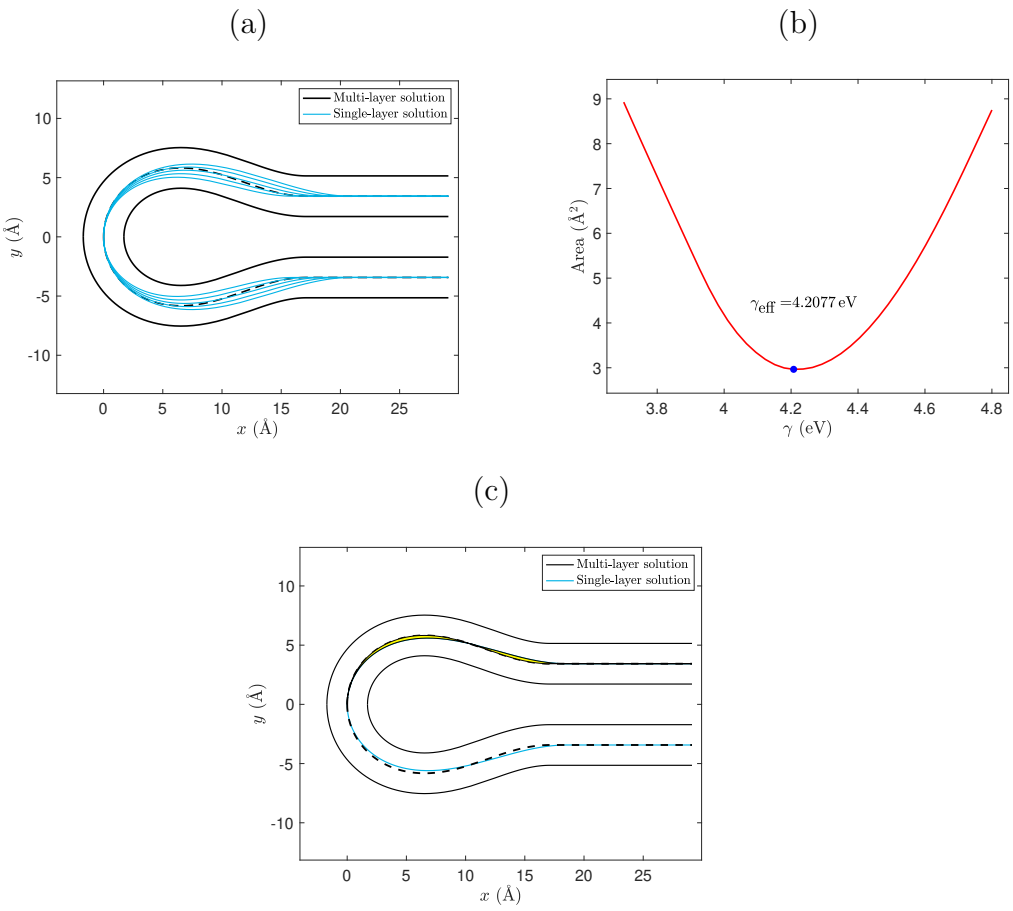

Figure 5.2: Representation of the steps taken to determine γ_{eff} of 2–layer graphene. (a) A series of curves (cyan), generated by the single-layer solution with a range of values for γ, are compared to the mid-line of the predicted folding profile of 2–layer graphene obtained from the multi-layer solution (black). (b) The area between the mid-line and these curves is plotted as a function of γ. (c) The predicted folding profile of 2–layer graphene with a comparison between the mid-line and the curve given by the single-layer solution with $\gamma = \gamma_{\text{eff}}$, where the area A_{min} is shaded in yellow.

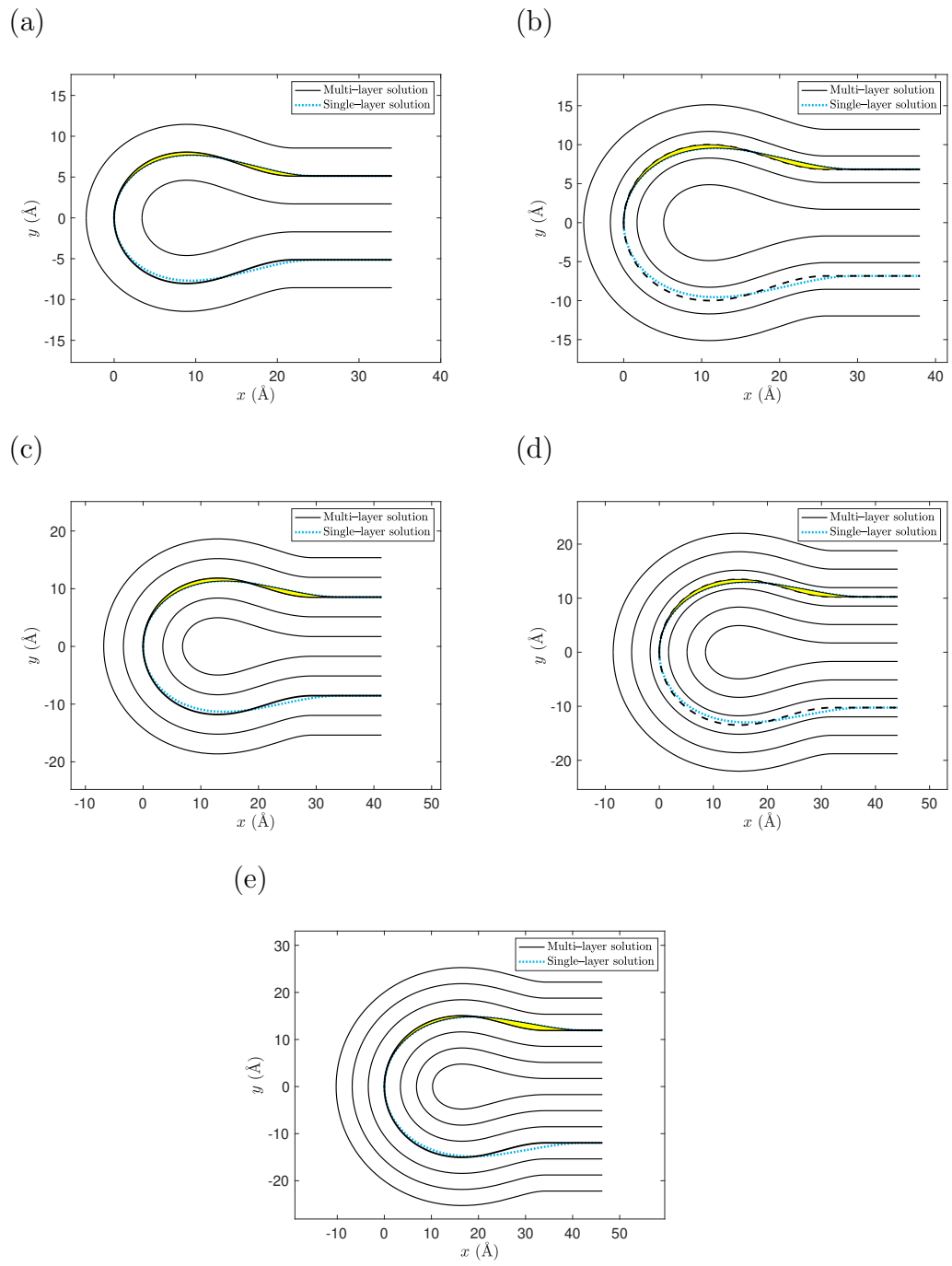

Figure 5.3: The predicted folding profile of: (a) 3–layer (b) 4–layer (c) 5–layer (d) 6–layer, (e) 7–layer, graphene obtained from the multi-layer solution (black) with a comparison between the mid-line and the curve (cyan) given by the single-layer solution with $\gamma = \gamma_{\text{eff}}$, where the area between these curves is shaded in yellow.

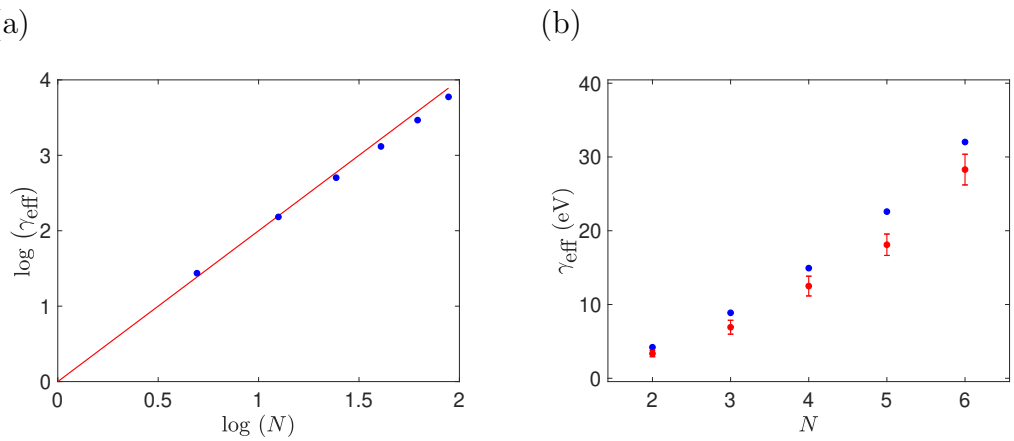

Figure 5.4: (a) The relationship between $\log(\gamma_{\text{eff}})$ and $\log(N)$. The blue dots correspond to the values presented in Table 5.2 which confirm the approximate relationship given in (5.6), represented by the red line. (b) The values of the effective bending rigidity obtained by the present model (blue dots) are compared to earlier results (represented by red), retrieved from Ref. [7].

5.6 Conclusion

This chapter presents a novel analytical approach to predict the effective bending rigidity of multi-layer graphene. Exploiting our work from Chapter 4, a mathematical model is constructed to predict the folding conforma-

Table 5.3: The relationship between the bending rigidity of multi-layer graphene and the number of layers N.

Reference	N	Relationship	Method
this study	≤ 6	quadratic	variational model
Ref. [7]	≤ 6	quadratic	nonlinear continuum model
Ref. [85]	≥ 6	linear	continuum theory/atomistic simulations
Ref. [57]	≤ 8	linear	finite-deformation beam theory

tion of unsupported multi-layer graphene sheets, where the values for the parameters ϵ and δ_{gg} are calculated based on the LJ potential. Then, the predicted folding profile of multi-layer graphene sheets is compared to several curves obtained from the single-layer solution for a range of values of the bending rigidity.

The effective bending rigidity is determined such that the area bounded by the mid-line and a curve obtained from the single-layer solution is minimised. For $N < 7$, it is demonstrated that the effective bending rigidity approximately follows a quadratic relationship in N, as given by (5.6), which is confirmed by a log–log plot presented in Fig. 5.4(a). This relationship is consistent with some earlier work, such as that given by Chen et al. [7], and the values of the effective bending rigidity obtained here are also in good agreement with experimental results [86].

5.7 Nomenclature

Symbol	Description
$\dot{\square}$	derivatives of $\square$ with respect to S
$\square'$	derivatives of $\square$ with respect to θ
γ_{eff}	the effective bending rigidity of multi-layer graphene
N	the total number of graphene layers
C	the curve from (x_0, y_0) to (x_3, y_3)
C_1/C_2	the negative/positive curvature regions of the curve C
C_3	the zero curvature region of the curve C
(x_1, y_1)	the point where curvature changes sign
E_{e}	the elastic energy
γ	the bending rigidity of graphene
κ_{tot}^2	the total squared curvatures of multiple curves
s_i	the arc length at the point (x_i, y_i)
S_i	the nondimensional arc length at the point (X_i, Y_i)
E_{v}	the vdW interaction energy
ϵ	the vdW interaction energy per unit length
E_{tot}	the total energy
L_{tot}	the total arc length of C
$2\delta_{\text{gg}}$	the graphene–graphene equilibrium distance
$\epsilon_{N\text{g}}$	the vdW interaction strength between N graphene layers
$\epsilon_{\text{gg}}(\varphi)$	the graphene–graphene vdW interaction strength at a distance φ
D_{g}	the surface density of carbon atoms on a sheet of graphene
$\mathcal{A}_{\text{gg}}/\mathcal{B}_{\text{gg}}$	positive constants of the graphene–graphene attraction/repulsion
κ_{m}	the line curvature of mid-line
θ	the angle made by the tangent vector with the horizontal axis

$\hat{\kappa}$	the nondimensional expression of κ
μ, ρ	parameters used to simplify calculations
p, q	notations used to simplify calculations
β_Y	a constant of integration for the multi-layer solution
X_{C_i}/Y_{C_i}	the nondimensional parametric solution for the curve C_i
α_{m}	a scaling factor for the multi-layer solution
x_{C_i}/y_{C_i}	the dimensional parametric solution for the curve C_i
g_1, g_2	functions from which the solution curves are constructed
A, B	parameters used for simplification purposes
β	a constant of integration for the single-layer solution
α_{s}	a parameter for the single-layer solution
$\mathrm{A}_{\mathrm{min}}$	the minimum area between multi-layer curve and single-layer curves

Chapter 6

Collapsed graphene wrinkles

6.1 Introduction

In Section 1.3, we introduce the various possible deformations in the structure of CVD-produced graphene, including ripples, arch-shaped wrinkles, self-adhered wrinkles, and collapsed wrinkles. Following this in Chapter 3, the behaviour of a rippled graphene sheet is investigated through a variational model. Another variational model has been constructed by Cox et al. [87] for both arc-shaped and self-adhered graphene wrinkles. Except for the case of collapsed wrinkles, each of these deformations has a reflective symmetry in the geometry which simplifies the modelling processes. In this chapter, we extend the variational approach to model the conformation of collapsed wrinkles, which in several ways is the most complicated structure that we consider in this thesis. A collapsed wrinkle forms when a self-adhered wrinkle folds over onto the surface after reaching some critical height. Although this critical height represents the transition point between these two different graphene configurations, only relatively few studies have reported numerical values for this transition height.

The critical height of the self-adhered wrinkle is the height at which the collapsed wrinkle has lower energy than the self-adhered wrinkle. Zhu et al. [38], report experimental measurements and make theoretical predictions of the critical height of the self-adhered wrinkle where SiO_2/Si is used as the supporting substrate. Through their experiments, they find that the critical height of the self-adhered wrinkle is approximately 6 nm, but they predict a higher value of 8.4 nm based on their theoretical calculations. In another study, Wang et al. [6], investigate the critical height for wrinkled graphene on a copper substrate and report an experimental value of 11 nm, while they predict a value of 7.6 nm based on theoretical considerations. Verhagen et al. [88], present atomic force microscopy images of graphene wrinkles on SiO_2/Si, showing height measurements for their profiles in the range from 9.4 to 10.1 nm. Furthermore, Long et al. [89] report that the critical height of self-adhered wrinkles on SiO_2/Si is experimentally found to be 5 nm. In a theoretical work by Zhang et al. [4], single- and multi-layer collapsed wrinkles are studied based on a quasi-analytical solution. Ignoring the effects of the substrate material, they predict a critical height of approximately 6.9 nm.

The conformations of self-adhered and collapsed wrinkles have been previously modelled using simplified energy formulations under the assumption the conformation is made up of circular arcs [4, 38]. In this chapter, a continuous approximation is adopted and a variational model is developed to firstly, predict morphologies for collapsed wrinkles, and then to calculate the critical height of the self-adhered wrinkle. We minimise the energy of the system by employing variational calculus to derive parametric solutions for these morphologies. This approach has been used by Cox et al. [87] to derive parametric solutions for two wrinkle configurations, the arch-shaped wrinkle and the self-adhered wrinkle. In the present chapter, these solutions

are exploited to determine the critical height of the self-adhered wrinkle by comparing the energy of the self-adhered wrinkle to that of the collapsed wrinkle.

This chapter is organised in the following way: in the next section, the mathematical model is formulated and three independent energy expressions are derived, each of which represents a specific part of the curve. Following in Section 6.3, variational calculus methods are applied to minimise each energy functional and derive parametric solutions for each part of the curve. We employ these solutions in Section 6.4, where some example substrate materials are considered, and the LJ potential is applied to account for the strengths of the graphene–substrate vdW interactions. In Section 6.5 the results are presented, and a comparison is made with previous theoretical and experimental studies. A brief summary is provided in the final section of this chapter.

6.2 Model formulation

The geometry of the self-adhered wrinkle and the collapsed wrinkle are shown in Fig. 6.1. The solid line represents the approximate excess length of graphene sheet, the total arc length of the graphene sheet profile compared to the length of the substrate (less the distance $2x_1$ where there is no direct graphene–substrate interaction), which is referred to by L_{tot}. Furthermore, the graphene–graphene equilibrium distance is denoted by $2\delta_{\text{gg}}$, while the graphene–substrate equilibrium distance is represented by δ_{gs}. As the self-adhered wrinkle has been previously modelled by Cox et al. [87], the focus of our modelling in this chapter is the conformation of the collapsed wrinkle. For convenience, transition regions are introduced and the curve of the col-

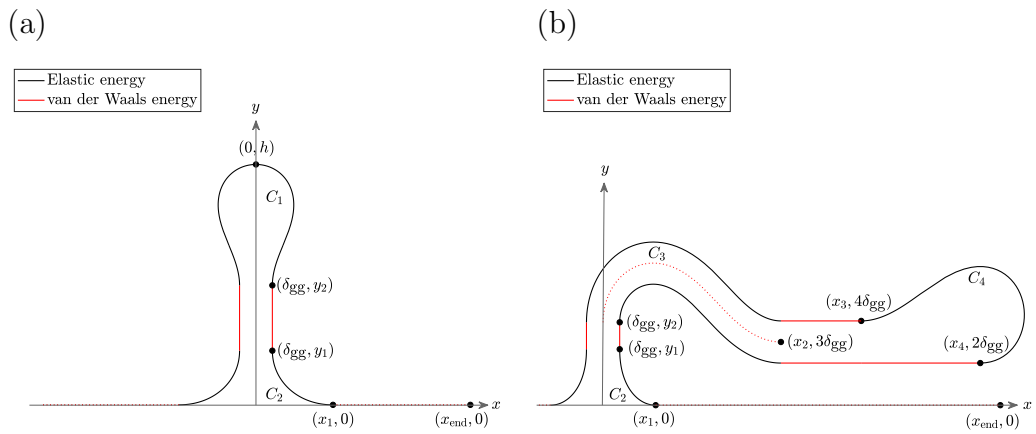

Figure 6.1: Schematic showing the geometry of: (a) self-adhered graphene wrinkle, (b) collapsed graphene wrinkle, supported on a substrate.

lapsed wrinkle is divided into three parts, as designated in Fig. 6.1(b). We avoid using the symbol C_1 for the collapsed wrinkle so as not to conflict with the notation used in Ref. [87]. Due to the reflective symmetry, the right-half of the first part is denoted by C_2. The curve C_3 is used to represent both sides of the collapsed wrinkle between the vertical and horizontal lines, while C_4 is used for the black curve from the point $(x_3, 4\delta_{\text{gg}})$ to the point $(x_4, 2\delta_{\text{gg}})$. The conformation of the curve C_2 is directly impacted by the strength of the graphene–substrate vdW interaction. The effects of the graphene–substrate vdW interaction on the conformation of C_3 and C_4 are relatively weak since the graphene–graphene vdW interaction is the dominating force due to the relatively more distant graphene–substrate vdW interaction. The effects of the graphene–substrate vdW interaction on the horizontal red lines are taken into account in Section 6.4, where we employ the LJ potential to model values for the strengths of the graphene–substrate vdW interactions.

With the aforementioned considerations in mind, the conformation of collapsed wrinkles is modelled by minimising the the graphene elastic energy

and maximising the vdW interaction energy. The graphene elastic energy E_{e} corresponds to the integral of the total squared curvatures; hence, it is only considered in the bended regions, but neglected in the regions with zero curvature (shown in solid red lines in Fig. 6.1(b)). Accordingly, we model E_{e} by the functional

$$E_{\mathrm{e}} = \gamma \left[2 \int_{C_2} \kappa^2 \, \mathrm{d}s + \int_{C_3} \kappa_{\mathrm{tot}}^2 \, \mathrm{d}s + \int_{C_4} \kappa^2 \, \mathrm{d}s \right],$$

where γ is a positive constant describing the bending rigidity of the graphene sheet, κ^2 is the squared line curvature of a single layer, and κ_{tot}^2 is the total squared curvatures of a pair of layers. Throughout this chapter, the line curvature κ is defined by

$$\kappa(s) = \left(\frac{\mathrm{d}x}{\mathrm{d}s} \right) \left(\frac{\mathrm{d}^2 y}{\mathrm{d}s^2} \right) - \left(\frac{\mathrm{d}^2 x}{\mathrm{d}s^2} \right) \left(\frac{\mathrm{d}y}{\mathrm{d}s} \right), \tag{6.1}$$

where s is the arc length. Furthermore, only the parallel regions are deemed to be governed by the vdW interaction energy E_{v}. The vdW interaction energies considered here include graphene–graphene interactions from the vertical lines throughout the curve C_3, 3 layers of graphene (including the layer on the horizontal axis) interacting with the substrate between x_2 and x_3, 2 layers of graphene interacting with the substrate between x_2 and x_4, and finally graphene–substrate interactions between x_1 and x_{end}. Hence, E_{v} is modelled by

$$\begin{aligned} E_{\mathrm{v}} = &-\epsilon_{\mathrm{gg}} \left[\int_{C_3} \mathrm{d}s + (y_2 - y_1) \right] - \epsilon_{3\mathrm{gs}}(x_3 - x_2) - \epsilon_{2\mathrm{gs}}(x_4 - x_2) \\ &- \epsilon_{\mathrm{gs}}(x_{\mathrm{end}} - x_1), \end{aligned}$$

where ϵ_{gg} and ϵ_{gs} are positive constants which respectively denote the graphene–graphene and graphene–substrate vdW interaction energies, and $\epsilon_{N\mathrm{gs}}$ represents the strengths of the vdW interaction energy when N layers of graphene

interact with the substrate, for $N = 2, 3$. Taking the elastic bending energy E_{e} and the vdW interaction energy E_{v} together, the total energy E_{tot} for the collapsed wrinkle may be written as a sum of three independent energy components as follows

$$E_{\mathrm{tot}} = E_{\mathrm{e}} + E_{\mathrm{v}} = E_2 + E_3 + E_4,$$

with

$$\begin{aligned} E_2 &= \int_{C_2} 2\gamma\kappa^2 \,\mathrm{d}s - \epsilon_{\mathrm{gs}}(x_{\mathrm{end}} - x_1) - \epsilon_{\mathrm{gg}}(y_2 - y_1), \\ E_3 &= \int_{C_3} \left(\gamma\kappa_{\mathrm{tot}}^2 - \epsilon_{\mathrm{gg}}\right) \mathrm{d}s - \epsilon_{3\mathrm{gs}}(x_3 - x_2), \\ E_4 &= \int_{C_4} \gamma\kappa^2 \,\mathrm{d}s - \epsilon_{2\mathrm{gs}}(x_4 - x_2). \end{aligned}$$

Additionally, the total arc length L_{tot} may be calculated by

$$L_{\mathrm{tot}} = 2\left(L_{C_2} + y_2 - y_1\right) + L_{C_3} + L_{C_4} + \left(x_3 - x_2\right) + \left(x_4 - x_2\right), \tag{6.2}$$

where L_{C_2}, L_{C_3}, and L_{C_4} denote the arc length of the curves C_2, C_3, and C_4, respectively. In Section 6.3, variational calculus is employed to determine the extremal curves for E_2, E_3, and E_4 independently.

6.3 Variational calculus

6.3.1 Extremal for E_2

In this subsection, the aim is to determine a solution curve for C_2 which produces a minimum value for the energy functional E_2. For convenience, the vdW interaction energy at each endpoint is subtracted and the reflective symmetry of the curve C_2 is exploited to reduce the energy functional E_2 to

$$\bar{E}_2 = \int_0^{L_{C_2}} \gamma\kappa^2 \,\mathrm{d}s + \epsilon_{\mathrm{gs}} x_1 + \epsilon_{\mathrm{gg}} y_1,$$

subject to the boundary conditions, at $s = 0$:

$$x = \delta_{\mathrm{gg}}, \quad y = y_1, \quad \mathrm{d}x/\mathrm{d}s = 0, \quad \mathrm{d}y/\mathrm{d}s = -1,$$

and at the endpoint $s = L_{C_2}$:

$$x = x_1, \quad y = 0, \quad \mathrm{d}x/\mathrm{d}s = 1, \quad \mathrm{d}y/\mathrm{d}s = 0,$$

where the endpoints x_1 and y_1 are not prescribed but determined as a part of the solution. This functional represents a variational problem with two dependent variables and natural boundary conditions, that is largely equivalent to that considered by Cox et al. [87], as a part of modelling the self-adhered graphene wrinkle. Therefore, their solution is employed here using the coordinate transformation

$$\mathrm{d}s = \sqrt{1 + (\mathrm{d}y/\mathrm{d}x)^2}\,\mathrm{d}x\,.$$

The obtained parametric solution depends on the following functions

$$x^{\star}_{C_2}(\phi) = 2\alpha_2 (\sin\psi_2)^{1/2} \left[\cos\psi_2\, E(\phi, k) - \sin\psi_2 (\cos 2\phi)^{1/2}\right],$$
$$y^{\star}_{C_2}(\phi) = 2\alpha_2 (\sin\psi_2)^{1/2} \left[\cos\psi_2 (\cos 2\phi)^{1/2} + \sin\psi_2\, E(\phi, k)\right],$$

where $E(\phi, k)$ denotes the elliptic integral of the second kind with the associated elliptic modulus $k = \sqrt{2}$, $\alpha_2 = \sqrt{\gamma/\epsilon_{\mathrm{gg}}}$, and

$$\psi_2 = \cos^{-1}\left(\frac{\epsilon_{\mathrm{gs}}}{\sqrt{\epsilon_{\mathrm{gg}}^2 + \epsilon_{\mathrm{gs}}^2}}\right).$$

Applying the boundary conditions, the curve is presented in parametric form as

$$x_{C_2}(\phi) = x^{\star}_{C_2}(\phi) - x^{\star}_{C_2}(\psi_2/2 - \pi/4) + \delta_{\mathrm{gg}},$$
$$y_{C_2}(\phi) = y^{\star}_{C_2}(\psi_2/2) - y^{\star}_{C_2}(\phi),$$

where ϕ ranges from $(\psi_2/2 - \pi/4)$ to $(\psi_2/2)$. The height of the curve C_2, h_{C_2} may be calculated by $h_{C_2} = y_1 = y_{C_2}(\psi_2/2 - \pi/4)$.

The method from Ref. [87] is now followed, and an expression for the arc length of the curve C_2 is given in terms of incomplete elliptic integrals of the first kind as

$$L_{C_2} = 2\alpha_2 (\sin\psi_2)^{1/2} \left[F(\psi_2/2, k) - F(\psi_2/2 - \pi/4, k)\right]. \tag{6.3}$$

Similarly, the total elastic energy inherent in C_2 is expressed in terms of incomplete elliptic integrals of the second kind as

$$E_{C_2} = \frac{2\gamma}{\alpha_2 (\sin\psi_2)^{1/2}} \left[E(\psi_2/2, k) - E(\psi_2/2 - \pi/4, k)\right]. \tag{6.4}$$

6.3.2 Extremal for E_3

In this subsection, the aim is to determine a solution curve for C_3 which produces a minimum value for the energy functional E_3 given by

$$E_3 = \int_{C_3} \left(\gamma\kappa_{\text{tot}}^2 - \epsilon_{\text{gg}}\right) \mathrm{d}s - \epsilon_{3\text{gs}}(x_3 - x_2).$$

We note that E_3 linearly depends on x_3, which plays no role in determining the extremal curve for E_3; hence, it is assumed that $x_3 = x_2$ for simplicity. Therefore, the energy functional to be minimised is now given by

$$E_3 = \int_{C_3} \left(\gamma\kappa_{\text{tot}}^2 - \epsilon_{\text{gg}}\right) \mathrm{d}s\,. \tag{6.5}$$

With reference to (6.2), the functional (6.5) must satisfy the arc length constraint

$$\int_{C_3} \mathrm{d}s = L_{\text{tot}} - L_{C_4} - (x_4 - x_2) - 2\left(L_{C_2} + y_2 - y_1\right).$$

Incorporating this constraint introduces a Lagrange multiplier λ_3 into the functional (6.5) which becomes

$$E_3 = \int_{C_3} \left(\gamma\kappa_{\text{tot}}^2 + \lambda_3 - \epsilon_{\text{gg}}\right) \mathrm{d}s\,.$$

The extremal curves for E_3 are determined based on the mid-line, the dotted line in Fig. 6.1(b), so it is convenient to write the previous expression as

$$\bar{E}_3 = \frac{E_3}{\lambda} = \int_0^{L_\mathrm{m}} \Big(\frac{\gamma}{\lambda}\kappa_\mathrm{tot}^2 + 1\Big)\,\mathrm{d}s\,, \tag{6.6}$$

where $\lambda = \lambda_3 - \epsilon_\mathrm{gg}$ and L_m denotes the length of the mid-line. The variational problem (6.6) must satisfy the boundary conditions, at $s = 0$,

$$x = 0, \quad y = y_2, \quad \mathrm{d}x/\mathrm{d}s = 0, \quad \mathrm{d}y/\mathrm{d}s = 1,$$

and at the endpoint $s = L_\mathrm{m}$,

$$x = x_2, \quad y = 3\delta_\mathrm{gg}, \quad \mathrm{d}x/\mathrm{d}s = 1, \quad \mathrm{d}y/\mathrm{d}s = 0,$$

where the x–coordinate of the endpoint x_2 is not prescribed. It is natural to assume that the distance $y_2 - y_1$ vanishes when the self-adhered wrinkle folds over. Then for this model to be physically meaningful, we require $y_2 = y_1$, which is determined in Subsection 6.3.1.

The total squared curvature for the curve C_3 is denoted by κ_tot^2 and is the sum of the squared curvature of the outer layer κ_o^2, and the inner layer κ_i^2. Taking the mid-line curvature to be $\kappa_\mathrm{m}(s) = \kappa(s)$ as defined by (6.1), the curvature of the outer and inner layers may be written in terms of κ_m as

$$\kappa_\mathrm{o/i} = \frac{|\kappa_\mathrm{m}|}{1 \pm \delta_\mathrm{gg}|\kappa_\mathrm{m}|}.$$

We mention that a general expression for the total squared curvature κ_tot^2 of folded N–layer graphene has been derived in Section 4.2, and is given by

$$\kappa_\mathrm{tot}^2 \approx N\kappa_\mathrm{m}^2 + N(N^2-1)\delta_\mathrm{gg}^2\kappa_\mathrm{m}^4 + N(N^2-1)(N^2-7/3)\delta_\mathrm{gg}^4\kappa_\mathrm{m}^6. \tag{6.7}$$

Hence, that expression may be exploited in this problem by making the substitution $N = 2$, which yields

$$\kappa_\mathrm{tot}^2 \approx 2\kappa_\mathrm{m}^2 + 6\delta_\mathrm{gg}^2\kappa_\mathrm{m}^4 + 10\delta_\mathrm{gg}^4\kappa_\mathrm{m}^6. \tag{6.8}$$

Inserting the expression in (6.8) into (6.6) yields the functional to be minimised.

The functional $\bar{E}_3$ is first nondimensionalised by making a change of variables such that $x = \alpha_3 X$ and $y = \alpha_3 Y$ with a scaling factor $\alpha_3 = \sqrt{2\gamma/\lambda}$. The mid-line's nondimensional curvature is then written as $\hat{\kappa}_{\mathrm{m}}(S) = \dot{X}\ddot{Y} - \ddot{X}\dot{Y}$, with the dot indicating the derivative with respect to the nondimensional arc length S. In terms of the new variables, $\kappa_{\mathrm{m}} = \hat{\kappa}_{\mathrm{m}}/\alpha_3$ and $\mathrm{d}s = \alpha_3\,\mathrm{d}S$. Thus, the nondimensional energy functional (6.6) becomes

$$\hat{E}_3 = \int_0^{\hat{L}_{\mathrm{m}}} \left(\hat{\kappa}_{\mathrm{m}}^2 + \mu\hat{\kappa}_{\mathrm{m}}^4 + \rho\hat{\kappa}_{\mathrm{m}}^6 + 1\right) \mathrm{d}S\,, \tag{6.9}$$

with the parameters

$$\mu = \frac{3\lambda\delta_{\mathrm{gg}}^2}{2\gamma}, \quad \text{and} \quad \rho = \frac{5\lambda^2\delta_{\mathrm{gg}}^4}{4\gamma^2}.$$

Following our usual notation, the integrand of the functional (6.9) is denoted by F, namely

$$F(\hat{\kappa}_{\mathrm{m}}) = \hat{\kappa}_{\mathrm{m}}^2 + \mu\hat{\kappa}_{\mathrm{m}}^4 + \rho\hat{\kappa}_{\mathrm{m}}^6 + 1, \tag{6.10}$$

which, through the definition of $\hat{\kappa}_{\mathrm{m}}$, clearly depends on the first and second derivatives of the new variables X and Y. Following the same steps as in Section 4.3, we may use variational calculus to derive

$$\ddot{X}F_{\ddot{X}} + \ddot{Y}F_{\ddot{Y}} - F = -\psi_3\dot{Y}, \tag{6.11}$$

where ψ_3 is a constant of integration. On substitution of (6.10) into (6.11), we obtain

$$\hat{\kappa}_{\mathrm{m}}^2(S) + 3\mu\hat{\kappa}_{\mathrm{m}}^4(S) + 5\rho\hat{\kappa}_{\mathrm{m}}^6(S) = 1 - \psi_3\dot{Y}.$$

For convenience, we now make the change of variables $\mathrm{d}S = (X'^2 + Y'^2)^{1/2}\,\mathrm{d}\theta$, with the prime indicating the derivative with respect to θ. Thus, we may

derive

$$\hat{\kappa}_{\mathrm{m}}^2(\theta) + 3\mu\hat{\kappa}_{\mathrm{m}}^4(\theta) + 5\rho\hat{\kappa}_{\mathrm{m}}^6(\theta) = 1 - \frac{\psi_3 Y'}{(X'^2 + Y'^2)^{1/2}}.$$

Solving this expression for $\hat{\kappa}_{\mathrm{m}}$ yields the curvature expression for the mid-line, and following the same steps as in Section 4.3.3, we may deduce that

$$\hat{\kappa}_{\mathrm{m}}(\theta) = \pm \left[\left(\sqrt{\frac{q^2}{4} + \frac{p^3}{27}} - \frac{q}{2} \right)^{1/3} - \frac{p}{3} \left(\sqrt{\frac{q^2}{4} + \frac{p^3}{27}} - \frac{q}{2} \right)^{-1/3} - \frac{\mu}{5\rho} \right]^{1/2}, \tag{6.12}$$

with

$$p = \frac{5\rho - 3\mu^2}{(5\rho)^2}, \quad \text{and} \quad q(\theta) = \mu\,\frac{2\mu^2 - 5\rho}{(5\rho)^3} - \frac{1}{5\rho}\left(1 - \psi_3 \sin\theta\right).$$

While we propose to model a curve that is structurally similar to the top-half of folded 2–layer graphene, we mention that the curvature expression (6.12) has also been employed in Section 5.3 to model the fold of unsupported N–layer graphene.

Taking the sign of the curvature into account, the mid-line is derived parametrically by solving the differential equations

$$X' = \frac{\cos\theta}{\hat{\kappa}_{\mathrm{m}}(\theta)}, \quad Y' = \frac{\sin\theta}{\hat{\kappa}_{\mathrm{m}}(\theta)}.$$

The part of C_3 with negative curvature is given by

$$X_{C_3^-}(\theta) = \int_{-\pi/2}^{\theta} \frac{\cos\tilde{\theta}}{\hat{\kappa}_{\mathrm{m}}(\tilde{\theta})}\,\mathrm{d}\tilde{\theta}\,, \quad Y_{C_3^-}(\theta) = -\int_{-\pi/2}^{\theta} \frac{\sin\tilde{\theta}}{\hat{\kappa}_{\mathrm{m}}(\tilde{\theta})}\,\mathrm{d}\tilde{\theta}\,,$$

where $\theta \in [-\pi/2, \theta_3]$ and $\theta_3 = \sin^{-1}(1/\psi_3)$ denotes the point where the curvature changes sign. The positive curvature part of C_3 where $\theta \in [0, \theta_3]$ is given by

$$X_{C_3^+}(\theta) = X_{C_3^-}(\theta_3) - \int_{\theta_3}^{\theta} \frac{\cos\tilde{\theta}}{\hat{\kappa}_{\mathrm{m}}(\tilde{\theta})}\,\mathrm{d}\tilde{\theta}\,,$$
$$Y_{C_3^+}(\theta) = Y_{C_3^-}(\theta_3) + \int_{\theta_3}^{\theta} \frac{\sin\tilde{\theta}}{\hat{\kappa}_{\mathrm{m}}(\tilde{\theta})}\,\mathrm{d}\tilde{\theta}\,.$$

The solutions of the mid-line are now exploited to obtain the solutions of the outer/inner layer as

$$X_{\mathrm{o/i}}(\theta) = X(\theta) \mp \frac{\delta_{\mathrm{gg}}}{\alpha_3}\left(\frac{Y'}{\sqrt{X'^2+Y'^2}}\right),$$
$$Y_{\mathrm{o/i}}(\theta) = Y(\theta) \pm \frac{\delta_{\mathrm{gg}}}{\alpha_3}\left(\frac{X'}{\sqrt{X'^2+Y'^2}}\right),$$

where $X(\theta)$ and $Y(\theta)$ describe the mid-line. Recall that $x = \alpha_3 X$ and $y = \alpha_3 Y$, and thus the dimensional solutions may be achieved through scaling these solutions by $\alpha_3 = \sqrt{2\gamma/\lambda}$. The maximum height of the curve C_3, h_{C_3} corresponds to the maximum height of the outer layer, which occurs in the negative curvature part of C_3 at $\theta = 0$. Thus, this height is calculated by $h_{C_3} = \alpha_3\, Y_{C_3^-}(0) + \delta_{\mathrm{gg}}$.

The arc length of the curve C_3 is calculated as the sum of the arc length of the outer and the inner layer, that is

$$L_{C_3} = L_{\mathrm{o}} + L_{\mathrm{i}} = \int_{C_3} \mathrm{d}s_{\mathrm{o}} + \int_{C_3} \mathrm{d}s_{\mathrm{i}}\,. \tag{6.13}$$

Since $\mathrm{d}s = \mathrm{d}\theta/\kappa_{\mathrm{m}}$, we may write

$$\mathrm{d}s_{\mathrm{o/i}} = \frac{\mathrm{d}\theta}{\kappa_{\mathrm{o/i}}} = (1 \pm \delta_{\mathrm{gg}}|\kappa_{\mathrm{m}}|)\,\mathrm{d}s\,,$$

with $\kappa_{\mathrm{m}} = \hat{\kappa}_{\mathrm{m}}/\alpha_3$ and $\hat{\kappa}_{\mathrm{m}}$ is given earlier by (6.12). Therefore, equation (6.13) may be rewritten as

$$L_{C_3} = \int_{C_3} (1 + \delta_{\mathrm{gg}}|\kappa_{\mathrm{m}}|)\,\mathrm{d}s + \int_{C_3} (1 - \delta_{\mathrm{gg}}|\kappa_{\mathrm{m}}|)\,\mathrm{d}s = 2\int_{C_3} \mathrm{d}s = 2L_{\mathrm{m}},$$

and upon changing the integration variable using the substitution $\mathrm{d}s = \mathrm{d}\theta/\kappa_{\mathrm{m}}$, the arc length of the curve C_3 may be calculated as

$$L_{C_3} = 2\left[\int_{-\pi/2}^{\theta_3} \frac{\mathrm{d}\theta}{\kappa_{\mathrm{m}}(\theta)} - \int_{\theta_3}^{0} \frac{\mathrm{d}\theta}{\kappa_{\mathrm{m}}(\theta)}\right]. \tag{6.14}$$

The total energy inherent in the curve C_3 includes the elastic energy cost of bending the outer layer E_o and the inner layer E_i, as well as the graphene–graphene vdW interaction energy along the bended region. Therefore, the total energy inherent in the curve C_3, E_{C_3} is given by

$$E_{C_3} = E_\mathrm{o} + E_\mathrm{i} - \epsilon_{\mathrm{gg}} L_\mathrm{m}, \tag{6.15}$$

where

$$E_{\mathrm{o/i}} = \gamma \int_{C_3} \kappa_{\mathrm{o/i}}^2 \, \mathrm{d}s_{\mathrm{o/i}} = \gamma \int_{C_3} \kappa_{\mathrm{o/i}} \, \mathrm{d}\theta = \gamma \left[\int_{-\pi/2}^{\theta_3} \kappa_{\mathrm{o/i}}(\theta) \, \mathrm{d}\theta - \int_{\theta_3}^{0} \kappa_{\mathrm{o/i}}(\theta) \, \mathrm{d}\theta \right],$$

and we recall that

$$\kappa_{\mathrm{o/i}} = \frac{|\kappa_\mathrm{m}|}{1 \pm \delta_{\mathrm{gg}} |\kappa_\mathrm{m}|}.$$

6.3.3 Extremal for E_4

In this subsection, the aim is to determine a solution curve for C_4 which produces a minimum value for the energy functional E_4 given by

$$E_4 = \int_{C_4} \gamma \kappa^2 \, \mathrm{d}s - \epsilon_{\mathrm{2gs}} (x_4 - x_2). \tag{6.16}$$

By the same reasoning as in Subsection 6.3.2, the functional E_4 must satisfy the arc length constraint L_{E_4} given by

$$L_{E_4} = \int_{C_4} \mathrm{d}s + (x_4 - x_2) = L_\mathrm{tot} - 2L_{C_2} - L_{C_3}.$$

As before, this constraint introduces a Lagrange multiplier λ_4 into the functional (6.16) which becomes

$$E_4 = \int_{C_4} \left(\gamma \kappa^2 + \lambda_4 \right) \mathrm{d}s + (\lambda_4 - \epsilon_{\mathrm{2gs}}) \, (x_4 - x_2).$$

Upon using the substitution

$$x_4 - x_2 = L_{E_4} - \int_{C_4} \mathrm{d}s \, ,$$

we may derive

$$E_4 = \int_{C_4} \left(\gamma\kappa^2 + \epsilon_{2\mathrm{gs}}\right) \mathrm{d}s + \left(\lambda_4 - \epsilon_{2\mathrm{gs}}\right) L_{E_4}.$$

Determining the extremal curve for E_4 is independent of the Lagrange multiplier λ_4, and thus $\lambda_4 = \epsilon_{2\mathrm{gs}}$ can be used to simplify our calculations. Then the functional to be minimised is now of the form

$$E_4 = \int_0^{L_{C_4}} \left(\gamma\kappa^2 + \epsilon_{2\mathrm{gs}}\right) \mathrm{d}s\,,$$

or, equivalently

$$\bar{E}_4 = \frac{E_4}{\epsilon_{2\mathrm{gs}}} = \int_0^{L_{C_4}} \left(\frac{\gamma}{\epsilon_{2\mathrm{gs}}}\kappa^2 + 1\right) \mathrm{d}s\,,$$

subject to the boundary conditions, at $s = 0$,

$$x = x_3, \quad y = 4\delta_{\mathrm{gg}}, \quad \mathrm{d}x/\mathrm{d}s = 1, \quad \mathrm{d}y/\mathrm{d}s = 0,$$

and at the endpoint $s = L_{C_4}$,

$$x = x_4, \quad y = 2\delta_{\mathrm{gg}}, \quad \mathrm{d}x/\mathrm{d}s = -1, \quad \mathrm{d}y/\mathrm{d}s = 0,$$

where x_3 is prescribed in this problem and its value is determined according to the assumed total arc length of the graphene sheet, but the x–coordinate of the endpoint x_4 is not prescribed.

Compared to the equivalent expression (6.7), in Section 6.3.2, the total squared curvature is simpler here and given by $\kappa_{\mathrm{tot}}^2 = \kappa^2$, since $N = 1$. We therefore follow the same steps as in Section 6.3.2 and derive an expression for the nondimensionalised curvature as

$$\hat{\kappa}(\theta) = \pm\left(1 - \psi_4 \sin\theta\right)^{1/2}, \tag{6.17}$$

where ψ_4 is a constant of integration. While we propose to model a curve that is structurally similar to folding supported single-layer graphene, we

comment that the curvature expression (6.17) has been also used in Section 4.3.1 to model the fold of N–layer graphene stack supported by SiO_2 substrate. The substitution $\theta = 2\phi - \pi/2$ is then made, and the parametric solutions are written in terms of the functions $g_1(\phi)$ and $g_2(\phi)$, as given by (4.27). Considering the arbitrary constant ψ_4, the parameters in (4.28) are now given by

$$A = \frac{2\,(1+\psi_4)^{1/2}}{\psi_4}, \quad B = \frac{1}{1+\psi_4}, \quad k = \left(\frac{2\psi_4}{1+\psi_4}\right)^{1/2}.$$

We now propose a solution that starts from X_3 with $\phi = \pi/4$, proceeds clockwise and ends at X_4 with $\phi = -\pi/4$. The first part of this solution has a positive curvature, while the second part has a negative curvature. These two parts are bounded by a point with zero curvature corresponding to $\phi_4 = \sin^{-1}(1/k)$. For the positive curvature portion of C_4, ϕ varies in the range $[\pi/4, \phi_4]$ and the parametric solution is

$$X_{C_4^+}(\phi) = X_3 + g_1(\pi/4) - g_1(\phi),$$
$$Y_{C_4^+}(\phi) = \frac{4\delta_{\text{gg}}}{\alpha_4} + g_2(\pi/4) - g_2(\phi).$$

For the negative curvature portion of C_4, ϕ varies in the range $[-\pi/4, \phi_4]$ and the parametric solution is given by

$$X_{C_4^-}(\phi) = X_3 + g_1(\pi/4) + g_1(\phi),$$
$$Y_{C_4^-}(\phi) = \frac{4\delta_{\text{gg}}}{\alpha_4} + g_2(\pi/4) + g_2(\phi) - 2g_2(\phi_4).$$

As in Section 6.3.2, scaling the parametric solutions by $\alpha_4 = \sqrt{\gamma/\epsilon_{2\text{gs}}}$ produces the dimensional solutions for C_4. It is noted that the maximum height of the curve C_4, h_{C_4} occurs in the negative curvature part of C_4 where $\phi = \pi/4$, and thus it is given by $h_{C_4} = \alpha_4\, Y_{C_4^-}(\pi/4)$. The value of ψ_4 can be calculated numerically such that the endpoint condition $y_{C_4^-}(-\pi/4) = 2\delta_{\text{gg}}$ is satisfied.

The arc length of the curve C_4 is now calculated as

$$L_{C_4} = \int_{C_4} \mathrm{d}s\,,$$

which after the substitution $\mathrm{d}s = \mathrm{d}\theta/\kappa = 2\,\mathrm{d}\phi/\kappa$ becomes

$$L_{C_4} = 2\left[\int_{-\pi/4}^{\phi_4} \frac{\mathrm{d}\phi}{\kappa(\phi)} - \int_{\phi_4}^{\pi/4} \frac{\mathrm{d}\phi}{\kappa(\phi)}\right], \tag{6.18}$$

where $\kappa = \hat{\kappa}/\alpha_4$ and $\hat{\kappa}$ is given earlier by (6.17). Thus, the arc length of the curve C_4 is represented by elliptic functions of the first kind as

$$L_{C_4} = 4\alpha_4\,(1+\psi_4)^{-1/2}\,F(\phi_4, k). \tag{6.19}$$

The total elastic energy inherent in the curve C_4 may be calculated using

$$E_{C_4} = \int_{C_4} \kappa^2\,\mathrm{d}s\,,$$

and a similar derivation as that used to calculate the arc length is applied, which yields

$$E_{C_4} = 4\gamma\,\alpha_4^{-1}\,(1+\psi_4)^{1/2}\,E(\phi_4, k). \tag{6.20}$$

The incomplete elliptic functions of the first and second kind are odd functions of ϕ as indicated by the relationship (2.40), and this property has been used to obtain (6.19)–(6.20). In the following section, specific substrate materials are adopted into the model and values for $\epsilon_{3\mathrm{gs}}$ and $\epsilon_{2\mathrm{gs}}$ are obtained from the LJ potential.

6.4 Substrate parameters

As mentioned in the Section 3.2, some metal(111) surfaces are shown to bind weakly on graphene such as Cu(111), while others are shown to bind strongly

such as Ni(111). Taking this into account, Cu(111) and Ni(111) are considered as example substrates in our variational model developed in Chapter 2 for graphene ripples. In addition, we mention that another variational model has been constructed for graphene arch-shaped and self-adhered wrinkles [87], where the authors have considered Cu(111) and Ni(111) substrates in their analysis. Continuing in this vein, this model is applied to study the behaviour of collapsed graphene wrinkles supported by Cu(111) or Ni(111) substrate. This approach also provides a good opportunity to exploit earlier work [87] and investigate the critical height of self-adhered wrinkles.

The strength of vdW interactions $\epsilon_{\rm gs}$ and the equilibrium distance $\delta_{\rm gs}$ for a single-layer graphene interacting with each considered substrate material have been reported in the literature [81]. However, the LJ potential is employed in this study to calculate values for the strengths of the vdW interaction energy $\epsilon_{N\rm gs}$, when N layers of graphene interact with the substrate, for $N = 2, 3$. The strengths of the vdW interaction energy $\epsilon_{N\rm gs}$ is approximated in this chapter such that each interaction between the top layer and the other layers below are accounted for along with the interaction between the top layer and the substrate. For instance, when calculating values for $\epsilon_{3\rm gs}$, we account for the interactions between two graphene layers at a distance $2\delta_{\rm gg}$, two graphene layers at a distance $4\delta_{\rm gg}$, and a graphene layer with the substrate at a distance $\delta_{\rm gs} + 4\delta_{\rm gg}$. Therefore, we may write a mathematical expression for $\epsilon_{N\rm gs}$ as

$$\epsilon_{N\rm gs} = \epsilon_{\rm gs}\left(\delta_{\rm gs} + (N-1)2\delta_{\rm gg}\right) + \sum_{j=1}^{N-1} \epsilon_{\rm gg}(j2\delta_{\rm gg}),$$

where $\epsilon_{\rm gg}(\varphi)$ and $\epsilon_{\rm gs}(\tilde{\varphi})$ are the graphene–graphene and graphene–substrate interaction energy at the distances $\varphi = j2\delta_{\rm gg}$, and $\tilde{\varphi} = \delta_{\rm gs} + (N-1)2\delta_{\rm gg}$, respectively.

Following the general approach given in Section 2.2.1, the graphene–graphene interaction energy is a surface–surface interaction, and therefore it may be modelled by

$$\epsilon_{\mathrm{gg}}(\varphi) = D_{\mathrm{g}}^2 \left(-\frac{\pi \mathcal{A}_{\mathrm{gg}}}{2\varphi^4} + \frac{\pi \mathcal{B}_{\mathrm{gg}}}{5\varphi^{10}} \right). \tag{6.21}$$

In this chapter, values for $\mathcal{A}_{\mathrm{gg}}$ and $\mathcal{B}_{\mathrm{gg}}$ are derived such that the parameters D_{g}, δ_{gg}, and ϵ_{gg} listed in Table 6.1, satisfy (6.21) and $[\mathrm{d}\epsilon_{\mathrm{gg}}/\mathrm{d}\varphi]_{\varphi=2\delta_{\mathrm{gg}}} = 0$. However, the graphene–substrate interaction is a surface–volume interaction, and therefore it may be modelled by

$$\epsilon_{\mathrm{gs}}(\tilde{\varphi}) = D_{\mathrm{g}} D_{\mathrm{s}} \left(-\frac{\pi \mathcal{A}_{\mathrm{gs}}}{6\tilde{\varphi}^3} + \frac{\pi \mathcal{B}_{\mathrm{gs}}}{45\tilde{\varphi}^9} \right). \tag{6.22}$$

Similarly, values for $\mathcal{A}_{\mathrm{gs}}$ and $\mathcal{B}_{\mathrm{gs}}$ are derived such that D_{s}, δ_{gs}, and ϵ_{gs} listed in Table 6.1, satisfy (6.22) and $[\mathrm{d}\epsilon_{\mathrm{gs}}/\mathrm{d}\tilde{\varphi}]_{\tilde{\varphi}=\delta_{\mathrm{gs}}} = 0$. Table 6.1 summarises the values for the parameters used in this work.

6.5 Results

Starting from the conformation of a self-adhered wrinkle with a gradually increasing height, the wrinkle may fold over at a certain height, which would form a collapsed wrinkle. In this study, two potential conformations for the collapsed wrinkle are considered, which are illustrated in Fig. 6.2. We first introduce Conformation A, which may form when the vertical layers of the self-adhered wrinkle are fully converted to a folded bilayer. We also consider Conformation B, which may form when these vertical layers are converted to a folded bilayer followed by a flat layers. Conformation A maximises the elastic energy, while B minimises the vdW energy. Taking into account that the minimum energy structure is energetically favourable, the energies of

these conformations are then compared and the length where each conformation becomes energetically favoured is obtained. It has been shown that the bending rigidity of graphene varies in the range 0.83–1.61 eV [15], and for comparison purposes, linearly spaced values are chosen from this range for γ, namely $\gamma = \{0.8, 1.0, 1.2, 1.4, 1.6\}$ eV.

The total arc length of the collapsed wrinkle is given by

$$L_{\text{tot}} = 2L_{C_2} + L_{C_3} + L_{C_4} + (x_3 - x_2) + (x_4 - x_2),$$

where expressions for L_{C_2}, L_{C_3}, and L_{C_4} are given by (6.3), (6.14), and (6.19), respectively. The total energy of the collapsed wrinkle is given by

$$E_{\text{tot}} = 2E_{C_2} + E_{C_3} + E_{C_4} - \epsilon_{3\text{gs}}(x_3 - x_2) - \epsilon_{2\text{gs}}(x_4 - x_2),$$

Table 6.1: Numerical values for the parameters of graphene–graphene interactions and graphene–substrate interactions (based on our calculations unless referenced).

Parameters	graphene–graphene, (z=g)	graphene–substrate, (z=s)	
		Cu(111)	Ni(111)
D_z	0.3812 (Å^{-2})	0.085 (Å^{-3})	0.091 (Å^{-3})
$\delta_{\text{g}z}$ (Å)	1.670 [90]	3.260 [81]	2.018 [81]
$\epsilon_{\text{g}z}$ (eV/Å^2)	0.0214 [90]	0.0132 [81]	0.0913 [81]
$A_{\text{g}z}$ (eV Å^6)	19.4456	40.4816	61.7489
$B_{\text{g}z}$ (eV Å^{12})	2.7×10^4	1.21×10^5	1.04×10^4
$\epsilon_{2\text{gs}}$ (eV/Å^2)	–	0.0238	0.0287
$\epsilon_{3\text{gs}}$ (eV/Å^2)	–	0.0243	0.0253

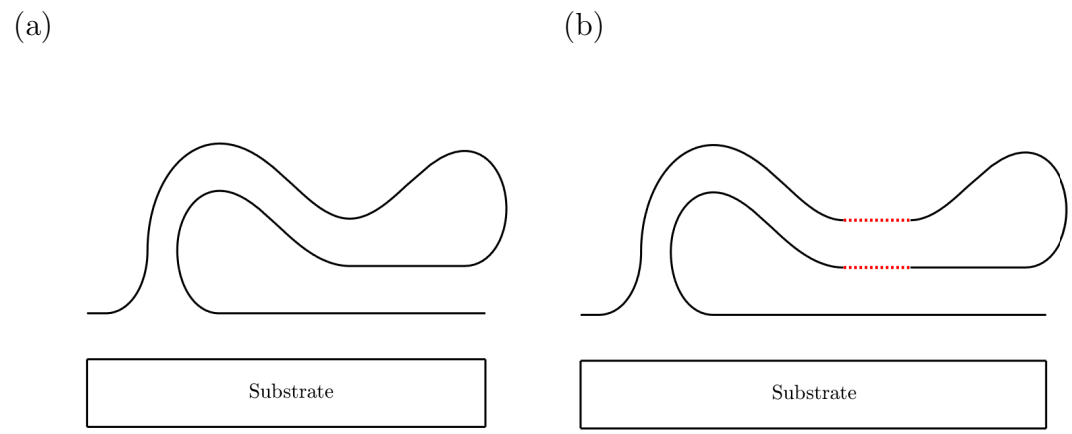

Figure 6.2: Schematic illustrating the structures of two potential conformations of collapsed wrinkles: (a) Conformation A and (b) Conformation B, with a zero and a non-zero distance following the folded bilayer, respectively.

where expressions for E_{C_2}, E_{C_3}, and E_{C_4} are given by (6.4), (6.15), and (6.20), respectively. The only unknown parameters are λ and ψ_3 which are numerically determined such that they satisfy the following equations:

$$y_{C_3^+}(0) = 3\delta_{\mathrm{gg}},$$
$$L_{C_3} = L_{\mathrm{tot}} - 2L_{C_2} - L_{C_4} - (x_3 - x_2) - (x_4 - x_2),$$

where L_{tot} is prescribed. The total arc length $L_{\mathrm{tot}}^{\mathrm{A}}$ and the total energy $E_{\mathrm{tot}}^{\mathrm{A}}$ of Conformation A are calculated using $x_2 = x_3$ where the total length is increased by increasing the curve C_3. On the other hand, the total arc length $L_{\mathrm{tot}}^{\mathrm{B}}$ and the total energy $E_{\mathrm{tot}}^{\mathrm{B}}$ of B are calculated assuming that $x_2 < x_3$, where the total length is increased by lengthening the flat section $(x_3 - x_2)$.

In an ideal setting, the wrinkle would not produce the flat section until the curve C_3 reaches an optimal length. The energies of the two potential conformations have an equal gradient (equal energy as shown in Fig. 6.4) at the transition length; hence, the initial length for which Conformation B

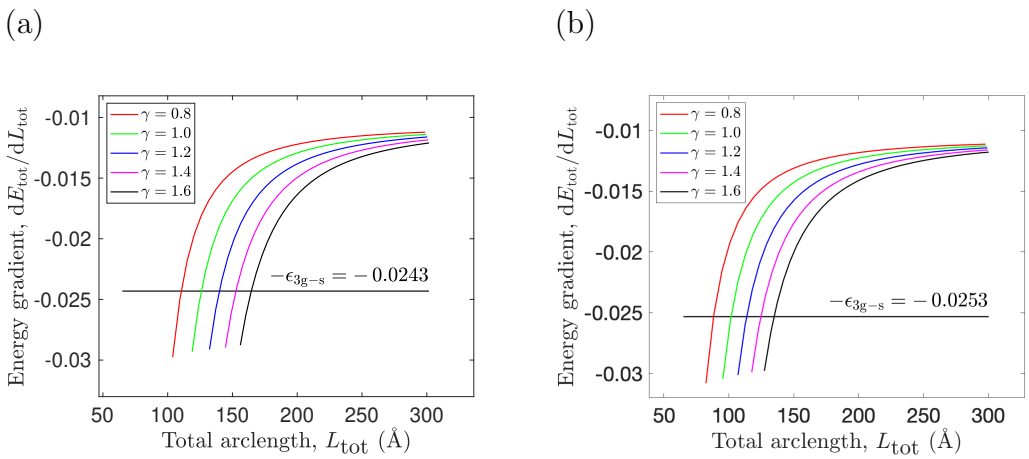

Figure 6.3: Energy gradients as a function of the total arc length L_{tot} of collapsed wrinkles supported by: (a) Cu(111) substrate, and (b) Ni(111) substrate. The coloured lines denote the energy gradients for Conformation A and the black line denotes the energy gradient for B, where the intersection point gives the length L_{B} for each value of γ.

produces lower energy L_{B} may be determined by numerically solving

$$\frac{\mathrm{d}E^{\text{A}}_{\text{tot}}(\lambda, \psi_3)}{\mathrm{d}L^{\text{A}}_{\text{tot}}(\lambda, \psi_3)} = \frac{\mathrm{d}E^{\text{B}}_{\text{tot}}(x_3)}{\mathrm{d}L^{\text{B}}_{\text{tot}}(x_3)} = -\epsilon_{3\text{gs}}.$$

In Fig. 6.3, the energy gradient for each conformation is plotted as a function of the total length L_{tot} where the intersection point denotes the starting length of Conformation B L_{B}, meaning that the collapse wrinkle starts producing the flat region.

We also investigate the critical height of self-adhered wrinkles through an energy comparison. A mathematical model has previously been developed for the self-adhered wrinkle [87], and its geometry is also presented in Fig. 6.1(a) for convenience. The total arc length of the self-adhered wrinkle $L^{\text{s}}_{\text{tot}}$ is derived in Ref. [87] as

$$L^{\text{s}}_{\text{tot}} = 2\left[L_{C_1} + L_{C_2} + (y_2 - y_1)\right],$$

and the total energy of the self-adhered wrinkle $E_{\text{tot}}^{\text{s}}$ is given by

$$E_{\text{tot}}^{\text{s}} = 2\,(E_{C_1} + E_{C_2}) - \epsilon_{\text{gg}}(y_2 - y_1),$$

where expressions for L_{C_1} and E_{C_1} are given in Ref. [87]. The value of y_1 is determined from a natural boundary condition, but the value of y_2 is varied in order to obtain the critical length L_{crit} for which the self-adhered wrinkle reaches the critical height h_{crit}.

Given that the minimum energy structure is energetically favourable, the comparison made in Fig. 6.4 shows that Conformation A of the collapsed wrinkle is unachievable since there are always other conformations with lower energies based on the parameters used in this study. However, it is useful in determining L_{B}, the initial length of Conformation B. The highlighted intersection point in Fig. 6.4 corresponds to the critical length of the self-adhered wrinkle before it folds and follows Conformation B. Fig. 6.5 illustrates the energy profiles for different bending rigidities and clearly indicates the critical lengths. Once the critical length L_{crit} is known, we may use the corresponding value of y_2 and utilise the work by Cox et al. [87], to calculate h_{crit} as

$$h_{\text{crit}} = y_2 + 2y_{C_1}^{\star}(-\pi/4) - y_{C_1}^{\star}(\psi_1/2) - y_{C_1}^{\star}(\psi_1/2 - \pi/4),$$

and the definitions of $y_{C_1}^{\star}$ and ψ_1 are given in Ref. [87].

Table 6.2 presents numerical values for the heights of collapsed wrinkles and the critical height h_{crit} of self-adhered wrinkles with the corresponding critical length L_{crit} and the critical energy E_{crit}. The bending rigidity of graphene $\gamma = 1.2 \pm 0.4\,\text{eV}$ is used in the analysis for comparison purposes. We find that self-adhered wrinkles adopt larger heights when supported by Cu(111) substrate rather than Ni(111) substrate for a fixed value of γ from the given range. Despite the substrate materials used in each study, these

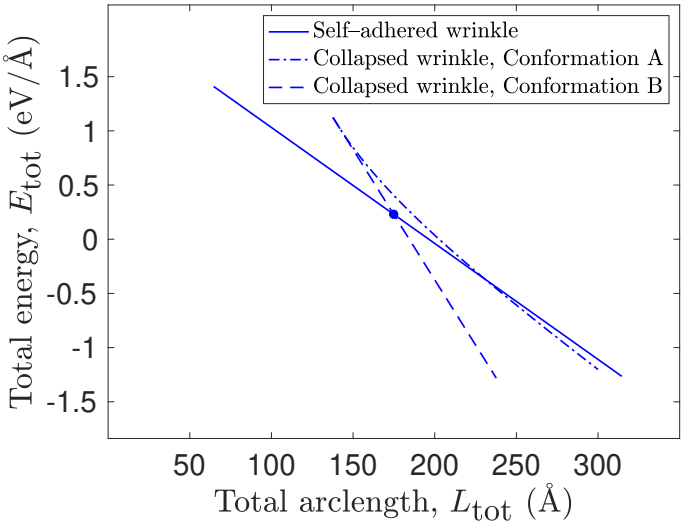

Figure 6.4: The behaviour of the total energy E_{tot} as a function of the total arc length L_{tot} for different wrinkle configurations with bending rigidity $\gamma = 1.2\,\text{eV}$ supported by Cu(111) substrate. The marked point denotes the critical length L_{crit} where the self-adhered wrinkle folds and follows Conformation B.

values correlate favourably with earlier experimental and theoretical studies which are summarised in Table 6.3. The predicted profiles of collapsed graphene wrinkles supported on Cu(111) and Ni(111) substrate are shown in Fig. 6.6, with $L_{\text{tot}} = L_{\text{crit}}$ as indicated in Fig. 6.5. Also for comparison purposes, the total arc length $L_{\text{tot}} = 180\,\text{Å}$ and $\gamma = 1.2\,\text{eV}$ are fixed to examine the effects of each substrate on the conformation of collapsed graphene wrinkles, as presented in Fig. 6.7. It is concluded that Ni(111) substrate leads to lower aspect ratio wrinkles compared to Cu(111) substrate, which may be justified by the stronger graphene–Ni(111) binding energy as compared with that of the graphene–Cu(111) substrate.

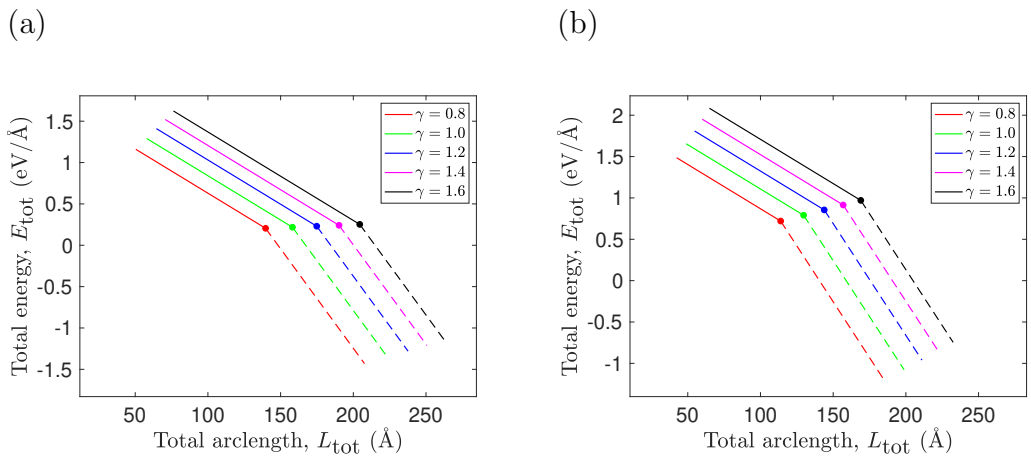

Figure 6.5: The behaviour of the total energy E_{tot} as a function of the total arc length L_{tot} for self-adhered wrinkles (solid lines) and Conformation B of collapsed wrinkles (dashed lines) supported by: (a) Cu(111) substrate, and (b) Ni(111) substrate. The marked points denote the critical lengths L_{crit} where self-adhered wrinkles fold and follow Conformation B.

6.6 Conclusion

In this chapter, a continuous approach is applied to construct a mathematical model for collapsed graphene wrinkles induced by folding standing self-adhered graphene wrinkles. The shape of the wrinkle is divided into three arcs with transition lines. Based on the elastic and vdW interaction energies, the total energy of the system is derived as a sum of three independent energy components. For each energy component, the calculus of variations is employed to minimise the energy functional and obtain expressions for the curvatures which are used to derive parametric solutions for each curve. Both copper and nickel substrates are considered in the analysis, and the LJ potential is applied to model the strengths of vdW interactions when two or three graphene layers interact with the substrate.

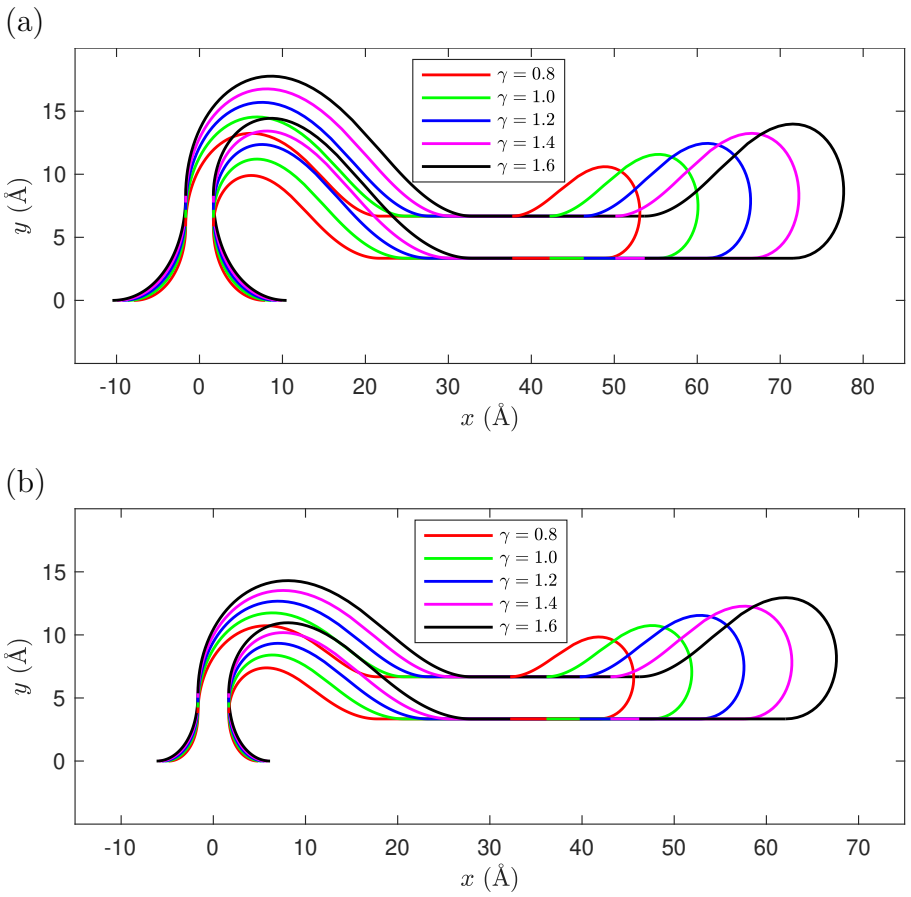

Figure 6.6: The conformation of collapsed wrinkles supported on: (a) Cu(111), and (b) Ni(111) substrate for different bending rigidities with $L_{\text{tot}} = L_{\text{crit}}$.

Table 6.2: Numerical values for the heights of collapsed wrinkles (Å), and the critical height of self-adhered wrinkles h_{crit} (Å) with the corresponding L_{crit} (Å) and E_{crit} (eV/Å) where the bending rigidity $\gamma = 1.2 \pm 0.4\,\text{eV}$.

Wrinkle	property	substrate	
		Cu(111)	Ni(111)
self-adhered	L_{crit}	175 ± 32	144 ± 28
	h_{crit}	79.6 ± 14.7	66.5 ± 12.7
	E_{crit}	0.230 ± 0.024	0.855 ± 0.123
collapsed	h_{C_2}	7.2 ± 1.2	4.7 ± 0.8
	h_{C_3}	15.7 ± 2.3	12.7 ± 1.8
	h_{C_4}	12.4 ± 1.7	11.5 ± 1.5

Table 6.3: Summary for some values for the critical height h_{crit} and the critical length L_{crit} of self-adhered wrinkles that have been reported in the literature.

Reference	h_{crit} (Å)	L_{crit} (Å)	Substrate	Study
Ref. [38]	60	–	SiO_2/Si	Experiment
Ref. [6]	110	–	Cu(111)	Experiment
Ref. [88]	101.5	–	SiO_2/Si	Experiment
Ref. [89]	50	–	SiO_2/Si	Experiment
Ref. [38]	84	163	SiO_2/Si	Theory
Ref. [6]	76	–	Cu(111)	Theory
Ref. [4]	69	155	Ignored	Theory

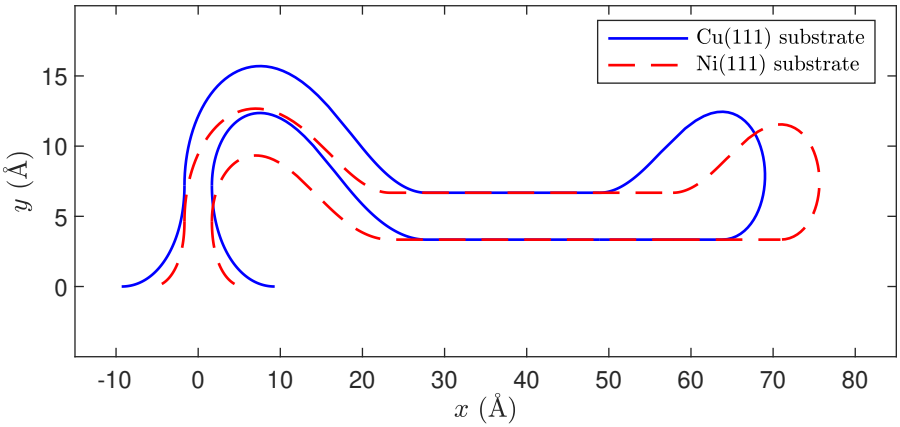

Figure 6.7: The conformation of collapsed wrinkles supported on Cu(111) and Ni(111) substrate with fixed arc length $L_{\text{tot}} = 180\,\text{Å}$ and bending rigidity $\gamma = 1.2\,\text{eV}$.

Two potential conformations for the collapsed wrinkle are investigated, along with the self-adhered wrinkle. Through an energy comparison between these configurations, the length where each configuration becomes energetically favoured is predicted. For collapsed wrinkles, the analysis of this study demonstrates that the folded bilayer is always followed by a flat region. For self-adhered wrinkles, the critical transition height is calculated exploiting an earlier solution that was derived for self-adhered wrinkles. The calculated critical heights are consistent with earlier experimental and theoretical results reported in the literature.

6.7 Nomenclature

Symbol	Description
$\dot{\square}$	derivatives of $\square$ with respect to S
$\square'$	derivatives of $\square$ with respect to θ
L_{tot}	the approximate total arc length of the wrinkle
$2\delta_{\mathrm{gg}}$	the graphene–graphene equilibrium distance
δ_{gs}	the graphene–substrate equilibrium distance
$C_{\square}$	curves from the geometry of the wrinkles
κ	the line curvature of a single curve
s_i	the arc length at the point (x_i, y_i)
S_i	the nondimensional arc length at the point (X_i, Y_i)
E_{e}	the elastic energy
γ	the bending rigidity of graphene
κ_{m}, $\kappa_{\mathrm{o/i}}$	the line curvature of the mid-line, outer/inner curve
κ_{tot}^2	the total squared curvatures of two curves
E_{v}	the vdW interaction energy
ϵ_{gg}	the graphene–graphene vdW interaction energy per unit length
ϵ_{gs}	the graphene–substrate vdW interaction energy per unit length
$\epsilon_{N\mathrm{gs}}$	the vdW interaction strength for N–layer graphene and substrate
E_{tot}	the total energy
X_{C_i}/Y_{C_i}	the nondimensional parametric solution for the curve C_i
x_{C_i}/y_{C_i}	the dimensional parametric solution for the curve C_i
$E_{\square}$	the energy inherent in the curve $C_{\square}$
$L_{\square}$	the length of the curve $C_{\square}$
$\psi_{\square}$	a constant of integration
$\alpha_{\square}$	a scaling factor

$h_{C_\square}$	the height of the curve $C_\square$
$\lambda_\square$	a Lagrange multiplier
F	the integrand part of a functional
$F_\square$	the partial derivative of F with respect to the variable $\square$
$L_{\mathrm{m,o/i}}$	the length of the mid-line, outer/inner layers of C_3
p, q	notations used to simplify calculations
g_1, g_2	functions from which the solution curves are constructed
A, B	parameters used for simplification purposes
$\epsilon_{N\mathrm{gs}}$	the vdW interaction of N graphene layers and the substrate
$\epsilon_{\mathrm{gg}}(\varphi)$	the graphene–graphene vdW interaction strength at a distance φ
D_{g}	the surface density of carbon atoms on a sheet of graphene
$\epsilon_{\mathrm{gs}}(\tilde{\varphi})$	the graphene–substrate vdW interaction strength at a distance $\tilde{\varphi}$
D_{s}	the volume density of the chemical element of the substrate
$\mathcal{A}_{\mathrm{g}\square}/\mathcal{B}_{\mathrm{g}\square}$	positive constants of the graphene–$\square$ attraction/repulsion
$E^{\mathrm{A}}_{\mathrm{tot}}/L^{\mathrm{A}}_{\mathrm{tot}}$	the total energy/length of collapsed wrinkles (conformation A)
$E^{\mathrm{B}}_{\mathrm{tot}}/L^{\mathrm{B}}_{\mathrm{tot}}$	the total energy/length of collapsed wrinkles (conformation B)
$E^{\mathrm{s}}_{\mathrm{tot}}/L^{\mathrm{s}}_{\mathrm{tot}}$	the total energy/length of self-adhered wrinkles
h_{crit}	the critical height of self-adhered wrinkles
$E_{\mathrm{crit}}/L_{\mathrm{crit}}$	the energy/length of self-adhered wrinkles at h_{crit}

Chapter 7

Conclusion

In this thesis, we propose a collection of mathematical models for a number of related graphene nanostructures. These models are constructed using the calculus of variations and the shape of the proposed structure is determined via an energy minimisation approach. To date, this method has been employed in modelling single-layer graphene folds [3, 59], and wrinkles [87]. In this thesis, we extend the use of variational calculus in the field of modelling graphene nanostructures by investigating four main configurations (graphically represented in Fig. 7.1), namely

1. single-layer graphene ripples,

2. supported multi-layer graphene folds,

3. unsupported multi-layer graphene folds, and

4. collapsed graphene wrinkles.

In each case, the modelling involves multiple physical parameters including the bending rigidity of graphene, vdW interaction strengths, equilibrium distances, and Lagrange multipliers relating to isoperimetric constraints. To fa-

cilitate the modelling, the equations are nondimensionalised to obtain a simplified model involving fewer parameters. Throughout this work, the calculus of variations is shown to be capable of modelling graphene configurations and providing results consistent with earlier theoretical and experimental studies. In the next three sections, the main novel results obtained for each of the above-mentioned configurations are summarised. The final section outlines potential directions for future research based on the work done in this thesis.

7.1 Single-layer graphene ripples

In Chapter 3, a variational model is constructed for a rippled graphene sheet supported by a metal substrate. This model comprises three cases for the configuration of the ripple that relate to the edge of the graphene sheet and the length of the substrate. Firstly, the transitional case assumes that the edge of the sheet and the substrate coincide. Then, the substrate constrained case accounts for the configuration when the ripple edge overhangs the substrate. Lastly, the graphene constrained case accounts for the configuration when the edge of the ripple does not extend to the substrate edge. Analytical solutions are derived for each case and a smooth transition between these cases is made based on the ratio of the Lagrange multiplier to the strength of vdW interaction.

In the analysis, two metal substrates are considered for comparison purposes, which are the Cu(111) and Ni(111) substrates. All three cases are incorporated to demonstrate a continuous relationship between the total energy per unit length and the substrate length. Additionally, the solution of the substrate constrained case is adopted to examine a flat graphene sheet on a shrinking substrate where two main effects have been observed. The

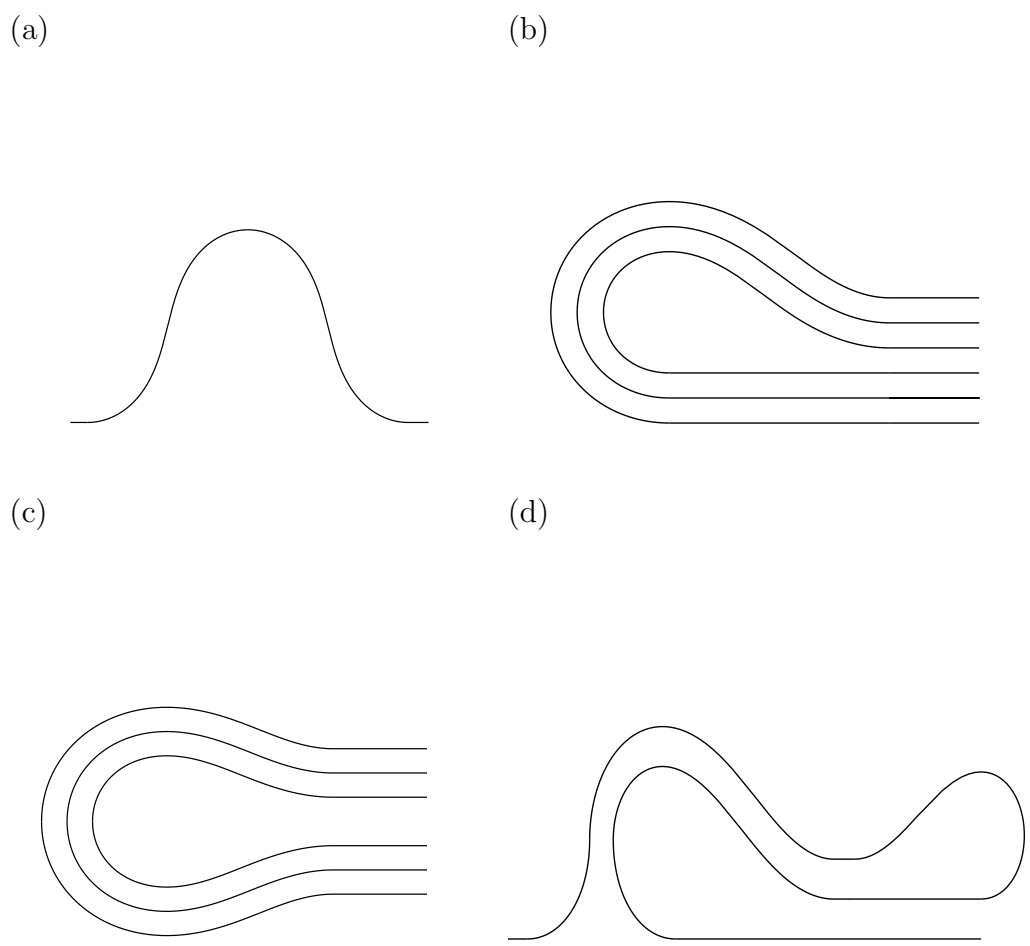

Figure 7.1: Graphene configurations investigated in this thesis: (a) single-layer ripples, (b) supported multi-layer folds, (c) unsupported multi-layer folds, and (d) collapsed wrinkles.

first of these is a ripple formation that appears with increasing height as the substrate shrinks. The second effect is that there is an increase in the total energy due to both the elastic energy that arises when the ripple forms, and the fact that the vdW interaction energy decreases when the substrate shrinks. To validate the mathematical model, predicted ripple profiles are compared to earlier results of molecular dynamical simulations and the com-

parison shows excellent agreement.

7.2 Multi-layer graphene folds

A fold of multi-layer graphene has been investigated in Chapters 4 and 5. In Chapter 4, a variational model is developed for folded multi-layer graphene supported on a substrate. The fold of multi-layer graphene has been previously modelled using a finite-deformation beam theory with a simplified model, where the curvature of a single-layer graphene was multiplied by the number of layers [57]. However, the model developed in this work takes into account the effects of curvature in each layer, and an expression for the total squared curvature is derived using a Taylor series expansion. Then, the folding conformation is examined under three truncations of the Taylor series for the total squared curvature, namely, the one-term approximation, the two-term approximation, and the three-term approximation.

To compare and assess these approximations, we exploit the experimental measurements reported in the literature for the hump height of folded multi-layer graphene supported on a SiO_2 substrate. Then, the SiO_2 substrate is adopted in the analysis and the LJ potential is employed to model values for the equilibrium distances and strengths of the vdW interaction. Our analysis suggests that the three-term approximation is capable of accurately predicting the folding profile of up to 5–layer graphene sheets, which is in good agreement with the experimental measurements of the hump height.

After establishing the accuracy of the three-term approximation in Chapter 4, we employ it again in another variational model for folded unsupported multi-layer graphene in Chapter 5. In this model, a novel analytical approach is proposed to predict the *effective* bending rigidity of multi-layer graphene.

Solutions for folded unsupported single- and multi-layer graphene are presented. Furthermore, the LJ potential is used to model values for the equilibrium distances and strengths of the vdW interaction. By changing the bending rigidity of single-layer graphene, we prescribe the effective bending rigidity of multi-layer graphene such that the predicted folding profiles obtained from both solutions are in best agreement. The analysis reveals that the effective bending rigidity of 2– to 6–layer graphene follows an approximate quadratic relationship with the number of layers. This relationship is confirmed by a log–log plot, and this result is also in line with earlier theoretical and experimental studies.

7.3 Collapsed graphene wrinkles

In Chapter 6, a variational model is constructed for the most intricate and complicated graphene configuration investigated in this thesis, the collapsed graphene wrinkle. Earlier works in the literature have approximated graphene wrinkles by circular concave and convex arcs with transition lines and modelled this complicated structure using a simplified energy formulation. In this thesis, the geometry of the wrinkle is partitioned into three continuous curves. Then, parametric solutions are derived from variational considerations for each curve. The Cu(111) and Ni(111) substrates are adopted in the analysis of the mathematical model for graphene ripples in Chapter 3. Also, these substrates have been used by Cox et al. [87] in the analysis of their models for arch-shaped and self-adhered wrinkles. Consequently, we adopt these substrates in the analysis of our model for collapsed graphene wrinkles in Chapter 6. Again, the LJ potential is employed to model values for the strength of the vdW interactions.

The analysis in this study takes into account two potential conformations for the collapsed wrinkle, and through an energy comparison, we predict that the folded bilayer section is always followed by a flat region. A collapsed wrinkle forms when a self-adhered wrinkle folds over towards the surface after achieving the maximum height. We report numerical values for this critical height through an energy comparison for the wrinkle before and after it collapses. Taking advantage of earlier theoretical work [87], we compare the total energy of a self-adhered wrinkle to that of collapsed wrinkle. Values for that critical height are calculated such that the collapsed wrinkle has lower total energy than the self-adhered wrinkle. These values are in line with previous theoretical and experimental results.

7.4 Future research

In this thesis, various configurations of supported graphene sheet(s) on a substrate are modelled. Hence, a straightforward extension to this work would be to apply these models to substrates other than those considered here by fitting the appropriate values of the parameters for the vdW interaction strengths and equilibrium distances. While in this thesis we assume a translational symmetry in the z–direction and then consider 2D problems throughout, the present models may also be extended by considering a radial symmetry with a small uniform bend. Specific directions of potential future research for each considered problem are presented below.

Single-layer graphene ripples

In Chapter 3, it is noted that a ripple forms in flat graphene located on a shrinking substrate. Thus, a possible avenue of research may be to address

this phenomenon by taking into account additional physical effects. For example, the model may be extended to account for the change in the vdW interaction strength as the substrate length and density change. This would introduce the parameter denoting the vdW interaction strength as a function of the independent variable which would undoubtedly complicate solving the corresponding Euler–Lagrange equation.

Multi-layer graphene folds

In Chapter 4, the Taylor series expansion is truncated to derive three approximations for the total squared curvature of folded multi-layer graphene. It has been shown that the three-term approximation is capable of accurately predicting the folding profile of up to 5–layer graphene. Thus, a possible future work could add extra terms in order to investigate the folding conformation of supported multi-layer graphene with more than 6 layers. However, simply extending the Taylor series would certainly complicate the derivation of the corresponding expression for the line curvature. Whereas in this thesis the total squared curvature is approximated using a Taylor series expansion, future research studies may look for an alternative approximation, such as the Padé approximation, which may lead to a more accurate expression while still maintaining mathematical tractability.

In Chapter 5, the effective bending rigidity of multi-layer graphene is predicted by comparing its folding profile to that of a single-layer graphene. While in this thesis we consider geometrically perfect graphene with uniform thickness distribution, modelling the folding of imperfect graphene differs from that of perfect graphene by taking into account the elastic energy in the impure region as discussed in Section 1.5.5. Therefore, a potential future work may involve applying the model in Chapter 5 to study the folding

conformations of imperfect graphene and investigating the change in the effective bending rigidity.

Collapsed graphene wrinkles

In Chapter 5, the conformation of the collapsed graphene wrinkle is modelled. In earlier work, the collapsed graphene wrinkle has been modelled as a concatenation of circular arcs. In this work, it is modelled as three continuous curves and parametric solutions are derived for each curve independently, which is an improvement in the modelling. A further improvement may come from modelling this complicated structure as a single continuous curve. Another possible work may consider modelling the multiple-folded graphene wrinkles.

Finally, the explicit analytical formulae derived in this thesis, such as the graphene–substrate vdW interaction energy given by (2.51), the analytical solutions given by (3.13), and the total squared curvature given by (4.5), are likely beneficial in the modelling of other observed conformations of graphene nanoribbons such as those shown in Fig. 7.2. In addition, these analytical formulae are potentially applicable to modelling configurations of other non-graphitic materials such as boron nitride nanosheet(s). However, the vdW interactions energy may complicate the modelling process since boron nitride nanosheet contains both boron and nitrogen atoms while graphene contains only carbon atoms.

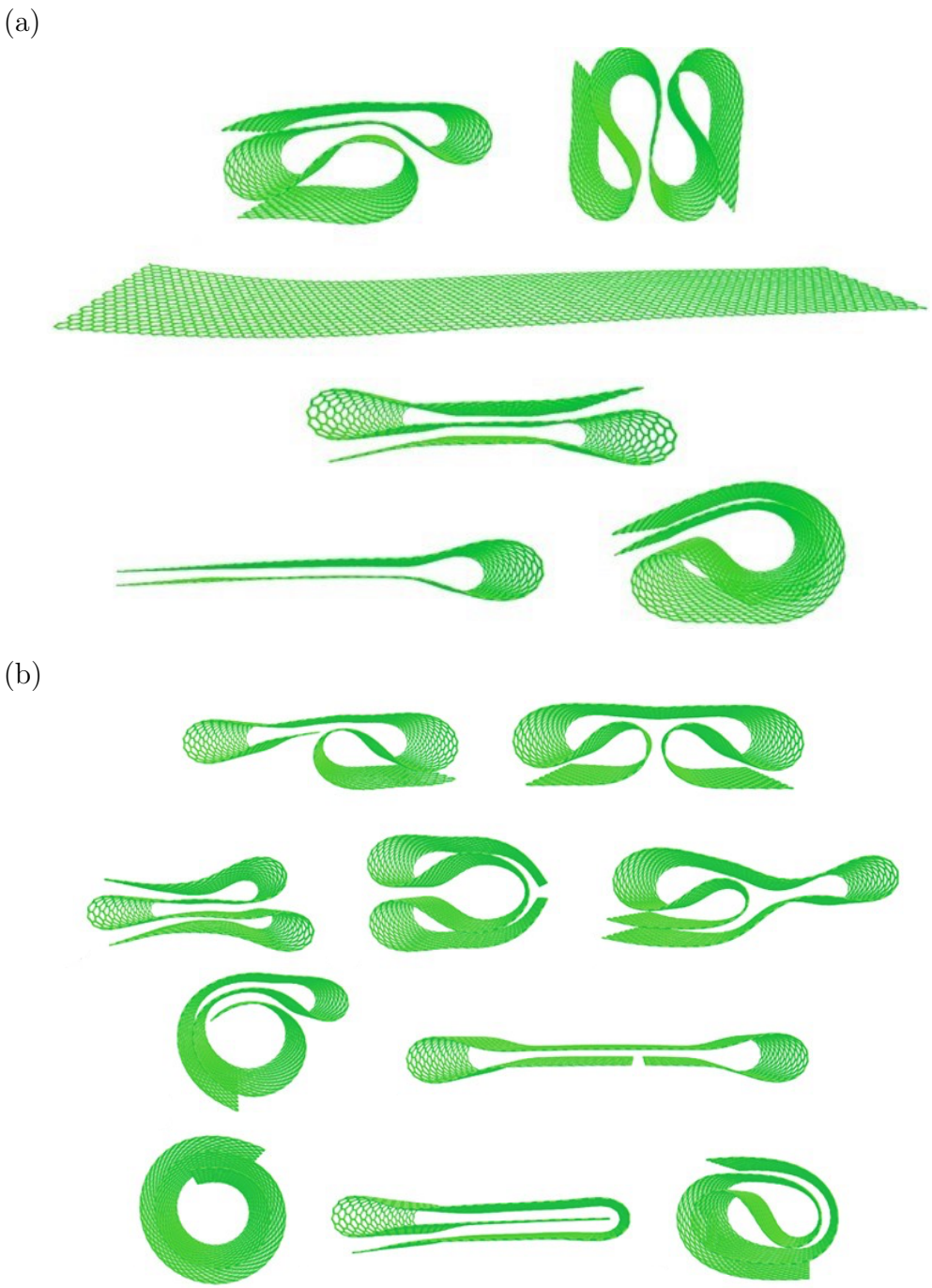

Figure 7.2: (a) Frequently and (b) occasionally observed graphene conformations. Taken from Ref. [8] under a Creative Commons Attribution 4.0 International License.

Appendix A

Analytical derivation of (4.3)

In this appendix, we present the analytical derivation of (4.3) which has been utilised to derive an expression for the total squared curvature of folded multi-layer graphene. The total squared curvature of a pair of inner and outer curves a distance $\nu\delta_{\mathrm{gg}}$ away from the mid-line is estimated by (4.2), which is given by

$$\kappa_{\mathrm{i}}^2 + \kappa_{\mathrm{o}}^2 = \frac{2\kappa_{\mathrm{m}}^2\left[1+\left(\nu\delta_{\mathrm{gg}}\kappa_{\mathrm{m}}\right)^2\right]}{\left[1-\left(\nu\delta_{\mathrm{gg}}\kappa_{\mathrm{m}}\right)^2\right]^2}. \tag{A.1}$$

We assume that the term $\left(\nu\delta_{\mathrm{gg}}\kappa_{\mathrm{m}}\right)^2 \ll 1$, and expand the denominator of (A.1) about $\left(\nu\delta_{\mathrm{gg}}\kappa_{\mathrm{m}}\right)^2 = 0$. We recall that the Taylor series of a function $f(x)$ about a point $x = a$ is given by

$$f(x) = \sum_{n=0}^{\infty} \frac{(x-a)^n}{n!} f^{(n)}(a) = f(a) + (x-a)\, f'(a) + \frac{(x-a)^2}{2!} f''(a) + \cdots,$$

which is known as Maclaurin series when $a = 0$. For instance, assume that we wish to expand a function f of the form

$$f(x) = \frac{1}{(1-x)^2},$$

about the point $x = 0$, where x is small. The nth derivative of the function f has the form

$$f^{(n)}(x) = \frac{(n+1)!}{(1-x)^{n+2}},$$

and therefore the Maclaurin series expansion of f is then

$$\begin{aligned}\frac{1}{(1-x)^2} &= \sum_{n=0}^{\infty} \frac{x^n}{n!} f^{(n)}(0) \\ &= \sum_{n=0}^{\infty} \frac{x^n}{n!} (n+1)! \\ &= \sum_{n=0}^{\infty} (n+1)\, x^n = 1 + 2x + 3x^2 + 4x^3 + \cdots . \end{aligned} \tag{A.2}$$

Repeating the same approach, we may write the following expression

$$\frac{1}{\left[1 - (\nu\delta_{\mathrm{gg}}\kappa_{\mathrm{m}})^2\right]^2} = 1 + 2\nu^2\delta_{\mathrm{gg}}^2\kappa_{\mathrm{m}}^2 + 3\nu^4\delta_{\mathrm{gg}}^4\kappa_{\mathrm{m}}^4 + 4\nu^6\delta_{\mathrm{gg}}^6\kappa_{\mathrm{m}}^6 + \cdots . \tag{A.3}$$

Consequently, we write (A.1) as

$$\begin{aligned}\kappa_{\mathrm{i}}^2 + \kappa_{\mathrm{o}}^2 &= 2\kappa_{\mathrm{m}}^2 \left(1 + \nu^2\delta_{\mathrm{gg}}^2\kappa_{\mathrm{m}}^2\right)\left(1 + 2\nu^2\delta_{\mathrm{gg}}^2\kappa_{\mathrm{m}}^2 + 3\nu^4\delta_{\mathrm{gg}}^4\kappa_{\mathrm{m}}^4 + 4\nu^6\delta_{\mathrm{gg}}^6\kappa_{\mathrm{m}}^6 + \cdots\right) \\ &= 2\kappa_{\mathrm{m}}^2 \left(1 + 3\nu^2\delta_{\mathrm{gg}}^2\kappa_{\mathrm{m}}^2 + 5\nu^4\delta_{\mathrm{gg}}^4\kappa_{\mathrm{m}}^4 + 7\nu^6\delta_{\mathrm{gg}}^6\kappa_{\mathrm{m}}^6 + \cdots\right) \\ &= 2\kappa_{\mathrm{m}}^2 \sum_{n=0}^{\infty} (2n+1) \left(\nu^2\delta_{\mathrm{gg}}^2\kappa_{\mathrm{m}}^2\right)^n .\end{aligned}$$

In this work we consider the first three terms of the series expansion, the total squared curvature of these inner and outer curves is approximated by

$$\kappa_{\mathrm{i}}^2 + \kappa_{\mathrm{o}}^2 \approx 2\kappa_{\mathrm{m}}^2 + 6\nu^2\delta_{\mathrm{gg}}^2\kappa_{\mathrm{m}}^4 + 10\nu^4\delta_{\mathrm{gg}}^4\kappa_{\mathrm{m}}^6,$$

and hence the derivation of (4.3) is completed.

Bibliography

[1] Andre K Geim and Konstantin S Novoselov. The rise of graphene. In *Nanoscience and technology: a collection of reviews from Nature journals*, pages 11–19. World Scientific, 2010.

[2] Xianhong Meng, Ming Li, Zhan Kang, Xiaopeng Zhang, and Jianliang Xiao. Mechanics of self-folding of single-layer graphene. *Journal of Physics D: Applied Physics*, 46(5):055308, 2013.

[3] Barry J Cox, Duangkamon Baowan, Wolfgang Bacsa, and James M Hill. Relating elasticity and graphene folding conformation. *RSC Advances*, 5(71):57515–57520, 2015.

[4] Yancheng Zhang, Ning Wei, Junhua Zhao, Yadong Gong, and Timon Rabczuk. Quasi-analytical solution for the stable system of the multilayer folded graphene wrinkles. *Journal of Applied Physics*, 114(6): 063511, 2013.

[5] Ming Li, LiXuan Che, FengWei Li, ZhenQun Guan, and Zhan Kang. Non-uniform self-folding of impure graphene. *International Journal of Mechanical Sciences*, 193:106158, 2021.

[6] Wen Wang, Shudu Yang, and Ashu Wang. Observation of the unex-

pected morphology of graphene wrinkle on copper substrate. *Scientific Reports*, 7(1):1–6, 2017.

[7] Xiaoming Chen, Chenglin Yi, and Changhong Ke. Bending stiffness and interlayer shear modulus of few-layer graphene. *Applied Physics Letters*, 106(10):101907, 2015.

[8] Ruslan D. Yamaletdinov and Yuriy V. Pershin. Finding stable graphene conformations from pull and release experiments with molecular dynamics. *Scientific Reports*, 7(1):42356, 2017.

[9] Andre Konstantin Geim. Graphene: status and prospects. *Science*, 324 (5934):1530–1534, 2009.

[10] Changgu Lee, Xiaoding Wei, Jeffrey W Kysar, and James Hone. Measurement of the elastic properties and intrinsic strength of monolayer graphene. *Science*, 321(5887):385–388, 2008.

[11] Alexander A Balandin, Suchismita Ghosh, Wenzhong Bao, Irene Calizo, Desalegne Teweldebrhan, Feng Miao, and Chun Ning Lau. Superior thermal conductivity of single-layer graphene. *Nano Letters*, 8(3):902–907, 2008.

[12] Ying Liu, Chongze Hu, Jingsong Huang, Bobby G Sumpter, and Rui Qiao. Tuning interfacial thermal conductance of graphene embedded in soft materials by vacancy defects. *The Journal of Chemical Physics*, 142 (24):244703, 2015.

[13] Kai-Tak Lam, Chengkuo Lee, and Gengchiau Liang. Bilayer graphene nanoribbon nanoelectromechanical system device: A computational study. *Applied Physics Letters*, 95(14):143107, 2009.

[14] M Poetschke, CG Rocha, LEF Foa Torres, S Roche, and G Cuniberti. Modeling graphene-based nanoelectromechanical devices. *Physical Review B*, 81(19):193404, 2010.

[15] Yujie Wei, Baoling Wang, Jiangtao Wu, Ronggui Yang, and Martin L. Dunn. Bending rigidity and Gaussian bending stiffness of single-layered graphene. *Nano Letters*, 13(1):26–30, 2013.

[16] Kostas Kostarelos and Kostya S Novoselov. Graphene devices for life. *Nature Nanotechnology*, 9(10):744, 2014.

[17] Ravi Kant Upadhyay, Navneet Soin, and Susanta Sinha Roy. Role of graphene/metal oxide composites as photocatalysts, adsorbents and disinfectants in water treatment: a review. *RSC Advances*, 4(8):3823–3851, 2014.

[18] Steven P Koenig, Luda Wang, John Pellegrino, and J Scott Bunch. Selective molecular sieving through porous graphene. *Nature Nanotechnology*, 7(11):728, 2012.

[19] Bing Yu, Hao Li, Jai White, Scott Donne, Jiabao Yi, Shibo Xi, Yang Fu, Graeme Henkelman, Hai Yu, Zuliang Chen, et al. Tuning the catalytic preference of ruthenium catalysts for nitrogen reduction by atomic dispersion. *Adv. Funct. Mater.*, 30(6):1905665, 2020.

[20] Shuaiwei Wang, Baocheng Yang, Houyang Chen, and Eli Ruckenstein. Reconfiguring graphene for high-performance metal-ion battery anodes. *Energy Storage Mater.*, 16:619–624, 2019.

[21] Beibei Zhan, Chen Li, Jun Yang, Gareth Jenkins, Wei Huang, and Xiaochen Dong. Graphene field-effect transistor and its application for electronic sensing. *Small*, 10(20):4042–4065, 2014.

[22] SRC Vivekchand, Chandra Sekhar Rout, KS Subrahmanyam, Achutharao Govindaraj, and CNR Rao. Graphene-based electrochemical supercapacitors. *Journal of Chemical Sciences*, 120(1):9–13, 2008.

[23] Duangkamon Baowan, Barry J Cox, and James M Hill. Discrete and continuous approximations for nanobuds. *Fullerenes, Nanotubes and Carbon Nanostructures*, 18(2):160–177, 2010.

[24] MS Dresselhaus, G Dresselhaus, and R Saito. Physics of carbon nanotubes. *Carbon*, 33(7):883–891, 1995.

[25] Shuaiwei Wang, Baocheng Yang, Houyang Chen, and Eli Ruckenstein. Popgraphene: a new 2D planar carbon allotrope composed of 5–8–5 carbon rings for high-performance lithium-ion battery anodes from bottom-up programming. *J. Mater. Chem. A.*, 6(16):6815–6821, 2018.

[26] Liam Britnell, Roman V Gorbachev, Rashid Jalil, Branson D Belle, Fred Schedin, Mikhail I Katsnelson, Laurence Eaves, Sergey V Morozov, Alexander S Mayorov, Nuno MR Peres, et al. Electron tunneling through ultrathin boron nitride crystalline barriers. *Nano Letters*, 12(3):1707–1710, 2012.

[27] Marino Arroyo and Ted Belytschko. Finite crystal elasticity of carbon nanotubes based on the exponential Cauchy–Born rule. *Physical Review B*, 69(11):115415, 2004.

[28] Qiang Lu, Marino Arroyo, and Rui Huang. Elastic bending modulus of monolayer graphene. *Journal of Physics D: Applied Physics*, 42(10): 102002, 2009.

[29] Konstantin N Kudin, Gustavo E Scuseria, and Boris I Yakobson. C_2F,

BN, and C nanoshell elasticity from ab initio computations. *Physical Review B*, 64(23):235406, 2001.

[30] Enrique Muñoz, Abhishek K Singh, Morgana A Ribas, Evgeni S Penev, and Boris I Yakobson. The ultimate diamond slab: Graphane versus graphene. *Diamond and Related Materials*, 19(5-6):368–373, 2010.

[31] R Nicklow, N Wakabayashi, and HG Smith. Lattice dynamics of pyrolytic graphite. *Physical Review B*, 5(12):4951, 1972.

[32] J Tersoff. Energies of fullerenes. *Physical Review B*, 46(23):15546, 1992.

[33] Zhan-chun Tu and Zhong-can Ou-Yang. Single-walled and multiwalled carbon nanotubes viewed as elastic tubes with the effective Young's moduli dependent on layer number. *Physical Review B*, 65(23):233407, 2002.

[34] Pekka Koskinen and Oleg O Kit. Approximate modeling of spherical membranes. *Physical Review B*, 82(23):235420, 2010.

[35] S Saqib Shams, Ruoyu Zhang, and Jin Zhu. Graphene synthesis: a review. *Mater. Sci. Pol*, 33(3):566–578, 2015.

[36] Roberto Munoz and Cristina Gómez-Aleixandre. Review of CVD synthesis of graphene. *Chemical Vapor Deposition*, 19(10-11-12):297–322, 2013.

[37] Levente Tapasztó, Traian Dumitrică, Sung Jin Kim, Péter Nemes-Incze, Chanyong Hwang, and László P Biró. Breakdown of continuum mechanics for nanometre-wavelength rippling of graphene. *Nature Physics*, 8 (10):739–742, 2012.

[38] Wenjuan Zhu, Tony Low, Vasili Perebeinos, Ageeth A Bol, Yu Zhu, Hugen Yan, Jerry Tersoff, and Phaedon Avouris. Structure and electronic transport in graphene wrinkles. *Nano Letters*, 12(7):3431–3436, 2012.

[39] Chun Hung Lui, Li Liu, Kin Fai Mak, George W Flynn, and Tony F Heinz. Ultraflat graphene. *Nature*, 462(7271):339, 2009.

[40] A.N. Obraztsov, E.A. Obraztsova, A.V. Tyurnina, and A.A. Zolotukhin. Chemical vapor deposition of thin graphite films of nanometer thickness. *Carbon*, 45(10):2017–2021, 2007.

[41] Shikai Deng and Vikas Berry. Wrinkled, rippled and crumpled graphene: an overview of formation mechanism, electronic properties, and applications. *Materials Today*, 19(4):197–212, 2016.

[42] Jannik C Meyer, Andre K Geim, Mikhail I Katsnelson, Konstantin S Novoselov, Tim J Booth, and Siegmar Roth. The structure of suspended graphene sheets. *Nature*, 446(7131):60, 2007.

[43] Shanshan Chen, Qiongyu Li, Qimin Zhang, Yan Qu, Hengxing Ji, Rodney S Ruoff, and Weiwei Cai. Thermal conductivity measurements of suspended graphene with and without wrinkles by micro-Raman mapping. *Nanotechnology*, 23(36):365701, 2012.

[44] C Wang, Y Liu, L Li, and H Tan. Anisotropic thermal conductivity of graphene wrinkles. *Nanoscale*, 6(11):5703–5707, 2014.

[45] Yi Wang, Rong Yang, Zhiwen Shi, Lianchang Zhang, Dongxia Shi, Enge Wang, and Guangyu Zhang. Super-elastic graphene ripples for flexible strain sensors. *ACS Nano*, 5(5):3645–3650, 2011.

[46] Wenzhong Bao, Feng Miao, Zhen Chen, Hang Zhang, Wanyoung Jang, Chris Dames, and Chun Ning Lau. Controlled ripple texturing of suspended graphene and ultrathin graphite membranes. *Nature Nanotechnology*, 4(9):562, 2009.

[47] Ivo Pletikosić, Marko Kralj, Petar Pervan, Radovan Brako, Johann Coraux, AT N'diaye, C Busse, and Th Michely. Dirac cones and minigaps for graphene on Ir(111). *Physical Review Letters*, 102(5):056808, 2009.

[48] Gui Gui, Jianxin Zhong, and Zhenqiang Ma. Electronic properties of rippled graphene. *Journal of Physics: Conference Series*, 402(9):012004, 2012.

[49] Zhonghuai Pan, Nan Liu, Lei Fu, and Zhongfan Liu. Wrinkle engineering: a new approach to massive graphene nanoribbon arrays. *Journal of the American Chemical Society*, 133(44):17578–17581, 2011.

[50] Xiaoming Chen, Liuyang Zhang, Yadong Zhao, Xianqiao Wang, and Changhong Ke. Graphene folding on flat substrates. *Journal of Applied Physics*, 116(16):164301, 2014.

[51] Hannes C Schniepp, Konstantin N Kudin, Je-Luen Li, Robert K Prud'homme, Roberto Car, Dudley A Saville, and Ilhan A Aksay. Bending properties of single functionalized graphene sheets probed by atomic force microscopy. *ACS Nano*, 2(12):2577–2584, 2008.

[52] Matthew Becton, Liuyang Zhang, and Xianqiao Wang. Effects of surface dopants on graphene folding by molecular simulations. *Chemical Physics Letters*, 584:135–141, 2013.

[53] Vivek B Shenoy and David H Gracias. Self-folding thin-film materials: From nanopolyhedra to graphene origami. *MRS Bulletin*, 37(9):847, 2012.

[54] Liuyang Zhang, Xiaowei Zeng, and Xianqiao Wang. Programmable hydrogenation of graphene for novel nanocages. *Scientific Reports*, 3(1): 1–8, 2013.

[55] Shuze Zhu and Teng Li. Hydrogenation-assisted graphene origami and its application in programmable molecular mass uptake, storage, and release. *ACS Nano*, 8(3):2864–2872, 2014.

[56] Steven Cranford, Dipanjan Sen, and Markus J Buehler. Meso-origami: folding multilayer graphene sheets. *Applied Physics Letters*, 95(12): 123121, 2009.

[57] Xian-Hong Meng, Ming Li, Zhan Kang, and Jian-Liang Xiao. Folding of multi-layer graphene sheets induced by van der Waals interaction. *Acta Mechanica Sinica*, 30(3):410–417, 2014.

[58] Alejandro Lopez-Bezanilla, Jessica Campos-Delgado, Bobby G Sumpter, Daniel L Baptista, Takuya Hayashi, Yoong A Kim, Hiroyuki Muramatsu, Morinobu Endo, Carlos A Achete, Mauricio Terrones, et al. Geometric and electronic structure of closed graphene edges. *The Journal of Physical Chemistry Letters*, 3(15):2097–2102, 2012.

[59] Tom Dyer, Ngamta Thamwattana, and Barry J Cox. Conformation of graphene folding around single-walled carbon nanotubes. *Journal of Molecular Modeling*, 24(4):99, 2018.

[60] Weibang Lu and Tsu-Wei Chou. Analysis of the entanglements in carbon nanotube fibers using a self-folded nanotube model. *Journal of the Mechanics and Physics of Solids*, 59(3):511–524, 2011.

[61] Ming Li, Xiao Li, LiXuan Che, FengWei Li, and Zhan Kang. Non-uniform global-buckling and local-folding in thin film of stretchable electronics. *International Journal of Mechanical Sciences*, 175:105537, 2020.

[62] Bruce Brunt. *The Calculus of Variations*. Springer New York, NY, 2004.

[63] J Stern. Der gelenkstab bei großen elastischen verformungen. *Ingenieur-Archiv*, 48(3):173–184, 1979.

[64] Arthur Erdélyi. Higher transcendental functions. *Higher transcendental functions*, page 59, 1953.

[65] Paul F Byrd and Morris D Friedman. *Handbook of elliptic integrals for engineers and physicists*, volume 67. Springer, 2013.

[66] Izrail Solomonovich Gradshteyn and Iosif Moiseevich Ryzhik. *Table of integrals, series, and products*. Academic Press, 8$^{\text{th}}$ edition, 2014.

[67] Milton Abramowitz and Irene A Stegun. Handbook of mathematical functions with formulas, graphs, and mathematical table. In *US Department of Commerce*. National Bureau of Standards Applied Mathematics series 55, 1965.

[68] Girolamo Cardano. *Ars magna or the rules of algebra*. Dover Publications, 1993 (reprint from 1545).

[69] Yang Wang, D Tomanek, and GF Bertsch. Stiffness of a solid composed of c 60 clusters. *Physical Review B*, 44(12):6562, 1991.

[70] Dong Qian, Gregory J Wagner, and, Wing Kam Liu, Min-Feng Yu, and Rodney S Ruoff. Mechanics of carbon nanotubes. *Appl. Mech. Rev.*, 55 (6):495–533, 2002.

[71] Duangkamon Baowan, Barry J Cox, Tamsyn A Hilder, James M Hill, and Ngamta Thamwattana. *Modelling and mechanics of carbon-based nanostructured materials*. William Andrew, Oxford, 2017.

[72] Fredrik Schedin, AK Geim, SV Morozov, EW Hill, P Blake, MI Katsnelson, and KS Novoselov. Detection of individual gas molecules adsorbed on graphene. *Nature Materials*, 6(9):652, 2007.

[73] Annalisa Fasolino, JH Los, and Mikhail I Katsnelson. Intrinsic ripples in graphene. *Nature Materials*, 6(11):858, 2007.

[74] Johan M Carlsson. Graphene: buckle or break. *Nature Materials*, 6(11): 801, 2007.

[75] Gulsah Yildiz, Majbritt Bolton-Warberg, and Firas Awaja. Graphene and graphene oxide for bio-sensing: general properties and the effects of graphene ripples. *Acta Biomaterialia*, 2021.

[76] Ryan JT Nicholl, Nickolay V Lavrik, Ivan Vlassiouk, Bernadeta R Srijanto, and Kirill I Bolotin. Hidden area and mechanical nonlinearities in freestanding graphene. *Physical Review Letters*, 118(26):266101, 2017.

[77] Ryan JT Nicholl, Hiram J Conley, Nickolay V Lavrik, Ivan Vlassiouk, Yevgeniy S Puzyrev, Vijayashree Parsi Sreenivas, Sokrates T Pantelides, and Kirill I Bolotin. The effect of intrinsic crumpling on the mechanics of free-standing graphene. *Nature Communications*, 6(1):1–7, 2015.

[78] JH Los, A Fasolino, and MI Katsnelson. Scaling behavior and strain dependence of in-plane elastic properties of graphene. *Physical Review Letters*, 116(1):015901, 2016.

[79] G. Giovannetti, P. A. Khomyakov, G. Brocks, V. M. Karpan, J. van den Brink, and P. J. Kelly. Doping graphene with metal contacts. *Phys. Rev. Lett.*, 101(2):026803, 2008.

[80] Thomas Olsen, Jun Yan, Jens J Mortensen, and Kristian S Thygesen. Dispersive and covalent interactions between graphene and metal surfaces from the random phase approximation. *Physical Review Letters*, 107(15):156401, 2011.

[81] Zhiping Xu and Markus J Buehler. Interface structure and mechanics between graphene and metal substrates: a first-principles study. *Journal of Physics: Condensed Matter*, 22(48):485301, 2010.

[82] Y Gamo, A Nagashima, M Wakabayashi, M Terai, and Ch Oshima. Atomic structure of monolayer graphite formed on Ni(111). *Surface Science*, 374(1-3):61–64, 1997.

[83] Toshiaki Kato and Rikizo Hatakeyama. Direct growth of doping-density-controlled hexagonal graphene on SiO_2 substrate by rapid-heating plasma CVD. *ACS Nano*, 6(10):8508–8515, 2012.

[84] Norio Inui and Sho Iwasaki. Interaction energy between graphene and a silicon substrate using pairwise summation of the Lennard-Jones potential. *e-Journal of Surface Science and Nanotechnology*, 15:40–49, 2017.

[85] YongKuan Shen and HengAn Wu. Interlayer shear effect on multilayer graphene subjected to bending. *Applied Physics Letters*, 100(10):101909, 2012.

[86] Edmund Han, Jaehyung Yu, Emil Annevelink, Jangyup Son, Dongyun A Kang, Kenji Watanabe, Takashi Taniguchi, Elif Ertekin, Pinshane Y Huang, and Arend M van der Zande. Ultrasoft slip-mediated bending in few-layer graphene. *Nature Materials*, 19(3):305–309, 2020.

[87] Barry J Cox, Tom Dyer, and Ngamta Thamwattana. A variational model for conformation of graphene wrinkles formed on a shrinking solid metal substrate. *Materials Research Express*, 7(8):085001, 2020.

[88] Tim Verhagen, Barbara Pacakova, Milan Bousa, Uwe Hubner, Martin Kalbac, Jana Vejpravova, and Otakar Frank. Superlattice in collapsed graphene wrinkles. *Scientific Reports*, 9(1):1–7, 2019.

[89] Fei Long, Poya Yasaei, Raj Sanoj, Wentao Yao, Petr Král, Amin Salehi-Khojin, and Reza Shahbazian-Yassar. Characteristic work function variations of graphene line defects. *ACS Applied Materials & Interfaces*, 8 (28):18360–18366, 2016.

[90] Leonardo Spanu, Sandro Sorella, and Giulia Galli. Nature and strength of interlayer binding in graphite. *Physical Review Letters*, 103(19): 196401, 2009.

List of the author's publications and presentations

Journal articles

1. J. Aljedani, M. J. Chen and B. J. Cox, 2020 "Variational model for a rippled graphene sheet," *RSC Advances,* **10** (27), 16016–16026, doi:10.1039/C9RA10439A.

2. J. Aljedani, M. J. Chen and B. J. Cox, 2021 "Multi–layer graphene folds supported on a substrate: a variational model," *Materials Research Express,* **8** (1), 015002, doi:10.1088/2053-1591/abd26b.

3. J. Aljedani, M. J. Chen and B. J. Cox, 2021 "Estimating the effective bending rigidity of multi-layer graphene," *Materials Research Express,* **8** (5), 055001, doi:10.1088/2053-1591/abfb29.

4. J. Aljedani, M. J. Chen and B. J. Cox, 2021 "Variational model for collapsed graphene wrinkles," *Applied Physics A,* **127** (11), 886, doi:10.1007/s00339-021-05000-y.

Conference paper

5. J. Aljedani, M. J. Chen and B. J. Cox, 2022 "Analysing the stability of graphene wrinkles using variational calculus," *ANZIAM Journal:*

Proceedings of the 15th Biennial Engineering Mathematics and Applications Conference, EMAC-2021, **63** (2022), C97–C109, doi:10.21914/anziamj.v63.17079

Conference presentations

- Australia and New Zealand Industrial and Applied Mathematics (ANZIAM)

  1. 2020 (Hunter Valley, NSW): Variational model for a rippled graphene sheet.
  2. 2021 (Virtual): Multi-layer graphene folds supported on a substrate.
  3. 2022 (Virtual): Analysing the stability of graphene wrinkles using variational calculus.

- Statistical Mechanics of Soft Matter (SM^2)

  4. 2019 (Adelaide, SA): Variational model for a rippled graphene sheet.
  5. 2020 (Virtual): Multi-layer graphene folds supported on a substrate.

- South Australia ANZIAM mini-meeting

  6. 2019 (Adelaide, SA): Variational model for a rippled graphene sheet.

- Engineering Mathematics and Applications Conference (EMAC)

  7. 2021 (Virtual): Analysing the stability of graphene wrinkles using variational calculus.